

POLITECNICO DI TORINO

MASTER OF SCIENCE DEGREE IN
MECHANICAL ENGINEERING



DYNAMIC ANALYSIS OF THE SOURCES OF VARIATION INSIDE THE PANTOGRAPH – CATENARY SYSTEM

MASTER THESIS

Supervisors

Stefano Marchesiello

Dario Anastasio

Author

Santiago Nicolas Martin Galli

A.Y 2020 - 21

Abstract

To power electrically tractioned railway vehicles, a connection between the vehicle and the source of energy is needed. This is achieved with the combined action of a train device called pantograph and the catenary, a powered line positioned along the railway. Guaranteeing a constant contact force between the two parts is essential to allow continuous energy feed to the vehicle.

The geometry of the catenary along the line generates important force fluctuation. A rigid and periodical geometry is considered for the study of these fluctuations under different pantograph velocities and contact stiffness rigidities. Its periodical nature is studied together with its behaviour in the frequency domain.

Due to these fluctuations, mechanical waves are generated inside the catenary system, on the messenger and contact wires. Wave dispersion is studied modelling the contact wire as an Euler-Bernoulli beam and the results are compared to an analytical model.

In the catenary system, the messenger and contact wires are connected by so called droppers. These droppers couple the dynamic behaviour of both wires. Transmission and reflection of mechanical waves are studied by using the proposed analytical models.

Acknowledgements

I would like to specially thank my thesis relator Professor Stefano Marchesiello and my thesis co-relator Professor Dario Anastasio for the support and guidance during these months of work and learning.

I would also like to thank to my colleagues and friends in Cordoba, Salerno and Turin for the last years shared together and to my family for everything.

Contents

Abstract	i
Acknowledgements	ii
Contents	iii
List of Figures	v
List of Tables	viii
List of Equations	ix
Chapter 1 Introduction	1
1.1 Motivation	1
1.1.1 Mechanical Stability and Locomotion Constraints.....	1
1.1.2 Maximum Power Constraints	3
1.2 Sliding Contact System Characteristics.....	4
1.3 Structure of the Thesis.....	7
Chapter 2 Variable Geometry Effects	9
2.1 Analytic Model.....	9
2.2 Analysis with Spatial Velocity as an Input.....	11
2.2.1 Mechanical Impedance	13
2.2.2 Geometric Force.....	14
2.3 Analysis with Spatial Displacement as an Input	15
2.3.1 Dynamic Stiffness	17
2.3.2 Geometric Force.....	17
2.4 Convergence – Contact Stiffness.....	18
Chapter 3 Mechanical Wave Effects - Dispersion	25
3.1 Dispersion.....	25
3.2 Analytic Model.....	29
3.3 Finite Element Method Analysis	31
3.3.1 Static FEM Configuration.....	31
3.3.2 Dynamic FEM Configuration	35
3.3.3 Newmark Method	36
3.3.4 HHT- α Method	40
3.4 Wave Velocity and Frequency	46
Chapter 4 Mechanical Wave Effects – Transmission and Reflection	49
4.1 Wave Reflection and Transmission on a Lumped Mass	49

4.2 Wave Reflection and Transmission on a Dropper.....	52
4.2.1 Input Wave on One of the Two Cables.....	53
4.2.2 Input wave on a Dropper – Waves Generated in the Two Cables	59
4.2.3 Mast Behaviour	61
4.3 FEM Result.....	63
4.3.1 Lumped Mass Simulations.....	63
4.3.2 Dropper Simulations – One Wire at the Time	65
4.3.3 Dropper Simulations – Two Wires at the Time	69
4.3.4 Mast Simulations	71
Chapter 5 Conclusion.....	73
5.1 Summary.....	73
5.2 Proposed Future Works	75
Appendices	77
A. Procedures for the Analysis on the Time and Frequency Domains	78
B. Flow Charts of the Used Numerical Methods	80
C. Procedure of the Wave Velocity Calculation in Dispersive Mediums.....	82
D. Comments on Digital and Analogue Filters	86
D.1 FIR Filters	86
D.2 Butterworth Filters	91
References	95

List of Figures

Figure 1. 1 Hunting mode, where y is the lateral displacement, $d\psi$ is the yaw rotation and $d\varphi$ is the rotation of the wheel axis. Adaptation from (Bosso, 2021).....	2
Figure 1. 2 Curve paths, with α the inclination of the rails plane, h the elevation of one of the rails respect to the other, G the centre of gravity of the train and F_c the centrifugal force and P the weight force. Adaptation from (Bosso, 2021).....	2
Figure 1. 3 Main constraints of the railway system. Adaptation from (Iwnicki, Spiryagin, Cole, & McSweeney, 2019).....	4
Figure 1. 4 Steady arm with its dimensions (left side). Contact wire section (right side). From (Vo Van, 2016).....	5
Figure 1. 5 Joints between bracket and mast (left side), messenger wire and bracket (centre) and registration arm and steady arm (right side). From (Vo Van, 2016).....	5
Figure 1. 6 Sliding contact system scheme. Adaptation from (Vo Van, 2016).....	6
Figure 1. 7 Main parts of the pantograph ATR 95 (left). ATR95 on the top of an ETR500 (right). From (Turri, 2017).....	6
Figure 2.1 Deflection of two spans	10
Figure 2. 2 Pantograph and contact wire model. Adaptation from (Vo Van, 2016).....	10
Figure 2. 3 Velocity in the spatial frequency domain	11
Figure 2. 4 Mechanical impedance in the frequency domain for three different contact stiffness k_c	14
Figure 2. 5 Contact force at 90 km/h (red) and 320 km/h (blue) for a contact stiffness $k_c = 50kN$	15
Figure 2. 6 Dynamic stiffness in the frequency domain for three different contact stiffnesses k_c	17
Figure 2. 7 Force comparison between the velocity and displacement approaches.....	18
Figure 2. 8 Variation coefficient of the non-filtered force function of the contact stiffness ...	19
Figure 2. 9 Amplitude spectrum of the non-filtered geometric contact force.....	20
Figure 2. 10 Variation coefficient of the 20Hz-filtered force function of the contact stiffness	20
Figure 2. 11 Amplitude spectrum of the 20Hz-filtered geometric contact force for different contact stiffness values.....	21
Figure 2. 12 Variation coefficient of the 70Hz-filtered force function of the contact stiffness	22
Figure 2. 13 Amplitude spectrum of the 70Hz-filtered geometric contact force for different contact stiffness values.....	22
Figure 3. 1 Angular frequency function of the wavenumber for non-dispersive and dispersive mediums (left side). Phase velocity and group velocity on a dispersive medium for $k=15$ (right side).	28
Figure 3. 2 Error in phase velocity when using the string and Euler-Bernoulli models	29

Figure 3. 3 Definition of the model proposed for the study of wave dispersion. Adaptation from (Hyeon Cho, 2008)	30
Figure 3. 4 Acceleration obtained from the mode superposition's method.....	31
Figure 3. 5 Euler Bernoulli beam element. Adaptation from (Genta, 2009).....	32
Figure 3. 6 Matrix assembly scheme.....	34
Figure 3. 7 Matrix constraint scheme.....	35
Figure 3. 8 Velocity and Acceleration response obtained from Newmark's integration method with $\Delta t=0.003s$	38
Figure 3. 9 Velocity and Acceleration response obtained from Newmark's integration method with $\Delta t=0.001s$	39
Figure 3. 10 Spectral radii function of the normalized time steps for the HHT- α method and the family of Newmark methods. Figure from (Hilber, Hughes, & Taylor, 1977).	42
Figure 3. 11 Damping ratios vs the normalized time steps for the HHT- α method and the family of Newmark methods. Figure from (Hilber, Hughes, & Taylor, 1977).....	43
Figure 3. 12 Velocity and Acceleration response obtained from Newmark's and alpha's integration methods with $\Delta t=0.003s$	44
Figure 3. 13 Velocity and Acceleration response obtained from Newmark's and alpha's integration methods with $\Delta t=0.001s$	45
Figure 3. 14 Acceleration response obtained with HHT- α method with a time step $dt=0.001s$ and four negative α -dissipation values.	46
Figure 3. 15 Filtered input and output signals of an input with $f=50Hz$ (left side). Spectrogram at 50 Hz of the input and output waves (right side). Calculations made with alpha method...	47
Figure 4. 1 Lumped mass on a single wire of length $2dx$. Adaptation from (Vo Van, 2016)..	50
Figure 4. 2 Coefficients of reflection (blue) and transmission (red) for lumped masses of 195gr (dashed) and 1kg (solid).....	52
Figure 4. 3 System configurations with an input at the same distance ($x=10m$) from the measuring point (green point): Singular incident wave on the CW (left side). Two incident waves, one on the MW and one on the CW generated by positioning the input on a dropper (right side).	53
Figure 4. 4 Dropper connecting the two wires model, input wave on a single wire. Adaptation from (Vo Van, 2016).....	53
Figure 4. 5 Coefficients of reflection (blue), transmission on the CW (red) and transmission on the MW (yellow). Incident wave on the CW for a standard dropper mass of 195gr (left side) and for a reinforced dropper 1kg (right side).	55
Figure 4. 6 Variation of the CW transfer functions with the modification of different parameters for a reinforced dropper (nominal) mass (1kg).....	56
Figure 4. 7 Wave velocities in the CW for a standard dropper mass of 195gr (left side) and for a reinforced dropper 1kg (right side).....	57
Figure 4. 8 Variation of the MW transfer functions with the modification of different parameters for a reinforced dropper (nominal) mass (1kg).....	58
Figure 4. 9 Wave velocities in the MW for a standard dropper mass of 195gr (left side) and for a reinforced dropper 1kg (right side).....	59
Figure 4. 10 Droppers connecting the two wires model, input wave on both wires. Adaptation from (Vo Van, 2016).....	60

Figure 4. 11 Wave velocities in the MW and CW for a normal dropper mass of 195gr.	60
Figure 4. 12 System configurations with an input wave on the last dropper of a span at a distance $2x$ ($x=5m$) from the measuring point (green point). In orange, the steady arm (SA) located at both endings.	61
Figure 4. 13 Waves propagating on the boundary segment of the messenger wire after a mass drop below the last dropper.	62
Figure 4. 14 Analytical vertical velocity of the messenger wire after the mass drop: velocity levels obtained after the successive reflections.	62
Figure 4. 15 Wave reflections on a lumped mass of 9.6 kg located on the steady arm for an input generated with a mass drop of 21.1 kg.	64
Figure 4. 16 Comparison between analytic and simulated results	65
Figure 4. 17 Analytic and simulated wave transmissions and reflections for the CW	67
Figure 4. 18 Analytic and simulated wave transmissions and reflections for the MW.	68
Figure 4. 19 Comparison between the sum of the transmitted, reflected and incident waves computed using FEM A, FEM B and analytically computed	70
Figure 4. 20 Simulated wave's reflection compared to the analytic results.	71
Figure 4. 21 Reflected waves on the mast (Messenger wire) and the steady arm (Contact wire) after mass drop generating an input velocity of 0.6 m/s	72

List of Tables

Table 2. 1 Parameters of the pantograph-catenary model.....	13
Table 3. 1 Parameters of the tensioned Euler-Bernoulli beam model.....	31
Table 3. 2 Wave propagation speed function of the excitation frequency.	48
Table 4. 1 Parameters of the lumped mass model.....	51
Table 4. 2 Parameters used in the lumped mass analytic calculation and FEM simulation.....	63
Table 4. 3 Parameters used for the mass drop near a dropper experiment, for the analytic calculation and FEM simulation	66

List of Equations

(1.1) Coefficient of variation.....	7
(2.2) Vertical velocity on the spatial frequency domain	11
(2.3) Spatial frequency or wavenumber definition.....	11
(2.4) Vertical displacement on the spatial domain (single sided and double sided spectrum)	12
(2.5) Angular frequency definition.....	12
(2.6) Vertical velocity on the time frequency domain	12
(2.7) Equation of motion of the MDOF system (velocity approach).....	12
(2.8) Geometric force on the time frequency domain function of velocities	12
(2.9) Geometric force on the time frequency domain function of the mechanical impedance	13
(2.10) Mechanical impedance	13
(2.11) Geometric force on the time domain	14
(2.12) Rearranged coefficient of variation	15
(2.13) Vertical displacement on the spatial domain (single sided and double sided spectrum) in MATLAB language	16
(2.14) Equation of motion of the MDOF system (displacement approach).....	16
(2.15) Geometric force on the time frequency domain function of displacements.....	16
(2.16) Geometric force on the time frequency domain function of dynamic stiffness	16
(2.17) Dynamic stiffness	16
(2.18) Contact stiffness for two crossed cylinders	19
(3.19) Wave equation in strings 1D	26
(3.20) Harmonic solution for the 1D wave equation in strings.....	26
(3.21) D'Alembert equation on the time and space domains.....	26
(3.22) Speed propagation of an harmonic wave or phase velocity	26
(3.23) Dispersion equation for strings.....	26
(3.24) Phase velocity in strings	27
(3.25) Wave equation in tensioned Euler-Bernoulli beam 1D.....	27
(3.26) Dispersion equation in tensioned Euler-Bernoulli beams.....	27
(3.27) Phase velocity in tensioned Euler-Bernoulli beams	27
(3.28) Group velocity in tensioned Euler-Bernoulli beams	27
(3.29) Harmonic solution for the 1D wave equation in strings (another solution)	28
(3.30) Boundary conditions of the string equation.....	28
(3.31) Relative error of velocities calculated under the two hypothesis	29
(3.32) Mode superposition method: analytic calculation of accelerations.....	30
(3.33) Amplitudes of the acceleration	30
(3.34) Angular frequencies.....	30
(3.35) Generalized coordinates vector	32
(3.36) Generalized coordinates vector for a tensioned beam	32

(3.37) Local mass matrix.....	32
(3.38) Local stiffness matrix	33
(3.39) Local mass matrix (with detailed components).....	33
(3.40) Local stiffness matrix (with detailed components).....	33
(3.41) Proportional damping matrix definition	33
(3.42) Local static force vector	34
(3.43) Global system of equations (static analysis).....	35
(3.44) Static deflection of the beam	35
(3.45) Global system of equations (dynamic analysis)	35
(3.46) Local vector of forces on the input point.....	36
(3.47) Approximation formulas of the Newmark method (velocity and displacement)	36
(3.48) Balance equation of the Newmark method.....	36
(3.49) Iteration matrix of the Newmark method	36
(3.50) Initial acceleration of the Newmark method	36
(3.51) Predictions of the Newmark method (velocity and displacement).....	37
(3.52) Acceleration of the new time step of the Newmark method	37
(3.53) Correction of the predictions of the Newmark method (velocity and displacement)....	37
(3.54) Link between the numerical dissipation parameters of Newmark method	37
(3.55) Gamma parameter restriction for unconditional stability.....	37
(3.56) Beta parameter restriction for unconditional stability	38
(3.57) Time step restriction for conditionally stable systems	38
(3.58) Aproximation formulas of the HHT- α method (velocity and displacement)	40
(3.59) Balance equation of the HHT- α method.....	40
(3.60) Iteration matrix of the HHT- α method	40
(3.61) Initial acceleration of the HHT- α method	40
(3.62) Predicions of the HHT- α method (velocity and displacement).....	41
(3.63) Acceleration of the new time step of the HHT- α method	41
(3.64) Correction of the predictions of the HHT- α method (velocity and displacement).....	41
(3.65) Spectral radius. First stability condition.....	41
(3.66) Eigenvalues of multiplicity 2. Second stability condition.....	41
(3.67) Numerical dissipation parameters function of α	42
(3.68) Range of used values of α -(negative)dissipation.....	43
(3.69) Phase velocity function of time frequency	46
(3.70) Sinusoidal force excitation definition.....	47
(4.71) Incident wave on the time and space domain.....	50
(4.72) Reflected wave on the time and space domain.....	50
(4.73) Transmitted wave on the time and space domain.....	50
(4.74) Newton's second law for a lumped mass (time and space domain).....	50
(4.75) Newton's second law for a lumped mass (time and space frequency domain).....	51
(4.76) Continuity of displacement at the origin	51
(4.77) System of equations on a matrix form.....	51
(4.78) Analytical expression of reflection and transmission coefficients	51
(4.79) Newton's second law for the lumped mass on the CW	54
(4.80) Newton's second law for the lumped mass on the MW	54

(4.81) Continuity of displacement on the CW	54
(4.82) Continuity of displacement on the MW	54
(4.83) Impedance definition on the dropper.....	54
(4.84) System of equations on a matrix form.....	54
(4.85) Analytical expression of reflection and transmission coefficients and the dropper impedance at the CW	55
(4.86) Reflection and transmission coefficients at $f=0\text{Hz}$	55
(4.87) Reflection and transmission coefficients at $f=0\text{Hz}$	55
(4.88) Analytical expression of reflection and transmission coefficients and the dropper impedance at the MW	57
(4.89) Definition of the mass drop needed to generate in the MW the same velocity step as in the CW.....	66
(4.90) Definition of the mass drop needed to generate an equal velocity step simultaneously on the two wires	69
(4.91) Simplified transmission coefficient at $f=0\text{Hz}$	69
(4.92) Weighted sum of the observed waves on the CW and the MW	69

Chapter 1

Introduction

The main characteristics of the sliding contact system and the problematic in analysis are introduced making a brief definition of the overall situation regarding the velocity limits on electrically tractioned high-speed railways.

1.1 Motivation

The maximum velocities in high-speed railway vehicles with electric traction are restricted by important physical and design factors. To facilitate the understanding of the role portrayed by the main constraints, these will be divided into two main groups: the mechanical stability and locomotion related constraints and the maximum power related constraints where the sliding contact system plays a central role. Although both groups are strictly linked by an integrated system, it is possible to differentiate them considering their main characteristics.

1.1.1 Mechanical Stability and Locomotion Constraints

Running stability during the whole range of reachable speeds is indispensable for vehicles, being the highest allowable velocities the most critical for the dynamic behaviour of the system. It is correlated to the “hunting mode”, critical on straight paths, which is the coupling of lateral displacements and yaw rotations of the wheelset. Stability depends on many design factors such as equivalent conicity of the wheels, damping of the hunting mode (longitudinal damping), lateral and longitudinal stiffness, gauge and play between the wheel and the railway between others.

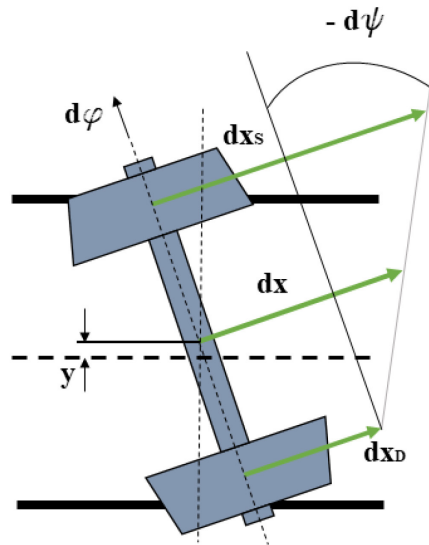


Figure 1. 1 Hunting mode, where y is the lateral displacement, $d\psi$ is the yaw rotation and $d\varphi$ is the rotation of the wheel axis. Adaptation from (Bosso, 2021)

For curve paths, stability is also a main issue due to the high derailment risk. Determined the curve radius, a maximum circulation velocity is established to guarantee a smooth movement for the passenger comfort and to minimize centrifugal forces causing train derailment.

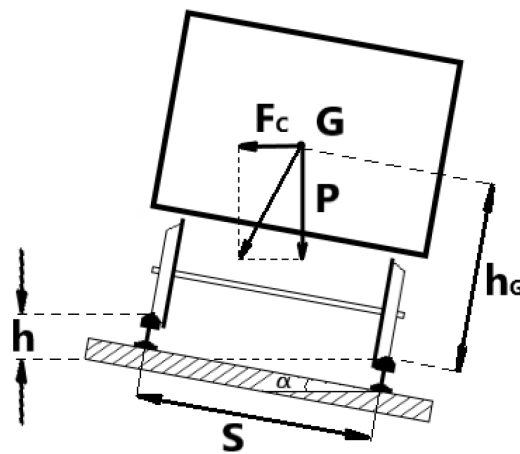


Figure 1. 2 Curve paths, with α the inclination of the rails plane, h the elevation of one of the rails respect to the other, G the centre of gravity of the train and F_c the centrifugal force and P the weight force. Adaptation from (Bosso, 2021).

To be able to obtain the motion of the vehicle, the generated traction force needs to be higher than the resistances that oppose to the movement and smaller than the adhesion limit of the system wheel-railway, the locomotion equation is:

$$R \leq T \leq f Pa$$

Where R is the resistance to the movement, T is the traction force, f is the friction coefficient of the wheel-railway contact and Pa is the adherent weight or the part of the total weight supported by the motorized wheels. Adhesion limit and total resistance to the movement are strongly related to the velocity, among other parameters. The friction coefficient is decreased with the increase of the velocity, decreasing the maximum reachable adhesion limit and restricting the superior limit for the traction force T .

To understand the movement resistance dependence on velocity it is necessary to divide it in two: the plano-altimetric resistances, that can be present or not, and the fundamental resistances, always opposed to motion. The plano-altimetric resistances' presence depends on the track nature (Antonucci, 1993):

$$R_L = \pm R_i + R_c \pm R_a$$

where R_i is the resistance due to the slope (additive for a positive slope and subtractive for a negative slope), R_c is the curve resistance and R_a is the acceleration/deceleration resistance (additive for deceleration and subtractive for acceleration). The fundamental resistances always oppose to the motion:

$$R_O = R_1 + R_2 \pm R_3$$

where R_1 is the resistance due to the viscous dissipations on the bearings and spindles, R_2 is the resistance on the wheel-railway contact due to the dissipation of the normal angular velocity component and R_3 is the aerodynamic resistance and it becomes one of the centres of discussion for high-speed train design.

Summarizing, an increase in velocity reduces the span of possible providable traction forces by increasing the lower limit (resistance) and decreasing the higher limit (adhesion limit). Moreover, by increasing the resistance to the motion, the required power delivered by the motor increases, as explained in (Bosso, 2021).

1.1.2 Maximum Power Constraints

The energy required to generate the motion of the vehicle is acquired from the contact between a pantograph, fixed to the train, and a power line or catenary, fixed to the ground. In this system it is possible to find some limitations; the constraints in the electric devices and cabling of the power unit, the ones related to the heat dissipation capacity and the ones regarding the energy acquisition system itself.

As explained in (Antonucci, 1993), electric devices such as transformers, inverters, rectifiers and filters suffer losses due to the power regulation procedures, due to Joule effect and have their own construction limits. The cabling network has its own power limitations imposed by the maximum tension, current (or conductor section) and, mainly, the Joule effect losses. This establishes a maximum admissible power for the line and for the vehicle.

The ability to dissipate heat in the devices' cabling regulates the capacity of power transmission inside the system. Poor dissipative capacities lead to lower admissible power,

increasing the risk of burning the internal cabling, while good dissipative capacities lead to a higher one.

The energy acquisition system consists, as previously discussed, in a sliding contact between two current-conducting bodies, the contact line and the pantograph. The regularity and dynamics of this contact determine the quality of the power collection and constitutes one of the main constraints for the maximum reachable velocities.

The main constraints of the system are summarized on *Figure 1. 1*.

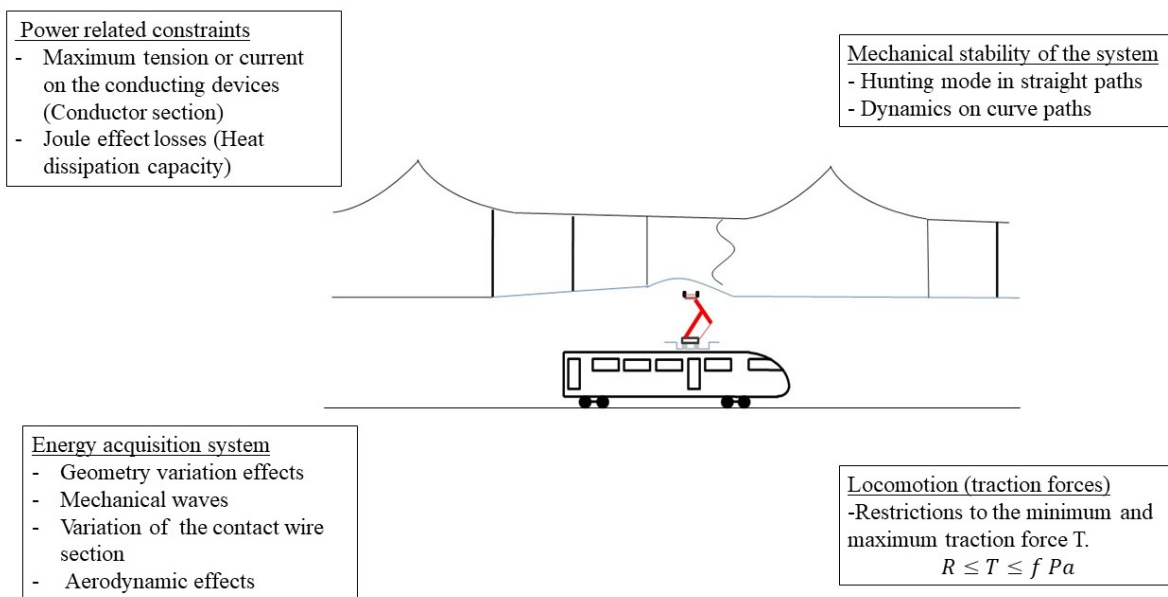


Figure 1. 3 Main constraints of the railway system. Adaptation from (Iwnicki, Spiryagin, Cole, & McSweeney, 2019)

1.2 Sliding Contact System Characteristics

Contact lines of high-speed railways are normally composed of two parallel cables, connected between them by droppers.

As defined by (Vo Van, 2016), the lower one is the contact wire (CW); it is electrified with a tension depending on the nature of the line and is the one in contact with the train's current collector device. It needs to have good mechanical resistance and high electrical conductivity; the used materials can be hard copper or alloys of copper and tin. The section of the wire is not exactly circular, it has grooves at two of its flanks needed to connect with the steady arms or droppers' claws (right side of *Figure 1. 4*).

A stagger is applied to the CW (+/- 20cm) by the so-called steady arm (SA) (left side of *Figure 1. 4*). This is done to distribute the wear along the whole pantograph contact line. The SA is always on traction, it is attached through a pivot to the registration arm (right side of

Figure 1. 5) which is then connected to the bracket by another pivot link. The SA introduces low stiffness to the wire, allowing its vertical and horizontal motions.

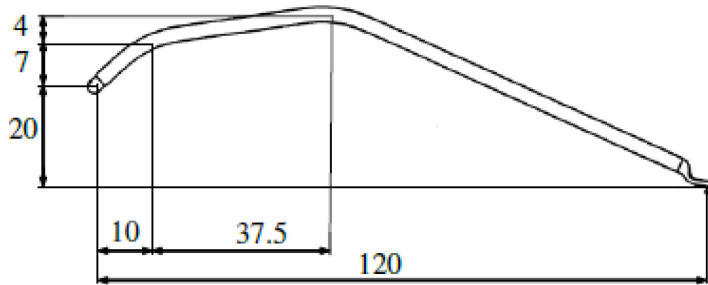


Figure 1. 4 Steady arm with its dimensions (left side). Contact wire section (right side). From (Vo Van, 2016).

To keep the CW as flat as possible, an upper cable is used. The so-called messenger wire (MW) supports the CW by using the droppers, distributed along each span. Thanks to its deflection along each span, the system receives the name of catenary. The MW is a braided wire composed of 37 yarns of bronze and it is connected to the bracket (centre of *Figure 1. 5*). The bracket is linked to the mast by two pivots allowing the wires to move longitudinally and constraining any vertical or horizontal motions (left side of *Figure 1. 5*).



Figure 1. 5 Joints between bracket and mast (left side), messenger wire and bracket (centre) and registration arm and steady arm (right side). From (Vo Van, 2016).

The power line is divided into spans of equal length delimited by masts working as support of the catenary. It is possible to consider a periodic geometry of the cables, with a period equal to the distance between two masts.

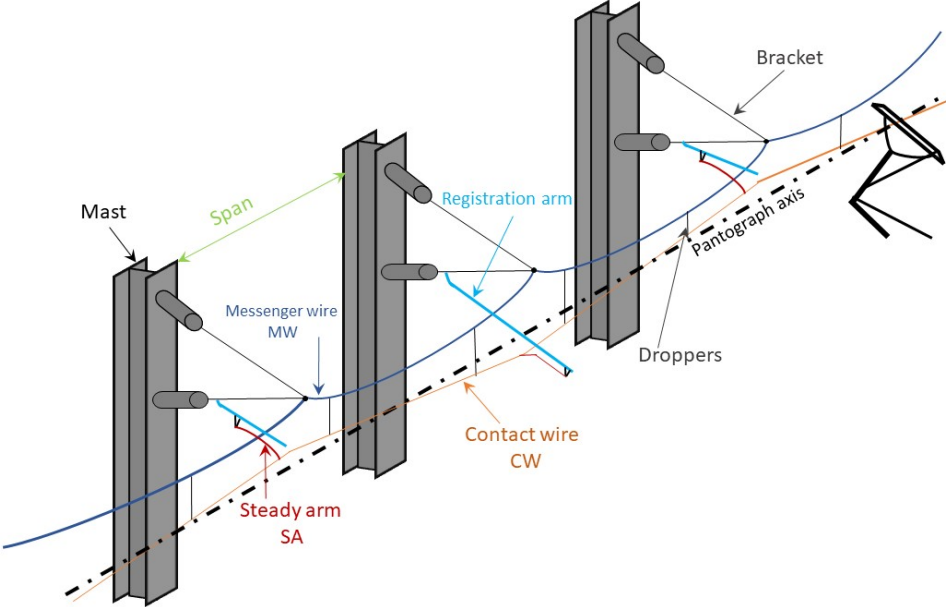
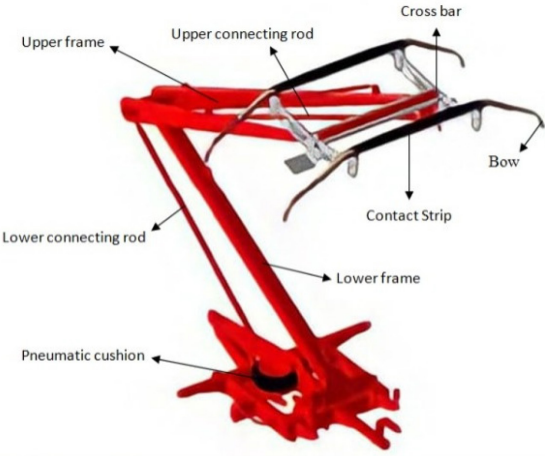


Figure 1. 6 Sliding contact system scheme. Adaptation from (Vo Van, 2016)

One or more current collector devices or pantographs are attached to the train. It consists in an assembly of articulated tubes fixed to the roof of the train, positioned on the locomotive or near it. The main function of the pantograph is, by means of sliding contact, collect current from the CW at a constant rate keeping the contact area as constant as possible. (Iwnicki, Spiriyagin, Cole, & McSweeney, 2019). To maintain this contact area constant, forces must be generated by the pantograph.

The main structure of the pantograph consists in the bow and the large frame. An historical pantograph used for high voltage/velocity lines in Italy is the ATR95, with the bow made of copper or graphite.



The interaction between pantograph and catenary is subject to dynamic fluctuations generated by many factors. These dynamic fluctuations generate discontinuities on the contact pressure and thus on the current collection.

To ensure a proper contact, limits for the contact force must be defined. High contact forces may produce excessive wear on the CW or the pantograph while low contact forces increment the resistance of the conduction with a decrease in the quality of current collection. A low contact force increases the risk of contact loss with the possibility of inducing current arcs between the two conductors.

Electric arcs are particularly dangerous mainly for two reasons. The first is that they produce a discontinuity and peak in current at high frequencies, generating electromagnetic distortions that affect the electric devices inside the vehicle. The second reason is that the electric arc, instead of being distributed in a contact area, is concentrated on a point. In this point a localized fusion is produced damaging the pantograph and contact wire surfaces. (Bosso, 2021)

Excessive fluctuations in the defined contact force are not wanted since they certainly produce variations in the collected current. The allowable variation of the contact force is:

$$\frac{\sigma}{F_m} < 0.3 \quad (1.1)$$

where σ is the standard deviation of the contact force and F_m is the mean contact force.

Force fluctuations depend mainly on the spatially variable geometry and stiffness of the CW on the vertical direction and, for high speeds, on phenomena as wave dispersion. Other characteristics such as section variation of the CW due to wear and ice formation can also affect the system. Aerodynamic forces are also an important factor for the dynamic analysis of the contact at high velocities.

1.3 Structure of the Thesis

As explained in *Section 1.2* two of the main sources of variation of the contact force are the geometry of the catenary and the mechanical waves generated on the contact and messenger wires.

In *Chapter 2* the main characteristics of the so-called geometric force are defined with the help of an analytic model of the catenary-pantograph system (*Section 2.1*). In this chapter the wires of the catenary are considered to be rigid, so no influence of mechanical waves is taken into account. Two approaches are considered for solving the analytic problem with two different inputs in *Sections 2.2* and *2.3*: the first using the vertical *velocity* of the contact point and the preload as inputs and the second one using the vertical *displacement* of the contact point and the preload as inputs. The concept of contact stiffness is introduced in *Section 2.4*, together

with an analysis of its convergence in modelled results for different frequency bandwidths of analysis.

Wave dispersion is introduced and analysed in *Section 3.1* of *Chapter 3*. An analytic model is presented for the definition of the phenomena in *Section 3.2*. On *Section 3.3* main aspects of FEM analysis are introduced and the discretization of the tensioned beam is realized with Euler-Bernoulli beam elements. The main characteristics of the Newmark and HHT- α numerical methods are defined for the resolution of differential equations in the time. The response in time of the discretized model is studied for an impulsive load to compare the differences between both methods. Finally, the dependence of wave velocity on frequency is analysed with a sinusoidal input on *Section 3.4*.

Wave transmission and reflection are analysed in *Chapter 4*. On *Section 4.1* these phenomena are introduced for a simple case of a lumped mass. Transmission and reflection characteristics of the system are studied for a path with and without masses. A more complete model is used in *Section 4.2*, to take into account the joint motion of the whole catenary system, connected through droppers. This new model is studied for a step velocity wave as input, simulating a mass drop, on a single wire (with a mass drop on the contact wire and another on the messenger wire) and for a step velocity wave as input on the two wires contemporarily (with a mass drop below a dropper linking both wires). At the end of this section the analytic model is exploited to study the wave behaviours on the droppers around the mast. Finally, on *Section 4.3*, the analytic results are compared with simulated results using a discretized catenary model. For the resolution in time of the discretized system, two numerical methods (Newmark method and HHT- α method) are used to analyse their main features.

On *Chapter 5* the main aspects of the results are explained and a conclusion for each of the studies is elaborated. Some complementary works are proposed for further studies on *Section 5.2*.

Finally, on the Appendices section, supplementary information is added for the understanding of some of the experiments carried on along the study.

Chapter 2

Variable Geometry Effects

On the first section the analytic contact model is presented with all its main characteristics. For the second and third section, two different paths are chosen in the resolution of the problem: one considering the vertical velocity as an input and the other considering the vertical displacement as an input. Finally, on section four, the convergence nature of the system is explained with the definition of contact stiffness.

2.1 Analytic Model

To begin the analysis a CW span is designed on *Figure 2.1* using the geometry described in EN50318 ((CENELEC), 2018), having periodic spans in an interval of 1375 meters with two boundary spans at the extremes. The geometry of the deflections of each span can be defined by its Fourier transform in the space domain $H_{CW}(k)$. *Figure 2.1* shows the deflection of the first two spans.

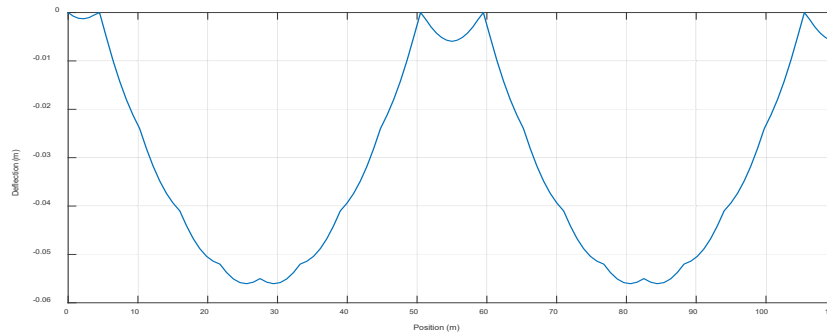


Figure 2.1 Deflection of two spans

The pantograph is modelled by a lumped, multi degree of freedom (MDOF) system with 3 masses, dampers and springs on each of the degrees of freedom (DOF). The values of the lumped parameters are defined in EN50318 ((CENELEC), 2018). It travels through the catenary at a velocity v_{panto} . The contact wire is considered to be rigid, thus, the reflected and transmitted waves represented on the scheme of Figure 2. 2 ($V_{r,panto}$, $V_{t-,panto}$, and $V_{t+,panto}$) are null.

The inputs of the system are the vertical displacement or velocity due to the geometry variation on the space frequency domain ($V_{CW}(k)$), defined in Sections 2.2 and 2.3, and the preload force applied on the first degree of freedom (F_0).

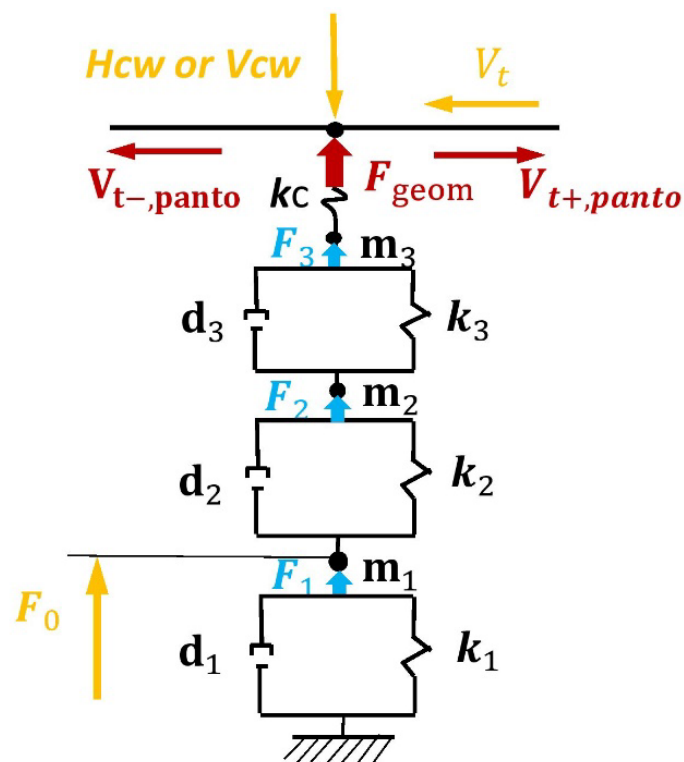


Figure 2. 2 Pantograph and contact wire model. Adaptation from (Vo Van, 2016)

For the analytic sliding contact model, no friction and aerodynamic forces are taken into account, and the contact and displacement are considered to take place without further restrictions

2.2 Analysis with Spatial Velocity as an Input

The vertical spatial velocity, on the spatial frequency domain, is the velocity of height variation of the CW, generated by the geometry of each span as seen in *Figure 2. 3*, and is defined as:

$$V_{CW}(k) = i \frac{k}{2\pi} \cdot H_{CW}(k) \quad (2.2)$$

where $H_{CW}(k)$ is the Fourier transform of the geometry of the catenary and k is the spatial frequency or wave number in [rad/m], calculated from the spatial frequency f_x in [1/m] as:

$$k = f_x \cdot 2\pi \quad (2.3)$$

Velocity of height variation in the spatial frequency domain is shown in *Figure 2. 3*.

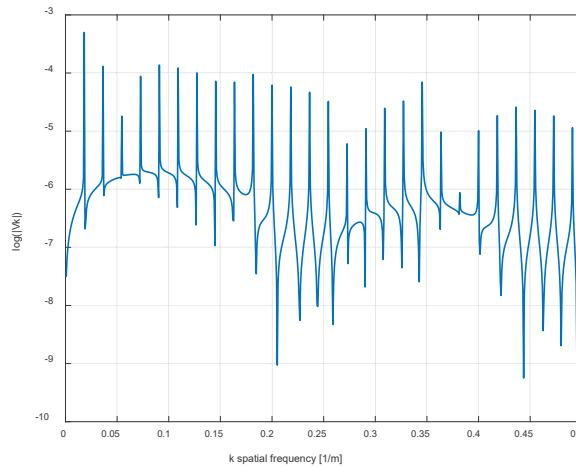


Figure 2. 3 Velocity in the spatial frequency domain

The Discrete Fourier transform of the catenary geometry is obtained by using the FFT algorithm (Fast Fourier Transform) from MATLAB. It is generally recommended to operate with a number of points equal to an integer power of 2. If this is not possible, the so called zero padding is applied by inserting zeros in order to obtain an integer power of 2, as explained in (Fasana & Marchesiello).

As previously said, the input for the FFT function is the catenary geometry in the space domain while its output is the double-sided spectrum of frequencies in the spatial frequency domain. For engineering analysis, only the positive frequencies are used.

From the guides (MATLAB, 2021), the single sided spectrum is obtained in MATLAB language, by:

$$\begin{aligned}
 H_{cWDS}(k) &= \text{fft}(h_{cW}(x), N_x) / N_x \\
 H_{cWSS}(k) &= 2 * H_{cWDS}(k)(1:N_{x2})
 \end{aligned}
 \tag{2.4}$$

where h_{cW} is the height of the catenary as function of the position, N_x is the number of spectral lines N_{x2} is the number of spectral lines representing approximately the single sided spectrum. (See *Appendix C*)

The angular frequency and the wave number are related by the relationship:

$$\omega = v_{panto} \cdot k \tag{2.5}$$

Finally, with *equation (2.5)* it is possible to define the vertical velocity on the time frequency domain as:

$$V_{CW}(\omega) = v_{panto} \cdot V_{CW}(k) \tag{2.6}$$

In this case, the pantograph velocity is the constant used to pass from the spatial frequency domain to the temporal frequency domain.

To begin with the calculation of the frequency response function or mechanical impedance and the force, the equations of motion of the MDOF system in a matrix form are defined as:

$$\begin{aligned}
 &\begin{bmatrix} m_1 & 0 & 0 \\ 0 & m_2 & 0 \\ 0 & 0 & m_3 \end{bmatrix} i\omega + \begin{bmatrix} d_1 + d_2 & -d_2 & 0 \\ -d_2 & d_2 + d_3 & -d_3 \\ 0 & -d_3 & d_3 \end{bmatrix} \\
 &+ \begin{bmatrix} k_1 + k_2 & -k_2 & 0 \\ -k_2 & k_2 + k_3 & -k_3 \\ 0 & -k_3 & k_3 + k_c \end{bmatrix} \frac{1}{i\omega} \cdot \begin{Bmatrix} V_1 \\ V_2 \\ V_3 \end{Bmatrix} = \begin{Bmatrix} F_0 \\ 0 \\ \frac{k_c}{i\omega} V_{CW}(\omega) \end{Bmatrix}
 \end{aligned}
 \tag{2.7}$$

where F_0 is the preload, k_c is the contact stiffness and V_1 , V_2 and V_3 are the vertical velocities of the three degrees of freedom. Thus, the resulting vertical geometric force in the temporal frequency domain is:

$$F_{geom}(\omega) = \frac{k_c}{i\omega} \cdot (V_{CW}(\omega) - V_3(\omega)) \tag{2.8}$$

Calling the left matrix of *equation (2.7) matrix [A]*, and substituting $V_3(\omega)$ in *equation (2.8)*, the geometric force becomes:

$$F_{geom}(\omega) = \frac{k_c}{i\omega} \cdot \left(1 - (A^{-1})_{3,3} \cdot \frac{k_c}{i\omega}\right) \cdot V_{CW}(\omega) + \frac{k_c}{i\omega} \cdot (A^{-1})_{3,1} \cdot F_0 \quad (2.9)$$

$$F_{geom}(\omega) = v_{panto} \cdot Z_{panto}(\omega) \cdot V_{CW}(\omega) + F_m$$

The mechanical impedance, $Z_{panto}(\omega)$, is defined as the amplitude of the force over the amplitude of velocity, both of them in the frequency domain:

$$Z_{panto}(\omega) = \frac{F_{geom}(\omega) + F_m}{V_{CW}(\omega)} \quad (2.10)$$

with the preload $F_m = 0$ for each $\omega \neq 0$.

2.2.1 Mechanical Impedance

The parameters used for the analysis of the pantograph-catenary model are summarized on *Table 2.1*

Parameter	Value	Description
m1	20	Mass of DOF 1 [kg]
m2	10	Mass of DOF 2 [kg]
m3	6	Mass of DOF 3 [kg]
d1	100	Damping Coefficient of DOF 1 [Nm/s]
d2	0.1	Damping Coefficient of DOF 2 [Nm/s]
d3	45	Damping Coefficient of DOF 3 [Nm/s]
k1	160	Stiffness of DOF 1 [N/m]
k2	15500	Stiffness of DOF 1 [N/m]
k3	7000	Stiffness of DOF 1 [N/m]
F0	169	Preload Force applied on DOF 1 [N]
kc	-	Contact Stiffness [N/m]

Table 2.1 Parameters of the pantograph-catenary model

The mechanical impedance from *equation (2.10)* is calculated for three different contact stiffnesses k_c .

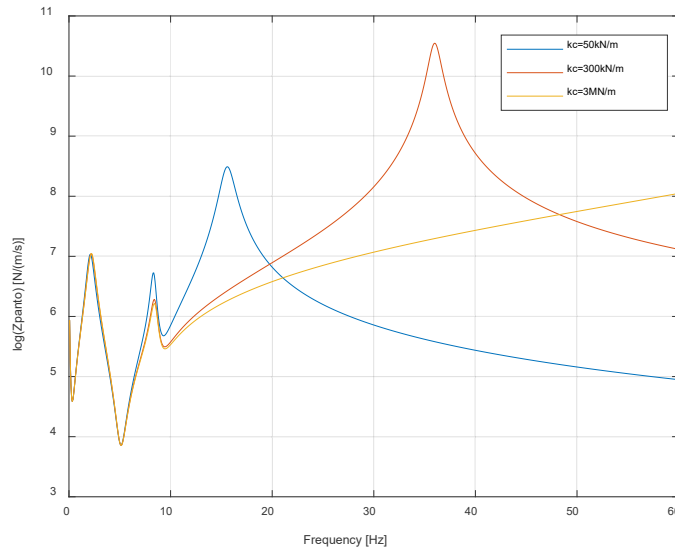


Figure 2.4 Mechanical impedance in the frequency domain for three different contact stiffness k_c

It is possible to observe that three resonance frequencies, equal to the number of DOF ($N_{dof} = 3$), and two anti-resonance frequencies ($N_{dof} - 1 = 2$) are present in the plot for the two mechanical impedance functions of the two lower contact stiffness values. As the stiffness contact is increased, the third resonance frequency moves towards higher frequencies while the first two resonance frequencies and all the anti-resonance frequencies remain constant. This is correct since the variation of the contact stiffness affects mainly the third DOF of the system.

The contact stiffness is a parameter introduced to model the contact but, its variation modifies the frequency response of the system. Thus, geometrical force variations induced by the change in the dynamic are incorrect. Further studies are done in *Section 2.4*.

2.2.2 Geometric Force

The geometric force in the time domain was calculated using *equation (2.8)* or *equation (2.9)* and the IFFT function (Inverse Fast Fourier transform) from MATLAB for two different pantograph velocities, 90 km/h and 320 km/h. (MATLAB, 2021)

The constants used to calculate the single-sided spectrum in *equation (2.4)* must be taken into account in the calculation of the geometric force in the time domain, in MATLAB language, as

$$F_{geom}(t) = \text{ifft}(F_{geom}(\omega), 'symmetric') * N_{x2}/2 \quad (2.11)$$

Since works are done in a single-sided spectrum, the symmetry of the spectrum must be specified on the ifft function. An analogous analysis is done in the *Appendix C* for a sinusoidal input.

To constrain the frequency domain to the traditional bandwidth as proposed in the European standard ((CENELEC), 2018) a Butterworth low pass filter of order 6 is placed at 20Hz (see *Appendix D*). The obtained results are

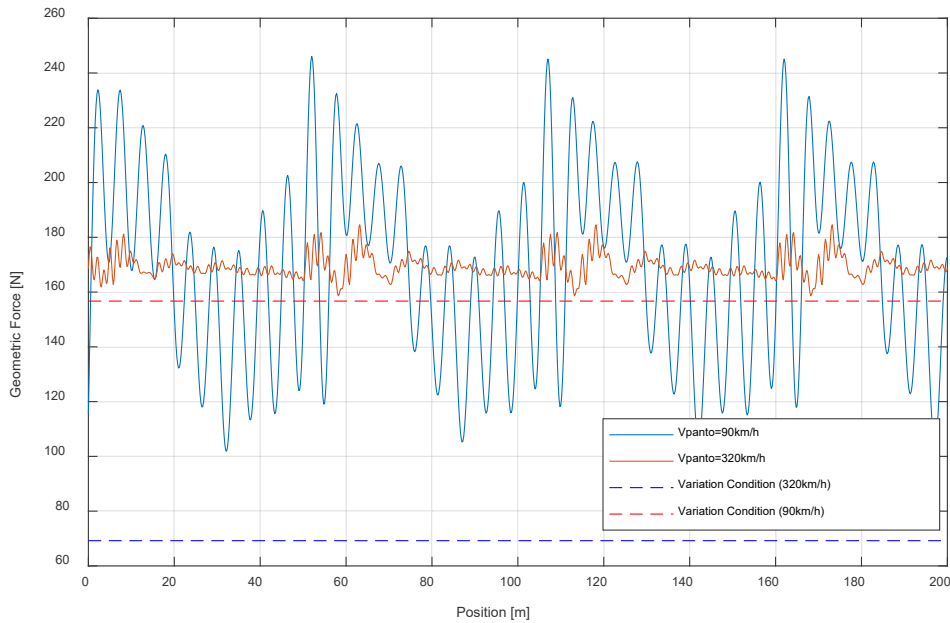


Figure 2. 5 Contact force at 90 km/h (red) and 320 km/h (blue) for a contact stiffness $k_c = 50kN$

Force variations along the delimited path are periodic with a period length equal to the length of each span. This is consistent with the geometry of the system. In *Figure 2. 5* two horizontal lines are observed, they correspond to the coefficient of variation defined in *equation (1.1)* and can be analogously written as the limit

$$F_m - 3 * \sigma > 0 \quad (2.12)$$

2.3 Analysis with Spatial Displacement as an Input

For this case, analysis is done from the Fourier transform of the geometry of the catenary $H_{CW}(k)$ and k .

The Discrete Fourier transform of the catenary geometry is obtained by using the FFT algorithm (fast Fourier transform) from MATLAB. As previously said, the input for the *fft* function is the catenary geometry in the space domain while its output is the double-sided spectrum of frequencies in the spatial frequency domain. For engineering analysis, only the positive frequencies are used.

From the guides (MATLAB, 2021), the single sided spectrum is obtained in MATLAB language, by:

$$\begin{aligned}
 H_{cWDS}(k) &= \text{fft}(h_{cW}(x), N_x)/N_x \\
 H_{cWSS}(k) &= 2 \cdot H_{cWDS}(k)(1:N_{x2})
 \end{aligned}
 \tag{2.13}$$

where h_{cW} is the height of the catenary as function of the position, N_x is the number of points where the algorithm is going to be performed and N_{x2} is half of the number of points.

To begin with the calculation of the frequency response function or dynamic stiffness the force, the equations of motion of the MDOF system in a matrix form are defined in an analogous way as in *equation (2.7)*

$$\begin{aligned}
 &\left[-\omega^2 \cdot \begin{bmatrix} m_1 & 0 & 0 \\ 0 & m_2 & 0 \\ 0 & 0 & m_3 \end{bmatrix} + i\omega \cdot \begin{bmatrix} d_1 + d_2 & -d_2 & 0 \\ -d_2 & d_2 + d_3 & -d_3 \\ 0 & -d_3 & d_3 \end{bmatrix} \right. \\
 &\quad \left. + \begin{bmatrix} k_1 + k_2 & -k_2 & 0 \\ -k_2 & k_2 + k_3 & -k_3 \\ 0 & -k_3 & k_3 + k_c \end{bmatrix} \right] \cdot \begin{Bmatrix} y_1 \\ y_2 \\ y_3 \end{Bmatrix} = \begin{Bmatrix} F_0 \\ 0 \\ k_c H_{cW}(\omega) \end{Bmatrix}
 \end{aligned}
 \tag{2.14}$$

where F_0 is the preload, k_c is the contact stiffness and y_3 is the velocity in the vertical direction.

Thus, the resulting vertical geometric force in the time frequency domain is:

$$F_{geom}(\omega) = k_c \cdot (H_{cW}(\omega) - y_3(\omega))
 \tag{2.15}$$

Calling the left matrix of *equation (2.14)* matrix $[A]$, and replacing $y_3(\omega)$ in *equation (2.15)*, the geometric force becomes:

$$\begin{aligned}
 F_{geom}(\omega) &= k_c \cdot (1 - (A^{-1})_{3,3} \cdot k_c) \cdot H_{cW}(\omega) + k_c \cdot (A^{-1})_{3,1} \cdot F_0 \\
 F_{geom}(\omega) &= D_{panto}(\omega) \cdot H_{cW}(\omega) + F_m
 \end{aligned}
 \tag{2.16}$$

The dynamic stiffness is defined as the amplitudes of force over the velocity, both in the frequency domain:

$$D_{panto}(\omega) = \frac{F_{geom}(\omega) + F_m}{H_{cW}(\omega)}
 \tag{2.17}$$

with the preload $F_m = 0$ for each $\omega \neq 0$.

2.3.1 Dynamic Stiffness

With the parameters summarized on *Table 2. 1* and *equation (2.17)*, the dynamic stiffness is calculated for three different values of contact stiffness k_c .

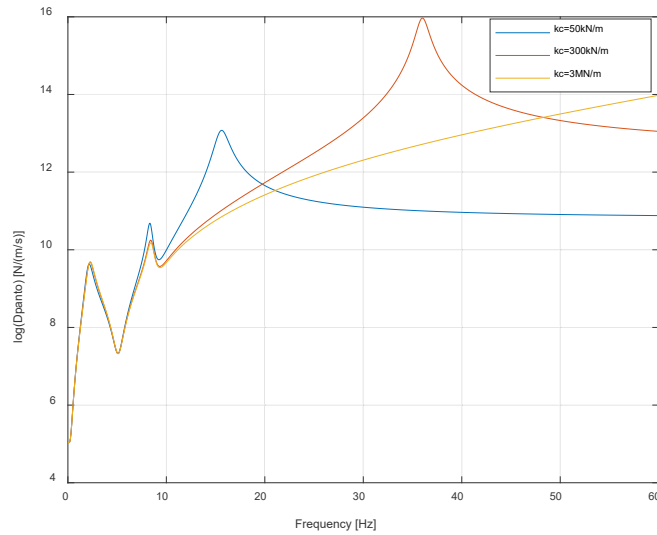


Figure 2. 6 Dynamic stiffness in the frequency domain for three different contact stiffnesses k_c

Analogously to *Figure 2. 5*, it is possible to observe that three resonance frequencies, equal to the number of DOF ($N_{dof}^{\circ} = 3$), and two anti-resonance frequencies ($N_{dof}^{\circ} - 1 = 2$) are present in the plot for the two dynamic stiffness functions of the two lower contact stiffness values. As the stiffness contact is increased, the third resonance frequency moves towards higher frequencies while the first two resonance frequencies and all the anti-resonance frequencies remain constant. This is correct since the variation of the contact stiffness affects mainly the third DOF of the system and its effect is uncoupled from the first two. Further studies on the contact stiffness effects are done in *Section 2.4*.

2.3.2 Geometric Force

The geometric force in the time domain is calculated with *equation (2.11)*, following the same procedure explained in *Appendix A* for a sinusoidal input. The force is calculated for three different values of contact stiffness k_c and the obtained forces are compared with the resulting forces calculated with the velocity approach. Results are plotted in *Figure 2. 7*.

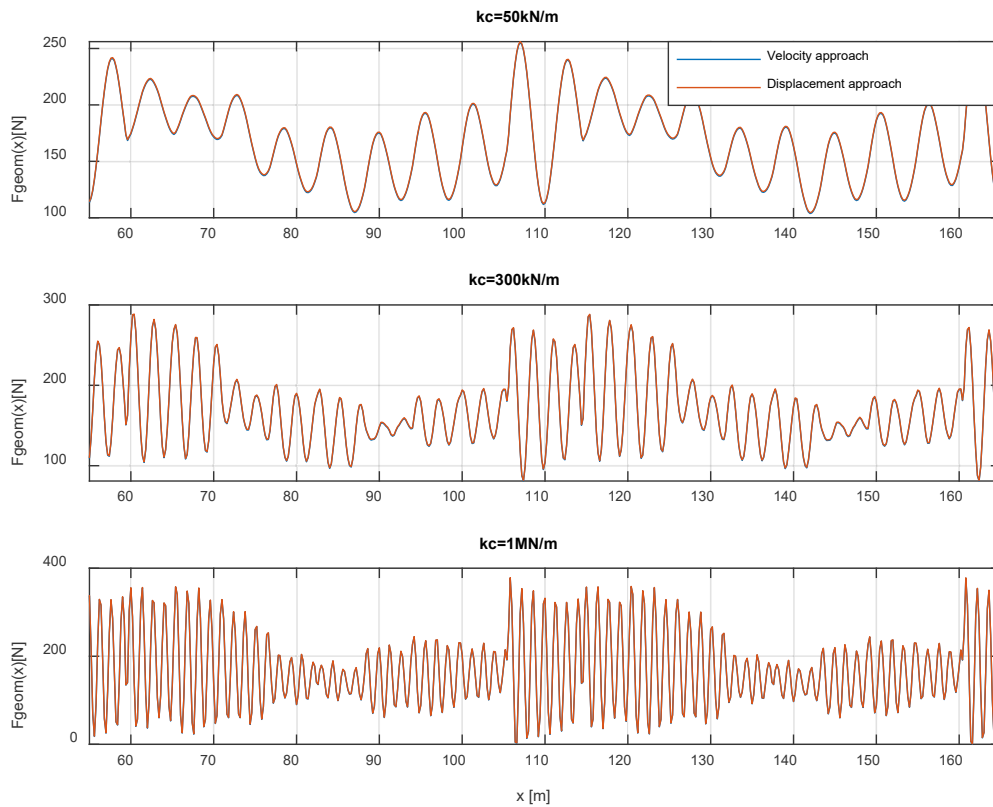


Figure 2. 7 Force comparison between the velocity and displacement approaches

The obtained results show an optimum confluence between both approaches. Nevertheless, for values of k_c higher or equal to 1MN/m, the geometric force takes values near 0. This behaviour might be associated to numerical problems.

It is possible to see that k_c is behaving analogously to a low pass filter, cutting higher frequencies for different values.

2.4 Convergence – Contact Stiffness

As explained in (Vo Van, 2016), contact between two surfaces generate forces that contain the penetration. The model proposed by Signorini for deformable objects interacting with rigid static bodies (Signorini, 1959) is typically used, it states that the gap between surfaces can only be positive and that for a gap equal to zero forces can develop. With the Hertz contact theory, see (Popov, 2010), the contact area is considered small compared to the whole dimensions analysed, hence, it introduces a contact stiffness to represent small deformations compatible with the Signorini model.

In the case of the contact between pantograph and catenary, small contact area relative to the whole system dimensions applies and Hertz contact theory can be used. For a contact between two crossed cylinders, the contact stiffness is equal to

$$k_c = 2 a E^* \quad (2.18)$$

with a equal to the radius of the contact surface (circular), and E^* the reduced modulus of the less rigid material.

The mechanical impedance is calculated for 3 different values of k_c and shown in *Figure 2. 4*, where it can be seen that the maximum resonances are strongly modified by the contact stiffness, modifying at the same time the geometric force as seen in *equation (2.9)*. This effect is not realistic, in *Figure 2. 7* strongly variations for the geometric force can be seen in the forces for different value of k_c , in concordance with the results shown in *Figure 2. 4*. For these, an optimized value of k_c must be calculated.

The usual frequency bandwidth used for the study of the contact force is from 0 to 20Hz. Another possible frequency bandwidth of interest is from 0 to 70Hz, which is where the dominant frequencies within the embankment of high-speed trains are located, as explained in (Connolly, et al., 2014) . The main objective is to find a value of k_c that take the third resonance generated as far as possible from the bandwidth of interest, respecting the stability condition of *equation (1.1)*. Hence, optimized values suitable for the first [0 – 20Hz] and second [0 – 70Hz] bandwidths will be calculated.

The first proposed path is to locate the optimized values with the mean force and the standard deviation calculated for each signal (*equation (1.1)*). The quotient is calculated for different values of k_c in *Figure 2. 8*.

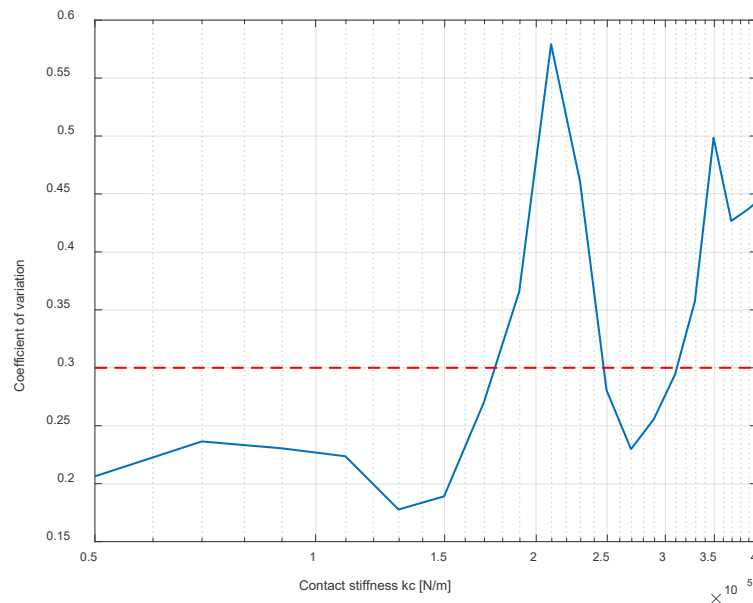


Figure 2. 8 Variation coefficient of the non-filtered force function of the contact stiffness

A clear peak in the variation coefficient is spotted for contact stiffness at around 200 kN/m, trespassing the stability limit (red pointed line). This behaviour could be due to numerical problems in the calculation of the forces. For the whole spectrum of frequencies a suitable value

(the maximum possible before the convergence problems) for k_c may be 150kN/m, being before the *numerical* peak. The geometrical force on the frequency domain is for $k_c = 150\text{kN/m}$ is plotted in *Figure 2. 9*.

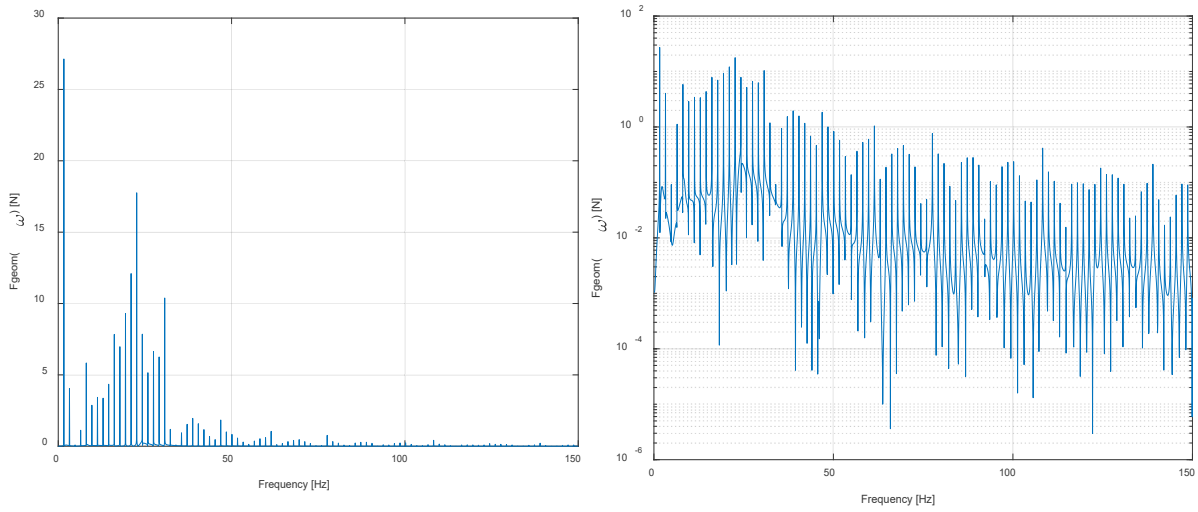


Figure 2. 9 Amplitude spectrum of the non-filtered geometric contact force

Nevertheless, for $k_c = 150\text{kN/m}$, the resonance frequency is placed inside the frequency bands of interest that were previously introduced. A detailed analysis for filtered force components must be done to find more appropriate results.

The variation coefficients for filtered force component at 20Hz are plotted in *Figure 2. 10*. The filtering is done with a low-pass Butterworth filter of order 6 (see *Appendix D*).

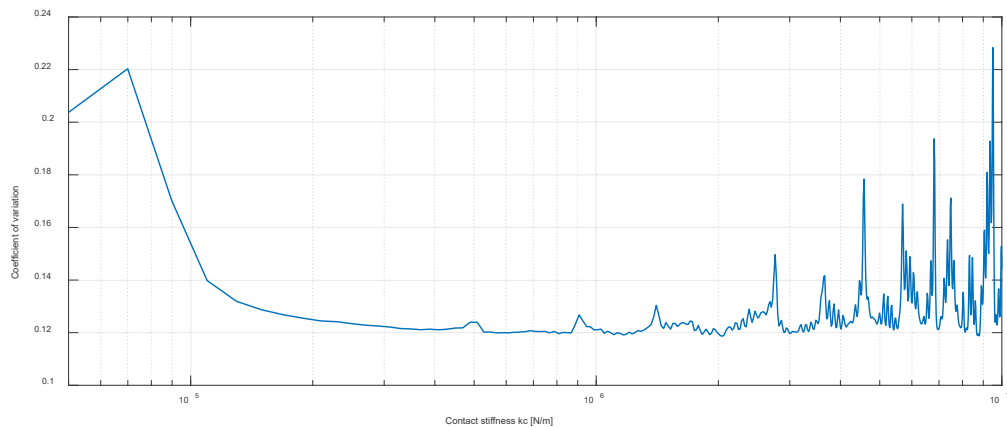


Figure 2. 10 Variation coefficient of the 20Hz-filtered force function of the contact stiffness

For the study of the frequency bandwidth from [0 - 20Hz] a wider range of possible contact stiffness values is accepted. Nevertheless, a possible numerically unstable region is

spotted after 2.5 MN/m. Values of k_c are chosen for analysis and their generated geometric forces plotted on the frequency domain to determine the most suitable one.

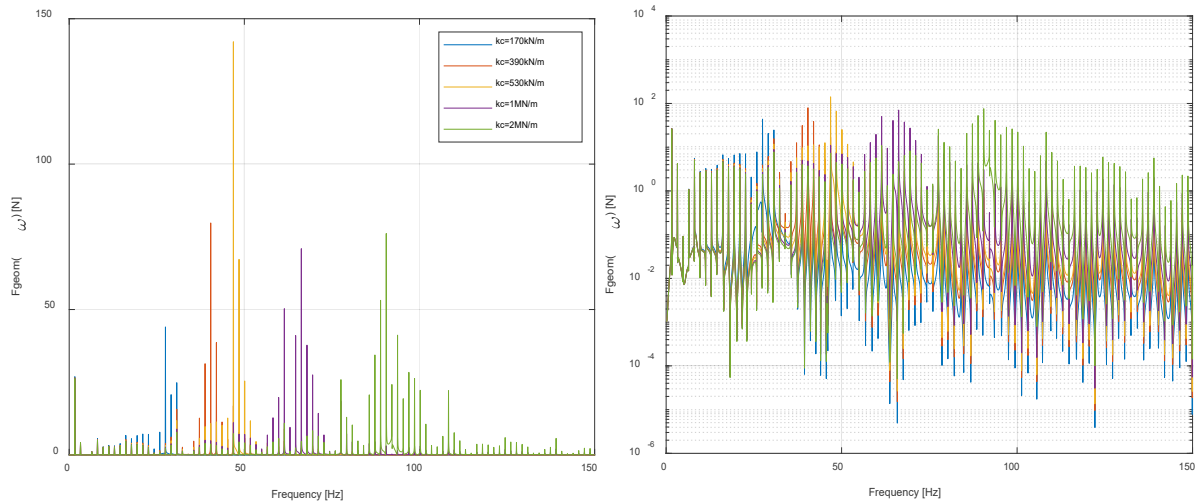


Figure 2. 11 Amplitude spectrum of the non-filtered geometric contact force for different contact stiffness values

It is possible to observe that for values of 170 kN/m, the resonance frequency of the third mode lies at around 27 Hz, this may be acceptable for working on bandwidths of [0 - 20Hz]. Lower values of contact stiffness tend to move the resonance peak towards the lower frequencies so it could be said that a lower limit for the contact stiffness values in 20Hz-filtered force analysis is 170kN/m. Any value greater than that moves away the resonance frequency “clearing” the area of work.

Higher limits may be established by the numerical uncertainties so, by looking in *Figure 2. 10*, this limit could be established to be at 1MN/m since, for higher values, fluctuations are spotted.

In the case of the second bandwidth [0 - 70Hz] constraints are more demanding. Values of stiffness below 170 kN/m are discarded due to the third resonance presence. Moreover, the stiffness range from 150kN/m to 1.5MN/m is dominated by numerical oscillations and problems of convergence arise. Nevertheless, for values above 1.5MN/m convergence in the system seems to return *Figure 2. 12*.

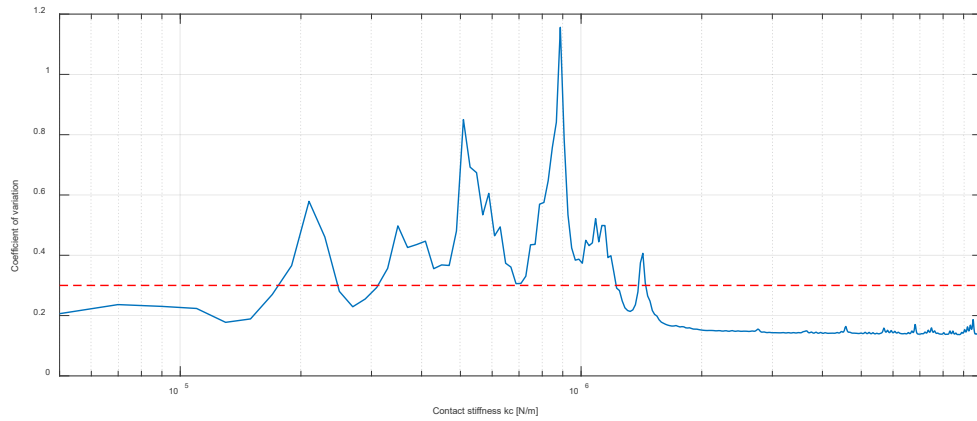


Figure 2. 12 Variation coefficient of the 70Hz-filtered force function of the contact stiffness

Values of $\approx 50\text{kN}$ are chosen for analysis and their generated geometric forces plotted on the frequency domain to determine the most suitable one.

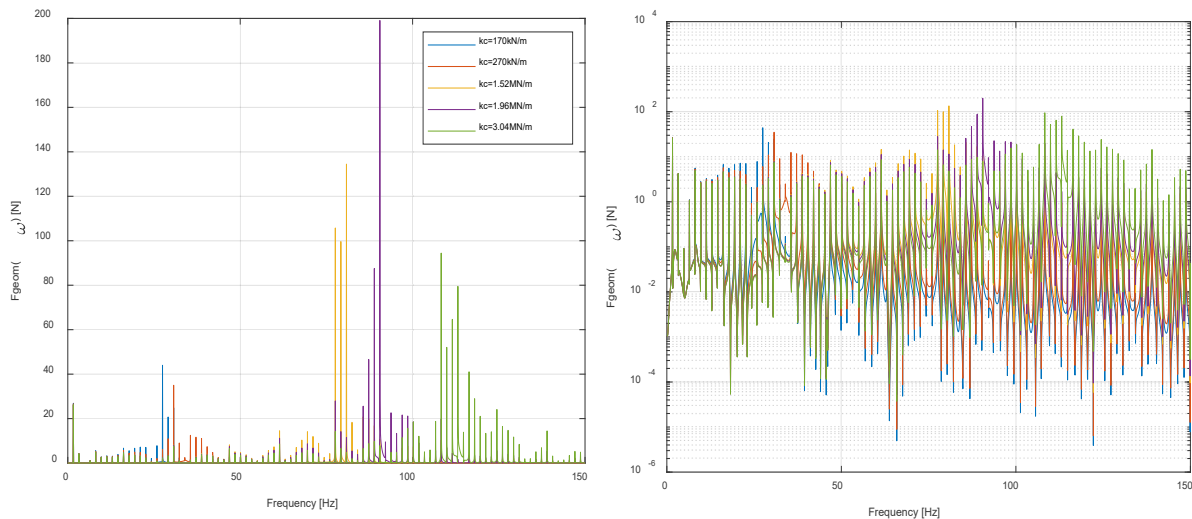


Figure 2. 13 Amplitude spectrum of the non-filtered geometric contact force for different contact stiffness values

For values below 1.52 MN/m, the resonance frequency of the third mode lies inside the bandwidth of interest and they must be discarded. A lower limit may be defined at around 1.9 MN/m, with resonance frequency at around 90 Hz. Any value greater than that moves away the resonance frequency “clearing” the area of work. These results are coherent with the ones obtained by (Vo Van, 2016).

However, the regions of numerical instability found in *Figure 2. 10* and *Figure 2. 12* must be interpreted and the results obtained for the bandwidth [0 - 70Hz] controlled.

A final comment must be done on the influence of the mass on the third degree of freedom (m_3). The third resonance can be approximated as $\sqrt{\frac{k_c}{m_3}}$, thus, its effects are crucial. In the

previously studies the used mass was equal to 6 kg. Heavier masses move the resonance frequencies towards lower frequencies, generating the need of higher contact stiffnesses.

As a conclusion, the contact stiffness should be high enough to maintain the resonance frequencies away from the frequency bandwidth of interest and small enough not to reach values with numerical or convergence problems.

Chapter 3

Mechanical Wave Effects -

Dispersion

In this chapter, dispersive effects are analysed. On the first section dispersion is defined and two models are introduced: the string model (non-dispersive) and the tensioned Euler-Bernoulli beam model (dispersive). To evidence the effects of dispersion an analytic model is proposed and analysed in *Section 3.2*. In *Section 3.3* a finite element analysis of the beam presented in the analytic model and its time behaviour is analysed with two numerical methods for the resolution of differential equations in time: α -method and Newmark method. Finally, the effects of the dispersive effects on waves velocities are analysed in *Section 3.4* for different time steps.

3.1 Dispersion

The contact wire is a semi-rigid tensioned copper cable; its geometry resembles a catenary. Inside this mean, mechanical waves are generated due to the irregularities of the contact and propagate along the whole structure impacting directly on the dynamics of the system.

The catenary can be modelled as a simply supported, tensioned Euler Bernoulli beam. Longitudinal waves are neglected and the motions on the vertical plane are considered to be uncoupled from the motions on the horizontal one as explained in (Genta, 2009).

Vibrations in beams can be studied by following the logic presented on (Morse , 1948). In string model, the string is completely flexible and under an applied tension working as a restoring force. Introducing the hypothesis of small oscillations (components of the force in the longitudinal direction are neglected) and considering that the tension is constant over the length of the string, its equation of motion or “1D wave equation in strings” is:

$$\mu \frac{\partial^2 z(x, t)}{\partial t^2} - T \frac{\partial^2 z(x, t)}{\partial x^2} = f(x, t) \quad (3.19)$$

with μ being the distributed mass per unit of length $[Kg/m]$, T the tension of the string $[N]$, $f(x, t)$ the external force $[N]$ and $z(x, t)$ the vertical displacement, with a harmonic solution of the type

$$z(x, t) = A \sin(kx - \omega t) \quad (3.20)$$

Considering that the external forces are equal to zero, the D'Alembert equation is obtained:

$$\frac{\partial^2 z(x, t)}{\partial t^2} = C_0^2 \frac{\partial^2 z(x, t)}{\partial x^2} \quad (3.21)$$

with C_0 being the speed of propagation of a harmonic wave or phase velocity

$$C_0 = C_\phi = \sqrt{\frac{T}{\mu}} \quad (3.22)$$

Making the Fourier transform of *equation (3.21)* in the time and space domains the dispersion equation is obtained

$$\omega^2 \Phi(k, \omega) = C_0^2 k^2 \Phi(k, \omega) \quad (3.23)$$

Then, making explicit the phase velocity on *equation (3.23)*, *equation (3.22)* becomes

$$c_{\phi} = \sqrt{\frac{T}{\mu}} = \frac{\omega}{k} \quad (3.24)$$

Therefore, in the string model, it is possible to say that the phase velocity is constant and independent of the wavelength k . This means that waves with different wavenumbers or wavelengths are going to propagate at the same speed.

Adding the stiffness to the string model a beam model or real string model is obtained

$$\mu \frac{\partial^2 z(x, t)}{\partial t^2} - T \frac{\partial^2 z(x, t)}{\partial x^2} + EI \frac{\partial^4 z(x, t)}{\partial x^4} = f(x, t) \quad (3.25)$$

The dispersion equation or *equation (3.23)* in this case becomes

$$(EI k^4 - \mu \omega^2 + T k^2) \Phi(k, \omega) = 0 \quad (3.26)$$

Then the phase velocity becomes

$$c_{\phi} = \frac{\omega}{k} = \sqrt{\frac{T + EI k^2}{\mu}} \quad (3.27)$$

Hence, the phase velocity is no longer constant and exhibits a dependence on the wavenumber k or on frequency ω . This means that waves with different frequencies and wavenumbers (or wavelengths) are going to propagate at different speeds, being the waves with higher frequencies or wavenumbers the ones with higher speed. As explained in (Gérardin & Rixen, 2015), the wave speed being directly proportional to the wavenumber exhibits that velocity has a maximum for a wavelength equal to zero. This becomes a physical incoherence since high frequency modes are dominated by rotatory motion of cross sections and not inertia is associated with these rotations in the elementary beam theory or Euler-Bernoulli beam model (Meirovitch, 2001).

The beam acts as a dispersing medium and, as explained in *Chapter 1*, wave dispersion is one of the causes of the discrepancy in the results of the geometric model and the real dynamics of the system. To simplify the analysis, a group velocity or velocity of the envelope of waves is defined as

$$c_g = \frac{\partial \omega}{\partial k} = \frac{EI k^2}{\sqrt{\mu} \sqrt{T + EI k^2}} + c_{\phi} \quad (3.28)$$

For the string hypothesis of *equation (3.24)*, this is for non-dispersive mediums, the group velocity coincides with the phase velocity. In models where dispersion is considered, as the Euler-Bernoulli beam model from *equation (3.27)*, group velocity tends to be larger than the phase velocity as explained in (Lee, 2016), see *Figure 3. 1*.

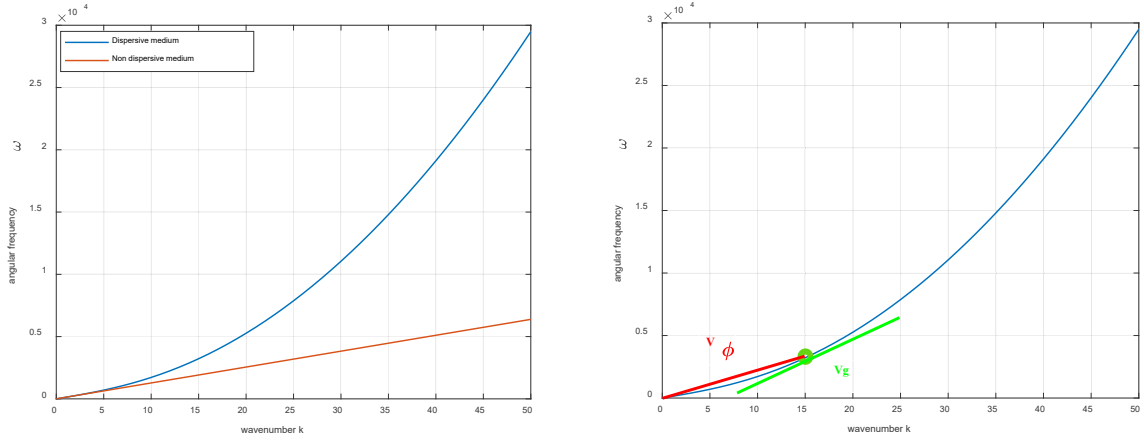


Figure 3. 1 Angular frequency function of the wavenumber for non-dispersive and dispersive mediums (left side). Phase velocity and group velocity on a dispersive medium for $k=15$ (right side).

It is possible to observe that for the first modes, both models are analogue, the main discrepancies between both hypotheses appear on the higher modes.

In the case of a fixed tensioned string defined by an equation of the type

$$v(x, t) = \sum_{m=1}^{\infty} A_m \sin(k_m x + \alpha_m) \sin(\omega_m t + \beta_m) \quad (3.29)$$

The procedure to get the unknowns is the same used for non-dispersive cases. This is, defining boundary and initial conditions. For the case in study, the boundary conditions lead to

$$v(0, t) = 0 \quad \rightarrow \quad k_m = \frac{m\pi}{L} \quad (3.30)$$

$$v(L, t) = 0 \quad \rightarrow \quad \alpha_m = 0$$

The shape of the modes continues to be determined by the boundary conditions, independently of the dispersion, and it is equal to the shape of the modes of non-dispersive mediums.

With the value of k_m , ω_m is calculated from the dispersion equation or *equation (3.26)*. Here is where dispersive and non-dispersive hypothesis diverge. The angular frequency is increased by dispersive effects and relaxation time rises.

The contrast between the string model and the Euler-Bernoulli beam model can be spotted by calculating the relative difference of the phase velocities for each one of them as

$$Relative\ difference\ [\%] = \frac{c_{euler-bernoulli} - c_{string}}{c_{euler-bernoulli}} \cdot 100 \quad (3.31)$$

This difference is obtained for the messenger wire (MW) and for the contact wire (CW). The results are plotted in *Figure 3. 2*.

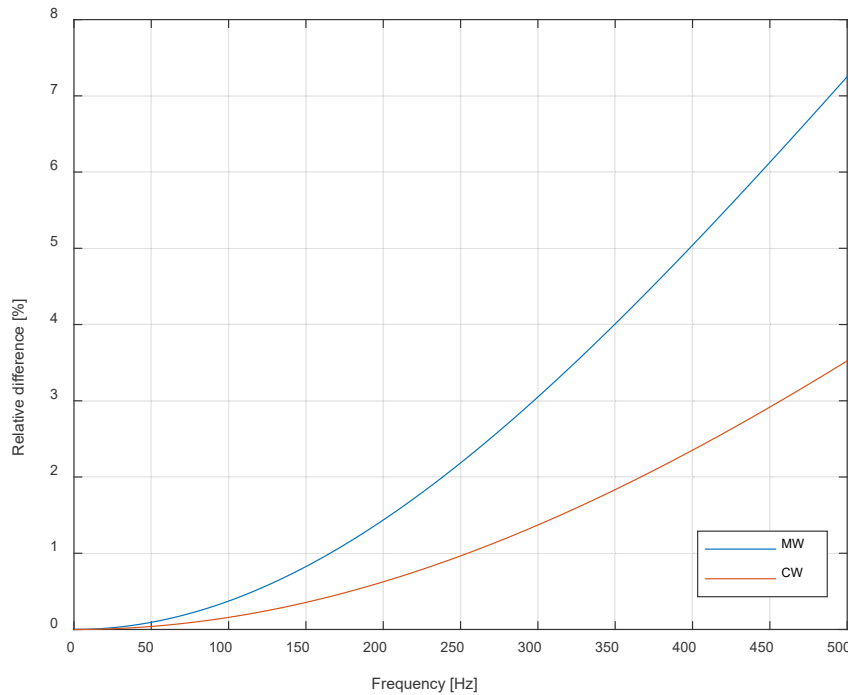


Figure 3. 2 Error in phase velocity when using the string and Euler-Bernoulli models

At low frequencies, both wires behave as strings. It is possible to observe that the mismatch between both models is almost negligible.

As explained in ((CENELEC), 2018) current studies of the pantograph-catenary dynamic interaction are done until 20 Hz for European experimental standards (EN50318) hence, the string model could be sufficient. Nevertheless, wave dispersion is non-negligible and, for high velocity trains, bigger frequency bandwidths of interest are starting to be studied.

3.2 Analytic Model

To observe wave dispersion in beams, the model proposed by (Hyeon Cho, 2008) is used. Considering a simply supported, tensioned Euler Bernoulli beam of the type

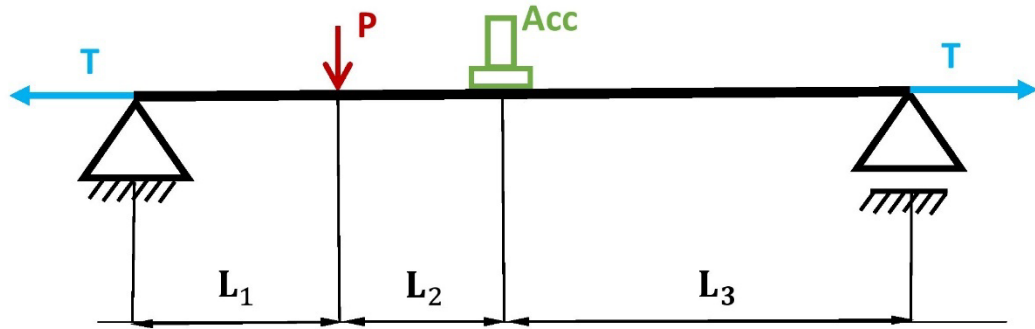


Figure 3. 3 Definition of the model proposed for the study of wave dispersion. Adaptation from (Hyeon Cho, 2008)

where a concentrated excitation force is applied at L_1 and measured at $L_1 + L_2$ with an accelerometer.

An analytical solution for the acceleration measures is proposed in (Dahlberg, 2006), the mode superposition method is written as

$$\ddot{y}(x, t) = \sum_{j=1}^{\infty} A_j \omega_j^2 \sin\left(\frac{j\pi L_1}{L}\right) \sin\left(\frac{j\pi(L_1 + L_2)}{L}\right) \cos(\omega_j t) \quad (3.32)$$

with

$$A_j = \frac{2P}{L} \frac{1}{EI \left(\frac{j\pi}{L}\right)^4 + T \left(\frac{j\pi}{L}\right)^2} \quad (3.33)$$

$$\omega_j = \frac{j\pi}{L} \sqrt{\frac{T}{\mu} + \left(\frac{j\pi}{L}\right)^2 \frac{EI}{\mu}} \quad (3.34)$$

where P is the excitation force, L the total length of the tensioned beam and j is the mode number.

The parameters for the analysis of the proposed model are summarized in *Table 3. 1*.

Parameter	Value	Description
L1	95	Position of the input (Force) [m]
L2	40	Distance from the input to the accelerometer [m]
L3	265	Distance from the accelerometer to the end of the beam [m]
L	400	Total length of the beam [m]
T	22	Axial tension force exerted on the beam [kN]
μ	1.35	Distributed mass per unit of length [kg/m]
E	100	Young modulus [GPa]
Iy	1790×10^{-12}	Moment of area [m ⁴]
P	-180	Excitation force [N]

Table 3. 1 Parameters of the tensioned Euler-Bernoulli beam model

For the first 650 modes of the beam, the results are

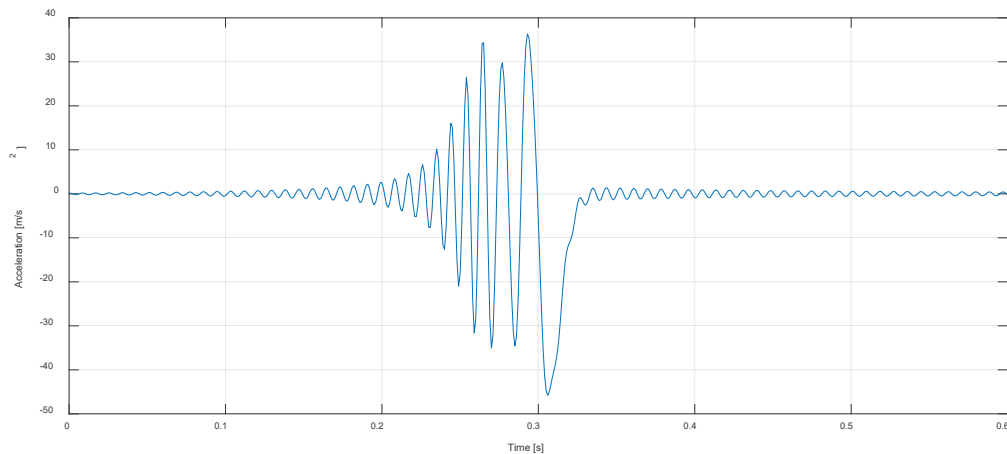


Figure 3. 4 Acceleration obtained from the mode superposition's method

The wave dispersion is clearly represented by *Figure 3. 4*, waves with higher frequency are observed to be faster than the ones with lower frequencies due to the different traveling velocities.

3.3 Finite Element Method Analysis

Following the steps presented in (Genta, 2009) the finite element discretization of the simply supported beam of *Figure 3. 3* was realized. The chosen elements for the discretization were the so-called Euler-Bernoulli beam elements with one node located at each of its ends.

3.3.1 Static FEM Configuration

Mass, damping and stiffness of an element are lumped in both nodes and each node has six degrees of freedom (DOFs), making a total of twelve degrees of freedom for each element

(three displacements and three rotations for each node). For a three-dimensional element, its generalized coordinates vector is equal to:

$$\mathbf{q} = [u_{x1}, u_{y1}, u_{z1}, \phi_{x1}, \phi_{y1}, \phi_{z1}, u_{x2}, u_{y2}, u_{z2}, \phi_{x2}, \phi_{y2}, \phi_{z2}]^T \quad (3.35)$$

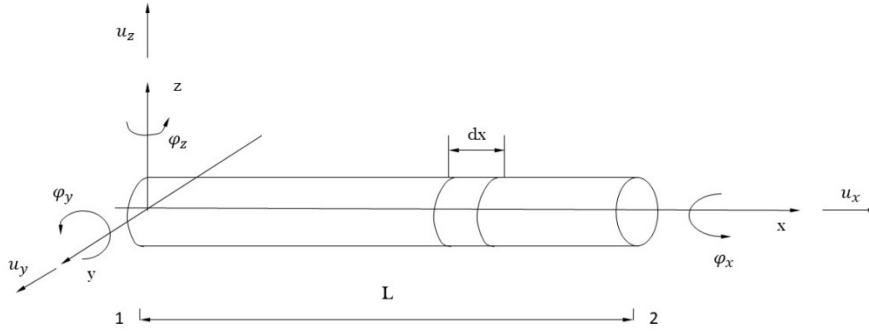


Figure 3. 5 Euler Bernoulli beam element. Adaptation from (Genta, 2009)

Considering that the axis of the beam element is straight along all its length, the axial translation is uncoupled from the other degrees of freedom. If the area centre of all cross sections coincides with their shear centre (if all cross sections have two perpendicular symmetry planes), the torsional degree of freedom is also uncoupled from the rest. Finally, if the planes of symmetry of all cross sections are equally oriented, if the beam is not twisted, and x- and y- axes are perpendicular to such planes, the flexural behaviour on the xz- plane is uncoupled from that in the yz-plane. (Genta, 2009)

Uncoupling the axial, torsional and flexural behaviour allows to subdivide the study of the element. For the tractioned beam of *Figure 3. 3* only the flexural DOF's on plane xz of *Figure 3. 5* and its axial DOF are used, since torsional and flexural effects on plane yz are neglected. The new generalized coordinates vector is equal to:

$$\mathbf{q}_b = [u_{x1}, u_{z1}, \phi_{y1}, u_{x2}, u_{z2}, \phi_{y2}]^T \quad (3.36)$$

For each element of the discretized system, the local mass and stiffness matrices are written as:

$$\mathbf{M}_L = \begin{bmatrix} \mathbf{M}_A & [\mathbf{0}] \\ [\mathbf{0}] & \mathbf{M}_{F_{xz}} \end{bmatrix} \quad (3.37)$$

$$\mathbf{K}_L = \begin{bmatrix} \mathbf{K}_A & [\mathbf{0}] \\ [\mathbf{0}] & \mathbf{K}_{F_{xz}} + \mathbf{K}_g \end{bmatrix} \quad (3.38)$$

The matrix of mass is composed by the mass matrix of the axial DOF (M_A) and the mass matrix of the flexural DOF's ($M_{F_{xz}}$). They both build a matrix of the type

$$\mathbf{M}_L = \begin{bmatrix} \frac{\rho Al}{3} & 0 & 0 & \frac{\rho Al}{6} & 0 & 0 \\ 0 & \frac{13 \rho Al}{35} + \frac{6 \rho I_y}{5l} & \frac{11 \rho Al^2}{210} + \frac{\rho I_y}{10} & 0 & \frac{9 \rho Al}{70} - \frac{6 \rho I_y}{5l} & -\frac{13 \rho Al^2}{420} + \frac{\rho I_y}{10} \\ 0 & \frac{11 \rho Al^2}{210} + \frac{\rho I_y}{10} & \frac{\rho Al^3}{105} + \frac{2 \rho I_y l}{15} & 0 & \frac{13 \rho Al^2}{420} - \frac{\rho I_y}{10} & -\frac{\rho Al^3}{140} - \frac{\rho I_y l}{30} \\ \frac{\rho Al}{6} & 0 & 0 & \frac{\rho Al}{3} & 0 & 0 \\ 0 & \frac{9 \rho Al}{70} - \frac{6 \rho I_y}{5l} & \frac{13 \rho Al^2}{420} - \frac{\rho I_y}{10} & 0 & \frac{13 \rho Al}{35} + \frac{6 \rho I_y}{5l} & -\frac{11 \rho Al^2}{210} - \frac{\rho I_y}{10} \\ 0 & -\frac{13 \rho Al^2}{420} + \frac{\rho I_y}{10} & -\frac{\rho Al^3}{140} - \frac{\rho I_y l}{30} & 0 & -\frac{11 \rho Al^2}{210} - \frac{\rho I_y}{10} & \frac{\rho Al^3}{105} + \frac{2 \rho I_y l}{15} \end{bmatrix}. \quad (3.39)$$

The stiffness matrix has an analogous configuration with a stiffness matrix of the axial DOF (K_A) and a stiffness matrix of the flexural DOF's ($K_{F_{xz}}$). Nevertheless, since traction forces (T_w) produce an increase in the stiffness of the element the so-called geometric stiffness matrix (K_g) needs to be added to account for these stiffening effects. Altogether, they build a matrix of the type

$$\mathbf{K}_L = \begin{bmatrix} \frac{EA}{l} & 0 & 0 & -\frac{EA}{l} & 0 & 0 \\ 0 & \frac{12EI_y}{l^3} + \frac{36T_w}{30l} & \frac{6EI_y}{l^2} + \frac{3T_w}{30} & 0 & -\frac{12EI_y}{l^3} - \frac{36T_w}{30l} & \frac{6EI_y}{l^2} + \frac{3T_w}{30} \\ 0 & \frac{6EI_y}{l^2} + \frac{3T_w}{30} & \frac{4EI_y}{l} + \frac{4T_w}{30} & 0 & -\frac{6EI_y}{l^2} - \frac{3T_w}{30} & \frac{2EI_y}{l} - \frac{4T_w}{30} \\ -\frac{EA}{l} & 0 & 0 & \frac{EA}{l} & 0 & 0 \\ 0 & -\frac{12EI_y}{l^3} - \frac{36T_w}{30l} & -\frac{6EI_y}{l^2} - \frac{3T_w}{30} & 0 & \frac{12EI_y}{l^3} + \frac{36T_w}{30l} & -\frac{6EI_y}{l^2} - \frac{3T_w}{30} \\ 0 & \frac{6EI_y}{l^2} + \frac{3T_w}{30} & \frac{2EI_y}{l} - \frac{4T_w}{30} & 0 & -\frac{6EI_y}{l^2} - \frac{3T_w}{30} & \frac{4EI_y}{l} + \frac{4T_w}{30} \end{bmatrix}. \quad (3.40)$$

Damping can be introduced using a linear combination of the previous two matrices, the proportional damping

$$\mathbf{C}_L = \alpha \mathbf{M}_L + \beta \mathbf{K}_L \quad (3.41)$$

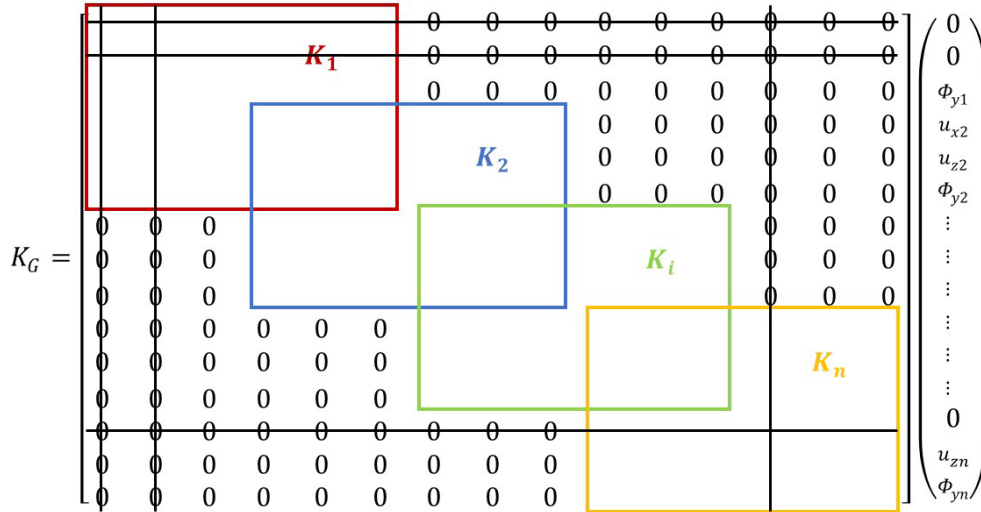


Figure 3. 7 Matrix constraint scheme

with dimensions $3n \times 3n$. The mass and damping matrices are constrained in an analogue way.

The global static force vector is assembled in a similar way with the local static force vectors defined in *equation (3.42)*.

The assembled and constrained global system has the form of

$$\mathbf{M}_G \ddot{\mathbf{q}}_{Gs} + \mathbf{C}_G \dot{\mathbf{q}}_{Gs} + \mathbf{K}_G \mathbf{q}_{Gs} = \mathbf{f}_G \quad (3.43)$$

Finally, the static deflection of the beam is defined as

$$\mathbf{q}_{Gs} = \mathbf{K}_G^{-1} \mathbf{f}_G \quad (3.44)$$

3.3.2 Dynamic FEM Configuration

The equation of motion in the time domain is defined analogously to *equation (3.43)* as

$$\mathbf{M}_G \ddot{\mathbf{q}}_{Gd} + \mathbf{C}_G \dot{\mathbf{q}}_{Gd} + \mathbf{K}_G \mathbf{q}_{Gd} = \mathbf{f}_{Gd} \quad (3.45)$$

The generalized coordinates together with the forcing need to be calculated for each time instant. The result is calculated independently from the static deformations. No variations in time of mass, damping or stiffness matrices are considered.

For the next studies, two types of excitations are considered. A time step forcing term and a sinusoidal forcing term are introduced. The excitation point is defined and the excitation function is defined in that point for a determined amount of time instants as

$$\mathbf{f}_{xp} = [-T \quad p(t) \quad 0 \quad T \quad 0 \quad 0]^T \quad (3.46)$$

where \mathbf{f}_{xp} is the excitation force vector on the input coordinates and $p(t)$ is the excitation force.

3.3.3 Newmark Method

The system is discretized and solved in time by the undamped case of the Newmark's method ($\delta = 0$), studied by (Newmark, 1959) and (Nickel, 1971), a single step implicit integration formula used for second order differential equations with two parameters (β and γ) used to tune the numerical dissipation and properties of the system as defined in (Gérardin & Rixen, 2015).

On its basic form, it consists in two approximation formulas and a balance equation of the type

$$\mathbf{q}_{n+1} = \mathbf{q}_n + \Delta t \dot{\mathbf{q}}_n + \Delta t^2 \left(\frac{1}{2} - \beta \right) \ddot{\mathbf{q}}_n + \Delta t^2 \beta \ddot{\mathbf{q}}_{n+1} \quad (3.47)$$

$$\dot{\mathbf{q}}_{n+1} = \dot{\mathbf{q}}_n + (1 - \gamma) \Delta t \ddot{\mathbf{q}}_n + \gamma \Delta t \ddot{\mathbf{q}}_{n+1}$$

$$[\mathbf{M} + \gamma \Delta t \mathbf{C} + \beta \Delta t^2 \mathbf{K}] \ddot{\mathbf{q}}_{n+1} = \mathbf{f}_{n+1} - \mathbf{C}[\dot{\mathbf{q}}_n + (1 - \gamma) \Delta t \ddot{\mathbf{q}}_n] - \mathbf{K} \left[\mathbf{q}_n + \Delta t \dot{\mathbf{q}}_n + \left(\frac{1}{2} - \beta \right) \Delta t^2 \ddot{\mathbf{q}}_n \right]. \quad (3.48)$$

with the iteration matrix defined as

$$\mathbf{S} = [\mathbf{M} + \gamma \Delta t \mathbf{C} + \beta \Delta t^2 \mathbf{K}] \quad (3.49)$$

The method starts with the definition of matrices \mathbf{M} , \mathbf{C} and \mathbf{K} and the initial conditions for displacement and velocity (\mathbf{q}_0 and $\dot{\mathbf{q}}_0$). Then the initial acceleration can be calculated with the equation

$$\ddot{\mathbf{q}}_0 = \mathbf{M}^{-1}(\mathbf{f}_0 - \mathbf{C} \dot{\mathbf{q}}_0 - \mathbf{K} \mathbf{q}_0) \quad (3.50)$$

After a time-step Δt , it is possible to calculate the predictions for the displacement and velocity as

$$\begin{aligned} \mathbf{q}_{n+1}^* &= \mathbf{q}_n + \Delta t \dot{\mathbf{q}}_n + \Delta t^2 \left(\frac{1}{2} - \beta \right) \ddot{\mathbf{q}}_n \\ \dot{\mathbf{q}}_{n+1}^* &= \dot{\mathbf{q}}_n + (1 - \gamma) \Delta t \ddot{\mathbf{q}}_n \end{aligned} \quad (3.51)$$

With the iteration matrix defined in *equation (3.49)* and the predictions from *equation (3.51)* the acceleration of this new time step Δt can be calculated as

$$\ddot{\mathbf{q}}_{n+1} = \mathbf{S}^{-1}(\mathbf{f}_{n+1} - \mathbf{C} \dot{\mathbf{q}}_{n+1}^* - \mathbf{K} \mathbf{q}_{n+1}^*) \quad (3.52)$$

Finally, the correction for the predictions is applied

$$\begin{aligned} \mathbf{q}_{n+1} &= \mathbf{q}_{n+1}^* + \Delta t^2 \beta \ddot{\mathbf{q}}_{n+1} \\ \dot{\mathbf{q}}_{n+1} &= \dot{\mathbf{q}}_{n+1}^* + \gamma \Delta t \ddot{\mathbf{q}}_{n+1} \end{aligned} \quad (3.53)$$

The whole procedure is summarized in the flow chart of *Figure B. 1*, from *Appendix B*,

The amount of numerical dissipation is controlled by a parameter different than the time steps. Numerical parameters in charge of tuning the numerical dissipation of the system are γ and β ; they are linked with the relationship

$$\beta = \frac{\left(\gamma + \frac{1}{2} \right)^2}{4} \quad (3.54)$$

Hence, the amount of numerical dissipation for a fixed time step is increased by increasing γ . The γ parameter is restricted with a condition of the type

$$\gamma \geq \frac{1}{2} \quad (3.55)$$

since for $\gamma < \frac{1}{2}$ a negative damping is introduced leading to an unbounded or oscillatory response. For $\gamma \geq \frac{1}{2}$, positive damping is introduced and it removes the transient response. Nevertheless, as explained in (Goudreau & Taylor, 1973), this damping is a potential throttle on the spurious oscillations of discrete systems like the one in *equation (3.45)*, in its approximation to discontinuities in the exact continuum solution.

The value of the second parameter is constrained, to produce an unconditionally stable system, by a further condition of the type

$$\beta \geq \frac{1}{4} \quad (3.56)$$

In the case of conditionally stable systems $\beta < \frac{1}{4}$, there is a stability condition for the method, as explained in (Canuto, 2021), that relates the time step with the spatial step of discretization of the beam.

$$\Delta t \leq C h \quad (3.57)$$

where Δt is the time step, h is the spatial step and C is a constant of proportionality.

Choosing $\gamma = \frac{1}{2}$, the beta parameter becomes $\beta = \frac{1}{4}$, calculated from *equation (3.54)*, generating an unconditionally stable system.

The simple supported beam presented in *Figure 3. 3* is discretized with $n = 800$ elements. Then the discretized system is solved for two different time steps $\Delta t = 0.003s$ and $\Delta t = 0.001s$.

The obtained velocity and acceleration for a time step $\Delta t = 0.003s$

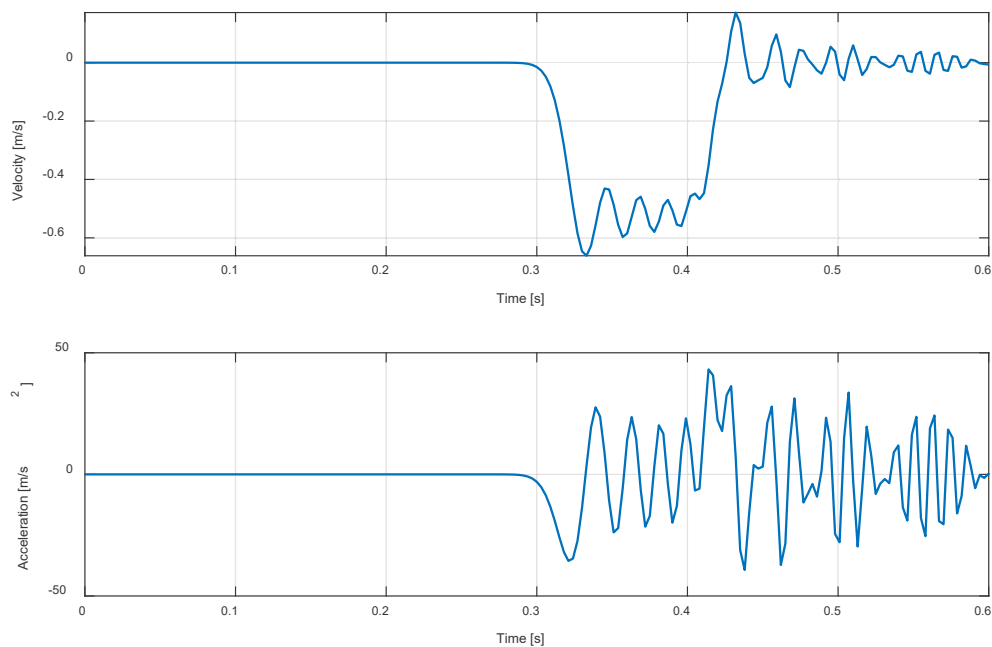


Figure 3. 8 Velocity and Acceleration response obtained from Newmark's integration method with $\Delta t=0.003s$

It is possible to see an opposite behaviour to the one explained in the analytic analysis and the wave dispersion phenomena of *Section 3.1*, lower frequency waves appear to be faster than the ones of higher frequency. In addition, the peaks of acceleration (and velocity) are larger than the ones obtained with the analytic solution and noise is observed in the oscillations.

This behaviour in the solution of Newmark's method is due to the size of the discretization in time, a time step of $\Delta t = 0.003s$ is not able to evidence or detect the dispersive effects.

To achieve better results, considering the same space discretization, a smaller time step is needed. For $\Delta t = 0.001 s$ the results are

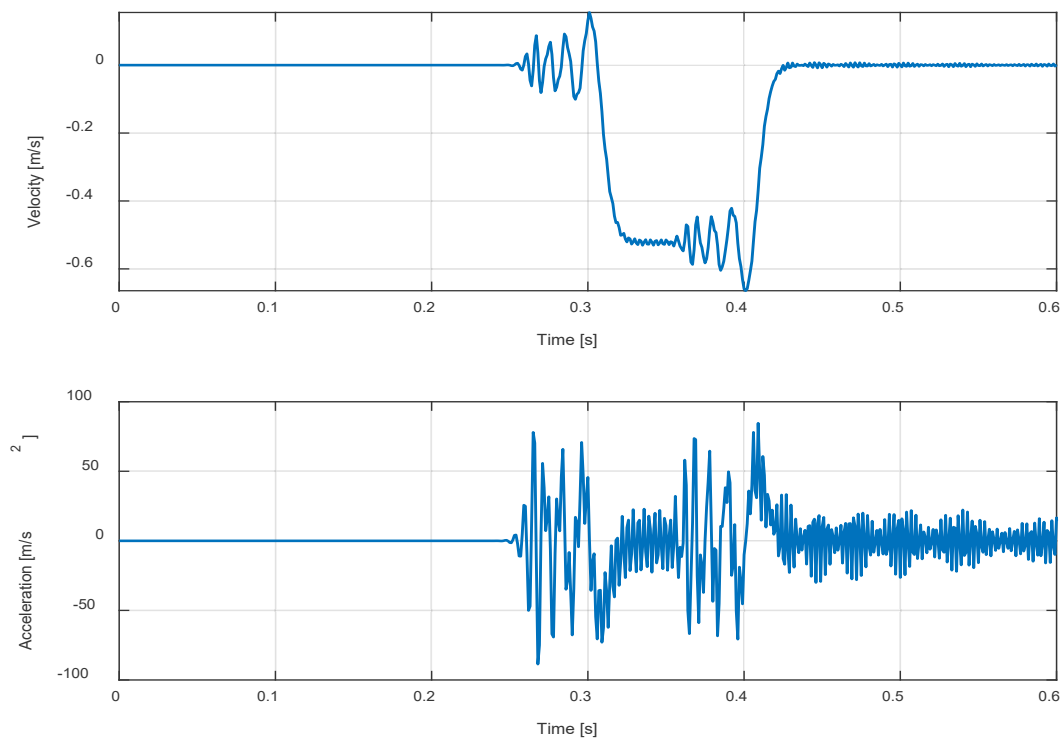


Figure 3. 9 Velocity and Acceleration response obtained from Newmark's integration method with $\Delta t=0.001s$.

In *Figure 3. 9*, the peaks of acceleration continue to be higher than the ones obtained with the analytic solution. Although the dispersive effect seems to be clearer, noise or spurious oscillations are present and a low resolution is spotted in the measurements.

As explained in (Chung & Hulbert, 1993) Newmark's family of methods possess high-frequency dissipation, but these methods are only first order accurate and too dissipative in the low-frequency domain. Higher-frequency dissipation should not produce a loss of accuracy or introduce excessive algorithmic damping in the low frequency modes, a method with a better controllable numerical dissipation is required to damp any spurious oscillations generated by the higher modes.

3.3.4 HHT- α Method

With the understanding of Newmark's method limitations that were previously discussed, three main requirements are defined by (Hilber, Hughes, & Taylor, 1977) for the desired algorithm:

- It should be unconditionally stable when applied to linear problems.
- It should possess numerical dissipation which can be controlled by a parameter other than the time step.
- The numerical dissipation should not affect the lower modes too strongly.

The proposed HHT- α method, or simply α method, is a single step implicit integration formula used for second order differential equations with one parameter (α) used to tune the numerical dissipation and properties of the system as defined in (Hilber, Hughes, & Taylor, 1977).

Analogously to the Newmark method, the α -method on its basic form consists in two approximation formulas and a balance equation of the type

$$\mathbf{q}_{n+1} = \mathbf{q}_n + \Delta t \dot{\mathbf{q}}_n + \frac{\Delta t^2}{2} \left[\frac{1 + 2\alpha - \alpha^2}{2} \ddot{\mathbf{q}}_n + \frac{(1 - \alpha)^2}{2} \ddot{\mathbf{q}}_{n+1} \right] \quad (3.58)$$

$$\dot{\mathbf{q}}_{n+1} = \dot{\mathbf{q}}_n + \Delta t \left[\frac{1 + 2\alpha}{2} \ddot{\mathbf{q}}_n + \frac{1 - 2\alpha}{2} \ddot{\mathbf{q}}_{n+1} \right]$$

$$\left[\mathbf{M} + (1 + \alpha)\mathbf{C} \Delta t \frac{1 - 2\alpha}{2} + (1 + \alpha)\mathbf{K} \frac{\Delta t^2 (1 - \alpha)^2}{2} \right] \ddot{\mathbf{q}}_{n+1} = (1 + \alpha)\mathbf{f}_{n+1} - \alpha\mathbf{f}_n + \alpha\mathbf{C}\dot{\mathbf{q}}_n + \alpha\mathbf{K}\mathbf{q}_n - (1 + \alpha)\mathbf{C}\dot{\mathbf{q}}_{n+1}^* - (1 + \alpha)\mathbf{K}\mathbf{q}_{n+1}^*. \quad (3.59)$$

with the iteration matrix defined as

$$\mathbf{S} = \left[\mathbf{M} + (1 + \alpha)\mathbf{C} \Delta t \frac{1 - 2\alpha}{2} + (1 + \alpha)\mathbf{K} \frac{\Delta t^2 (1 - \alpha)^2}{2} \right] \quad (3.60)$$

The method starts with the definition of matrices \mathbf{M} , \mathbf{C} and \mathbf{K} and the initial conditions for displacement and velocity (\mathbf{q}_0 and $\dot{\mathbf{q}}_0$). Then the initial acceleration can be calculated with the equation

$$\ddot{\mathbf{q}}_0 = \mathbf{M}^{-1}(\mathbf{f}_0 - \mathbf{C} \dot{\mathbf{q}}_0 - \mathbf{K} \mathbf{q}_0) \quad (3.61)$$

After a time-step Δt , it is possible to calculate the predictions for the displacement and velocity as

$$\begin{aligned} \mathbf{q}_{n+1}^* &= \mathbf{q}_n + \Delta t \dot{\mathbf{q}}_n + \frac{\Delta t^2}{2} \left(\frac{1 + 2\alpha - \alpha^2}{2} \right) \ddot{\mathbf{q}}_n \\ \dot{\mathbf{q}}_{n+1}^* &= \dot{\mathbf{q}}_n + \Delta t \left(\frac{1 + 2\alpha}{2} \right) \ddot{\mathbf{q}}_n \end{aligned} \quad (3.62)$$

With the iteration matrix defined in *equation (3.60)* and the predictions from *equation (3.62)* the acceleration of this new time step Δt can be calculated as

$$\ddot{\mathbf{q}}_{n+1} = \mathbf{S}^{-1} \left((1 + \alpha) \mathbf{f}_{n+1} - \alpha \mathbf{f}_n + \alpha \mathbf{C} \dot{\mathbf{q}}_n + \alpha \mathbf{K} \mathbf{q}_n - (1 + \alpha) \mathbf{C} \dot{\mathbf{q}}_{n+1}^* - (1 + \alpha) \mathbf{K} \mathbf{q}_{n+1}^* \right). \quad (3.63)$$

Finally, the correction for the predictions is applied

$$\begin{aligned} \mathbf{q}_{n+1} &= \mathbf{q}_{n+1}^* + \Delta t^2 \beta \ddot{\mathbf{q}}_{n+1} \\ \dot{\mathbf{q}}_{n+1} &= \dot{\mathbf{q}}_{n+1}^* + \gamma \Delta t \ddot{\mathbf{q}}_{n+1} \end{aligned} \quad (3.64)$$

The whole procedure is summarized in the flow chart of *Figure B. 2*, from *Appendix B*.

The stability of the method is defined in terms of spectral stability. To achieve the spectral stability two conditions must be satisfied. First, the spectral radius ρ must be greater or equal than 1

$$\rho = \max\{|\lambda_1|, |\lambda_2|, |\lambda_3|\} \leq 1 \quad (3.65)$$

where λ_1 , λ_2 and λ_3 are the eigenvalues of the amplification matrix of the method, defined in (Hilber, Hughes, & Taylor, 1977). The second condition is that the double roots, or the eigenvalues of multiplicity two, satisfy

$$|\lambda| < 1 \quad (3.66)$$

This condition is explained on (Gear , 1971). If the algorithm is spectrally stable for all frequencies and time steps greater than 0, it is said to be unconditionally stable.

In *Figure 3. 10*, the spectral radii of four different methods are plotted as function of the normalized time steps.

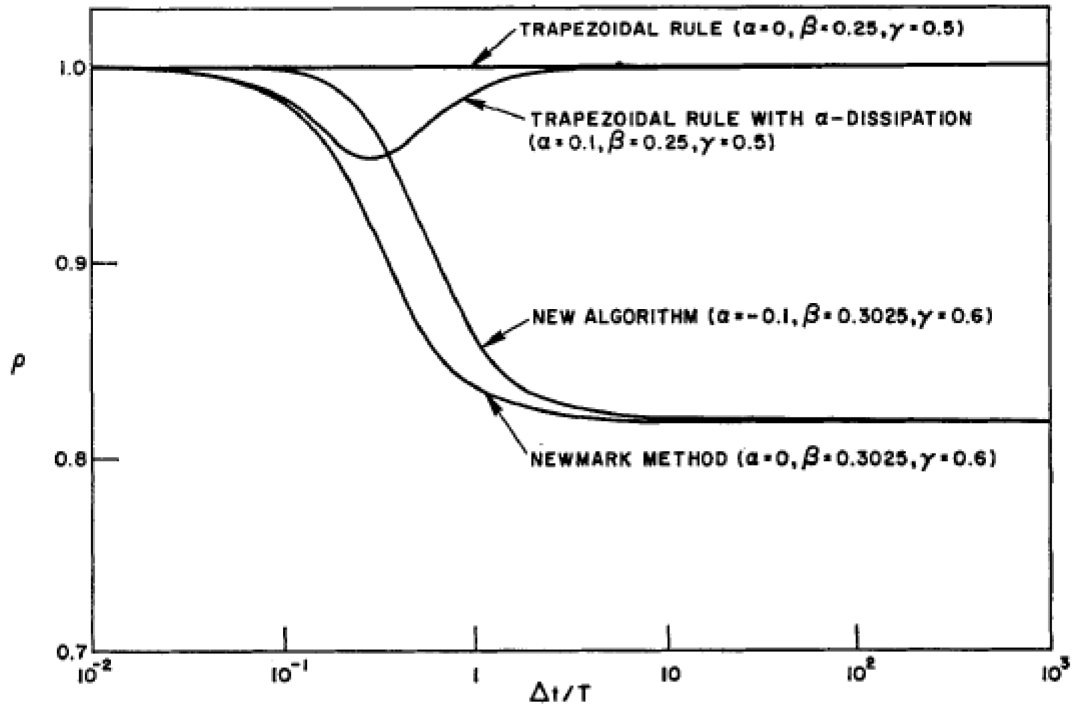


Figure 3. 10 Spectral radii function of the normalized time steps for the HHT- α method and the family of Newmark methods. Figure from (Hilber, Hughes, & Taylor, 1977).

It can be seen that the trapezoidal rule with positive α -dissipation is not an effective dissipative mechanism. In the case of the new algorithm and Newmark's method, they are shown to be identical for large $\Delta t/T$. Nevertheless, for small $\Delta t/T$ the spectral radius in the first case is closer to one than for Newmark's method. This is due to the negative α -dissipation.

In the α -method the amount of dissipation is controlled by the parameter α , independent from the time step. Dissipation exerted by this parameter can be positive or negative.

Positive dissipation is not too effective. It behaves as the linear viscous damping, being inefficient for higher modes, as explained in (Hilber H. , 1976). Nevertheless, it is possible to combine a negative α -dissipation with particular values of β and γ to make a one parameter family of algorithms, the HHT- α method. With

$$\beta = \frac{(1 - \alpha)^2}{4} \quad (3.67)$$

$$\gamma = \frac{1}{2} - \alpha$$

the obtained range of interest for parameter α is

$$-\frac{1}{3} \leq \alpha \leq 0 \quad (3.68)$$

Since for values below $-\frac{1}{3}$ spectral radius increases and the unconditional stability is lost. Furthermore, by reducing the α parameter below $-\frac{1}{3}$, no increase in the damping ratio is obtained as explained in (Hilber, Hughes, & Taylor, 1977).

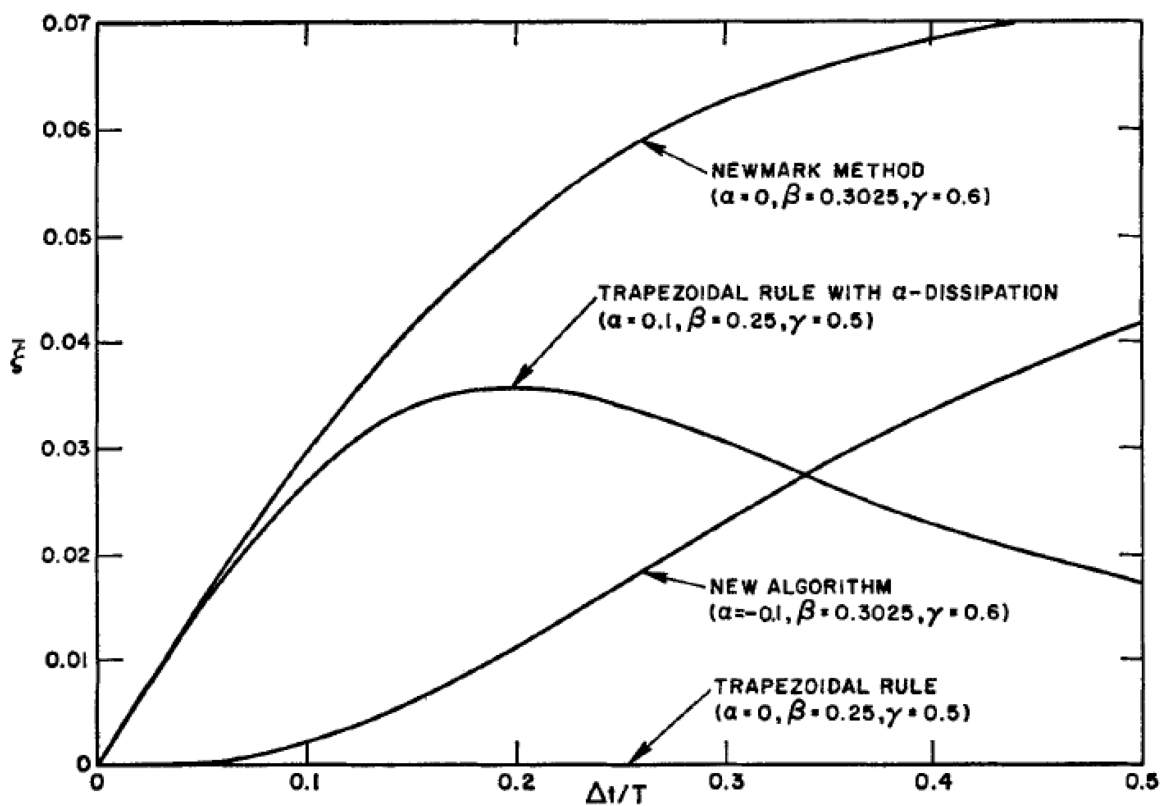


Figure 3.11 Damping ratios vs the normalized time steps for the HHT- α method and the family of Newmark methods. Figure from (Hilber, Hughes, & Taylor, 1977).

For the Newmark method and the trapezoidal rule with positive α -dissipation, the slope of the dissipation ratio curve is positive at the origin. This is the reason why the Newmark family possess ineffective numerical dissipation. For the case of the trapezoidal rule the curve turns downward as $\Delta t/T$ increases, showing the ineffectiveness of the positive α -dissipation. Finally, dissipation of the new introduced algorithm, has a null slope at the origin and slowly increases towards higher $\Delta t/T$.

From the experiments realized by (Hyeon Cho, 2008), for time steps equal to $\Delta t = 0.003s$ or $\Delta t = 0.001s$, convergence is reached with a spatial step $h \leq 0.5m$.

Again, the simple supported beam presented in *Figure 3. 3* is discretized in with $n = 800$ and the discretized system is solved for two different time steps $\Delta t = 0.003s$ and $\Delta t = 0.001s$. The problem is solved with the value $\alpha = -1/3$ in order to accentuate the differences with Newmark's method.

The obtained results are plotted together with the ones obtained from the Newmark method in order to study the main differences. The obtained velocity and acceleration for a time step $\Delta t = 0.003 s$

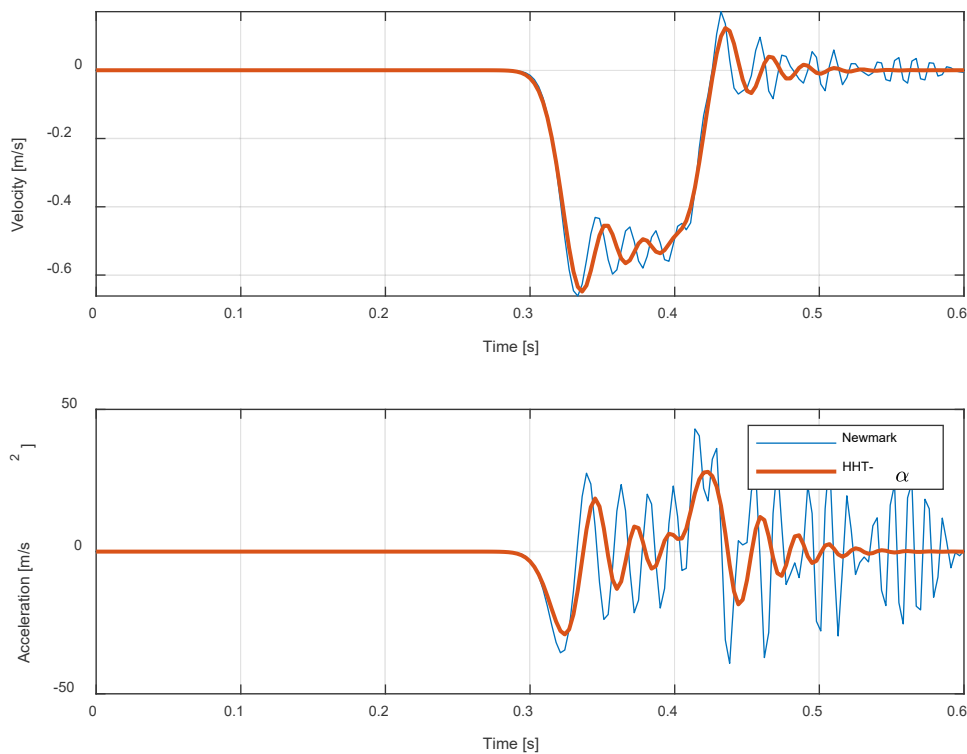


Figure 3. 12 Velocity and Acceleration response obtained from Newmark's and alpha's integration methods with $\Delta t=0.003s$

A clear reduction in spurious oscillations is observed with the use of the α -method, with an increase of the low frequency waves resolution. This improvement in the results is a product of the optimal combination of high frequency and low frequency dissipation of the method. This is that, for a given value of high frequency dissipation, the algorithm minimizes the low frequency dissipation. (Chung & Hulbert, 1993).

However, lower frequency waves appear to be slower than the higher frequency ones, contradicting the results of the analytical model of *Figure 3. 4* and the wave dispersion phenomena explained in *Section 3.1*.

It is possible to conclude that a time step $\Delta t = 0.003s$ is unable to effectively represent the wave dispersion phenomena with both methods, becoming necessary to use smaller time steps.

The results for a reduced time step $\Delta t = 0.001 s$ are

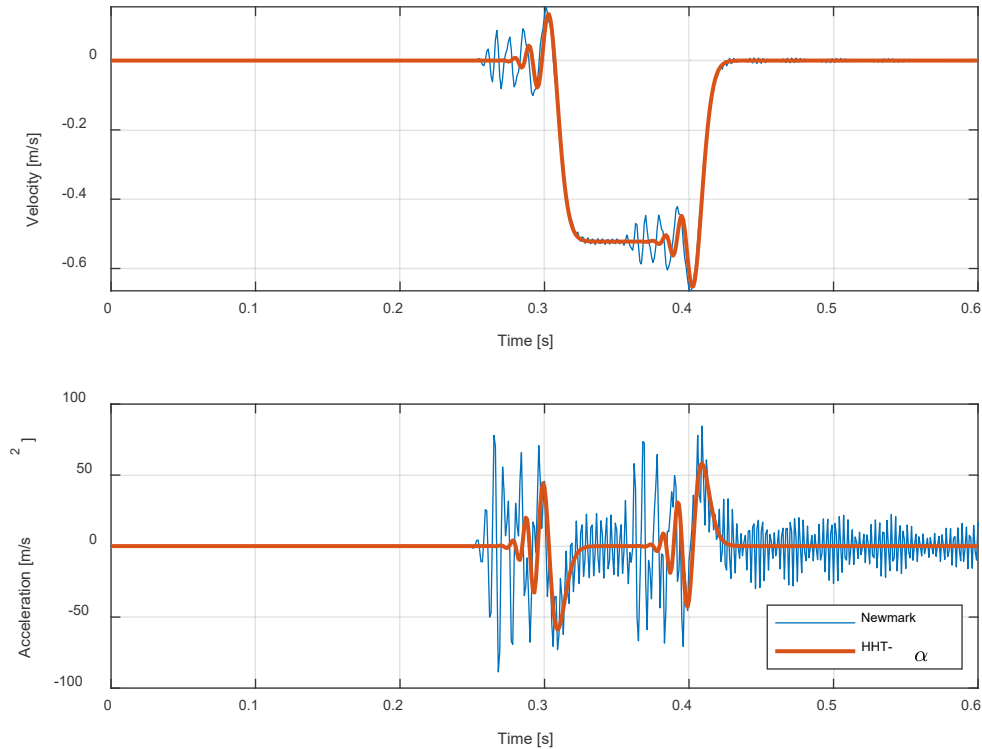


Figure 3. 13 Velocity and Acceleration response obtained from Newmark's and alpha's integration methods with $\Delta t=0.001s$

Spurious oscillations are reduced and the resolution is increased. The wave dispersion phenomena is clearly visible. Therefore, the alpha method has better qualities for the study of the dispersion phenomena.

Despite of being more accurate in the lower modes, it is still strongly dissipative method and for the selected dissipation it attenuates excessively the amplitude of the calculated response.

A further study is done to determine the dissipation level that better suits the requirements of the system. The problem is solved for a $\Delta t=0.001s$, in order to be able to observe the dispersion phenomena, with four different intensities of negative α -dissipation ($\alpha = -\frac{1}{3}, \alpha = -\frac{1}{5}, \alpha = -\frac{1}{10}, \alpha = -\frac{1}{20}$).

The obtained results are plotted for a bounded time interval in *Figure 3. 14*.

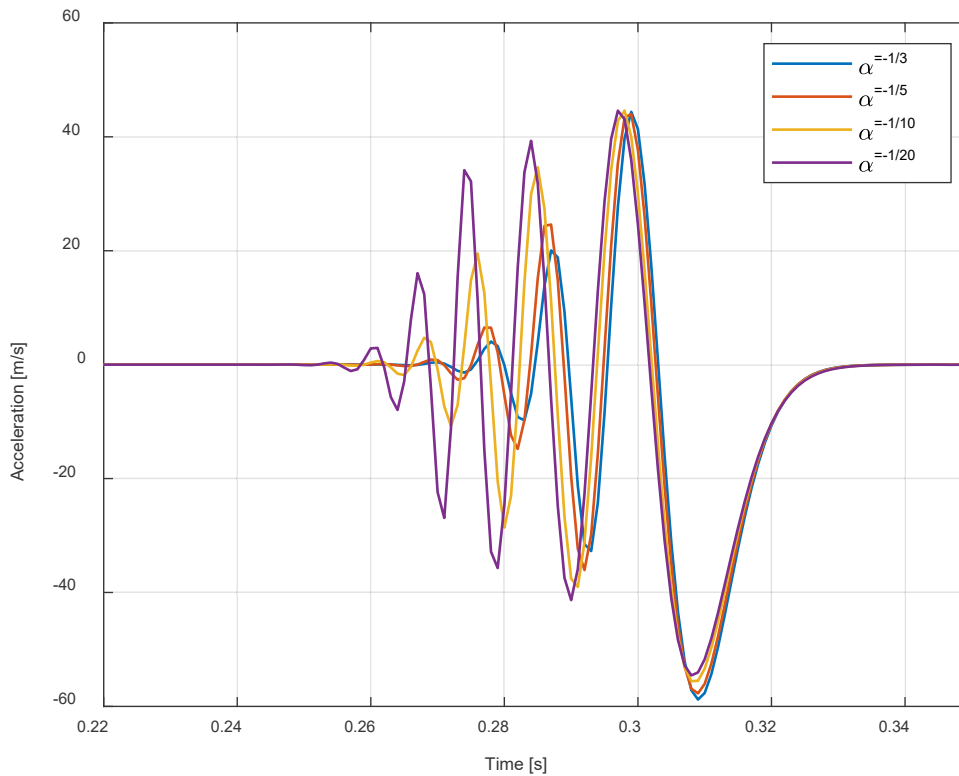


Figure 3. 14 Acceleration response obtained with HHT- α method with a time step $dt=0.001s$ and four negative α -dissipation values.

Comparing the results of *Figure 3. 14* with the analytic results from *Figure 3. 4* it is possible to see that the dissipation obtained for $\alpha = -\frac{1}{10}$ is the most suitable for the case in study since, it increases the amplitude of the oscillations in an acceptable range and it allows to observe more clearly the behaviour of the smaller frequency modes.

3.4 Wave Velocity and Frequency

An analogous form of *equation (3.27)* for tensioned beams, phase velocity function of frequency instead of wavenumber, is proposed by (Park, Jeon, Lee, & Cho, 2006)

$$c_{\phi} = \sqrt{\frac{T + \sqrt{T^2 + 16 \mu EI \pi^2 f^2}}{2\mu}} \quad (3.69)$$

were $T [N]$ is the tension of the wire, μ is the distributed mass per unit of length $[Kg/m]$, EI is the flexural rigidity $[N.m^2]$ and f is the frequency $[Hz]$.

To study the wave velocity dependence on frequency, sinusoidal excitations with three different frequencies (20Hz, 50Hz and 100Hz) are used as an input in the same configuration from *Figure 3. 3*, with the measure point located at a distance of 40m from the excitation's input. The sinusoidal force has an amplitude of 10 [N] and is of the type of

$$f(t) = 10 \sin(2\pi f . t) \tag{3.70}$$

The time history of the system is calculated by two numerical methods (Newmark and α -method.) for two time-steps (dt=0.003s and dt=0.001s).

In order to increase the accuracy in the wave propagation velocity calculations, the input and output signals are filtered using an equi-ripple finite impulse response (FIR) band-pass filter (see *Appendix D*) designed with the Filter Designer form MATLAB's Signal Processing Toolbox (MATLAB, 2021). This filtering isolates the excitation frequency for its analysis and allows a greater precision in the computations.

Subsequently, a short-time Fourier transform was applied to the filtered signals to obtain the time distance between them. To observe the time delay clearly, a spectrogram is plotted function of time at for the excitation frequency. For an excitation frequency of 50 Hz, the filtered signals and the spectrogram for 50 Hz in the time domain are plotted

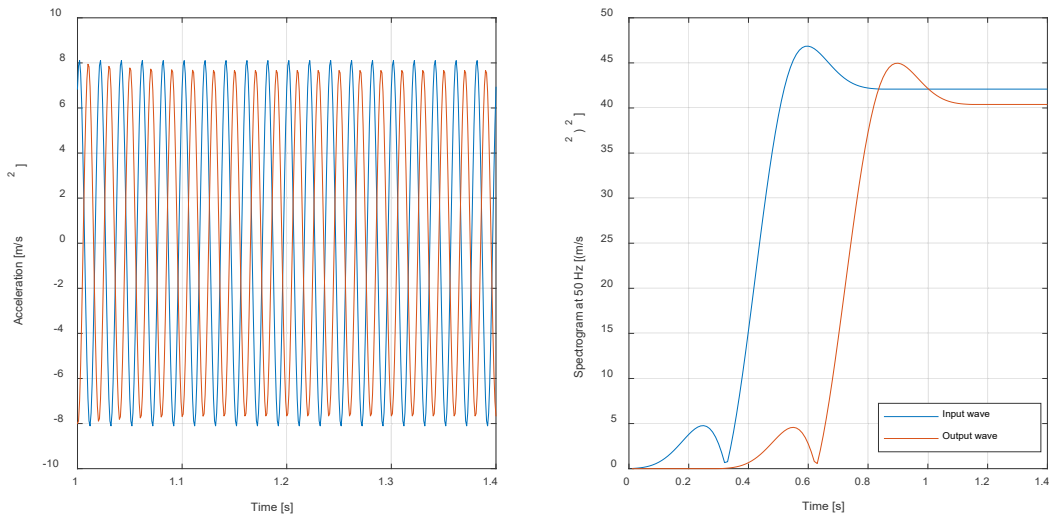


Figure 3. 15 Filtered input and output signals of an input with f=50Hz (left side). Spectrogram at 50 Hz of the input and output waves (right side). Calculations made with alpha method.

Applying the same procedure for the four time-steps, the three frequencies and both numerical methods the results of *Table 3. 2* were obtained. The resulting velocities are compared with the velocities calculated in *equation (69)* and the relative error between them is computed.

Time step [s]	Excitation frequency [Hz]	Theoretical speed [m/s]	α -method		Newmark method	
			Speed [m/s]	Relative error [%]	Speed [m/s]	Relative error [%]
0.003	20	128.15	126.98	0.91	126.98	0.91
	50	130.62	121.21	7.2	121.21	7.2
	100	138	-	-	-	-
0.001	20	128.15	129.03	0.69	129.87	1.34
	50	130.62	133.33	2.07	133.33	2.07
	100	138	137.93	3.51	145.45	5.4

Table 3. 2 Wave propagation speed function of the excitation frequency.

For a time-step $dt=0.003s$, obtained velocities tend to reduce. For frequencies of 20Hz the relative error is almost negligible with both methods while for frequencies of 50Hz, the relative error calculated for the Newmark method is equal to the one obtained with the α -method (7.2 %). Finally, for frequencies of 100Hz the signals are too “weak” to obtain clear velocity results. Nevertheless, the tendency of velocity reduction is clear within the two methods.

Contrarily to the previous reductive effect, by decreasing the time step, velocity tends to increase. With a time-step of $dt=0.001s$ the relative error for frequencies of 20Hz continues to be negligible for both methods. For frequencies of 50 Hz relative errors for both methods are equal (2.07 %) while for frequencies of 100 Hz a clear distinction is made between the two methods with a relative error in the α -method (3.51 %) slightly smaller than the one obtained with the Newmark method (5.4 %).

From the results it is possible to observe the same effects described in *Section 3.3*, with time steps of $dt=0.003s$ the dispersive effects are not taken into account. This means that higher frequencies are considered to be slower than smaller frequencies. With time steps of $dt=0.001s$ or smaller, dispersive effects are considered, with higher frequencies been faster than waves with smaller frequencies.

The whole procedure is summarized on the *Appendix C*.

Chapter 4

Mechanical Wave Effects – Transmission and Reflection

The span of the catenary system may be considered to be constructed in segments as seen in *Figure 4. 3*, each one of them delimited by two droppers at both ends. Droppers are fixed to the two wires (Messenger wire and Contact wire) by joints or claws.

When the traveling wave arrives to one of these joints it is decomposed into a transmitted wave and a reflected wave, generating at the same time two transmitted waves in the other wire. To explain more in detail the functionality of the phenomena, two different models from (Vo Van, 2016) are proposed and analysed.

4.1 Wave Reflection and Transmission on a Lumped Mass

An incident wave $z_i(x,t)$, travels through tensioned wire with a velocity c calculated with the string theory (*equation (3.22)*). It arrives to a lumped mass and it is decomposed in two different waves, a transmitted wave $z_t(x,t)$ and a reflected wave $z_r(x,t)$ as seen in *Figure 4. 1*.

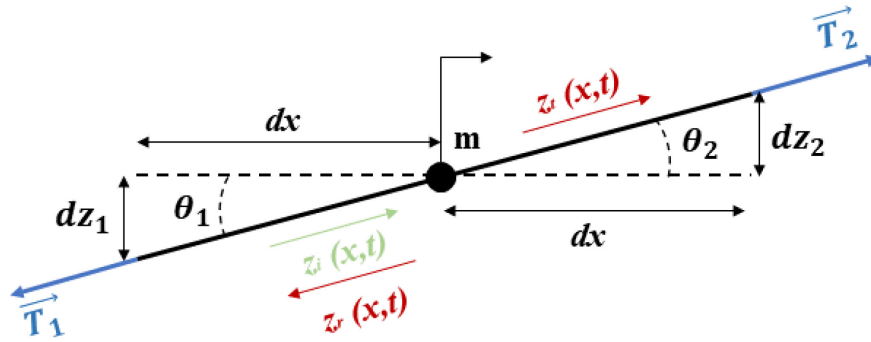


Figure 4. 1 Lumped mass on a single wire of length $2dx$. Adaptation from (Vo Van, 2016)

The three waves can be calculated as

$$z_i(x, t) = \int_{-\infty}^{\infty} \int_{-\infty}^{\infty} \Phi_i(k, \omega) e^{i\omega(t - \frac{x}{c})} dk d\omega \quad (4.71)$$

$$z_r(x, t) = \int_{-\infty}^{\infty} \int_{-\infty}^{\infty} \Phi_r(k, \omega) e^{i\omega(t + \frac{x}{c})} dk d\omega \quad (4.72)$$

$$z_t(x, t) = \int_{-\infty}^{\infty} \int_{-\infty}^{\infty} \Phi_t(k, \omega) e^{i\omega(t - \frac{x}{c})} dk d\omega \quad (4.73)$$

where $\Phi_i(k, \omega)$, $\Phi_r(k, \omega)$ and $\Phi_t(k, \omega)$ are the double Fourier transform in space and time of the vertical incident, reflected and transmitted waves respectively.

Newton's second law can be applied on the lumped mass, yielding

$$-T \left. \frac{\partial z_i}{\partial x} \right|_{x=0^-} - T \left. \frac{\partial z_r}{\partial x} \right|_{x=0^-} + T \left. \frac{\partial z_t}{\partial x} \right|_{x=0^+} = m \frac{\partial^2 z_m}{\partial t^2} \quad (4.74)$$

where T is the tension of the cable that, multiplied by the first derivative of the wave displacement respect to the space, gives the shear force.

By using equations (3.69) to (4.73) it is possible express equation (4.74) in the frequency domain as

$$\frac{T}{c}(\Phi_i(k, \omega) - \Phi_r(k, \omega) - \Phi_t(k, \omega)) = i\omega m \Phi_t(k, \omega) \quad (4.75)$$

constituting the first equation of the system. By making the continuity of displacement at the origin of x positioned on the lumped mass, the second equation of the system is obtained

$$\Phi_i(k, \omega) + \Phi_r(k, \omega) = \Phi_t(k, \omega) \quad (4.76)$$

Using the model of the string from *equation (3.22)*, $\frac{T}{c}$ is replaced by $\sqrt{\mu T}$, the system of equations constituted by *equation (4.75)* and *equation (4.76)* becomes

$$\begin{bmatrix} 1 & 1 + \frac{i\omega m}{\sqrt{\mu T}} \\ -1 & 1 \end{bmatrix} \begin{Bmatrix} \Phi_r \\ \Phi_t \end{Bmatrix} = \begin{bmatrix} 1 \\ 1 \end{bmatrix} \{\Phi_i\} \quad (4.77)$$

Finally, with *equation (4.76)* it is possible to write the analytical expression of reflection and transmission coefficients

$$\begin{Bmatrix} \Phi_r \\ \Phi_t \end{Bmatrix} = \begin{bmatrix} -i\omega m \\ \sqrt{\mu T} + i\omega m \\ \sqrt{\mu T} \\ \sqrt{\mu T} + i\omega m \end{bmatrix} \{\Phi_i\} = \begin{bmatrix} R_{mass}(\omega) \\ T_{mass}(\omega) \end{bmatrix} \{\Phi_i\} \quad (4.78)$$

Two cases are used to modellate the mass of Figure 4. 1: $m_{0.2}$ corresponding to the standard 195g mass of a claw linking the dropper and the contact wire and m_1 for an approximate 1kg mass of a junction claw used to reinforce a damaged contact wire.

The parameters used to construct the analytical model are listed on *Figure 4. 1*.

Parameter	Value	Description
T	22	Axial tension force on the wire [kN]
M	1.35	Distributed mass per unit of length [kg/m]
E	100	Young modulus [GPa]
P	8940	Density of copper [kg/m ³]
I _y	2082,43 x 10 ⁻¹²	Moment of area [m ⁴]
A	150 x 10 ⁻⁶	Section of the wire [m ²]
m ₀₂	0.195	Mass of a standard claw linking the dropper and the wire [kg]
m ₁	1	Mass of a junction claw used to reinforce damaged wires [kg]

Table 4. 1 Parameters of the lumped mass model

The obtained results are

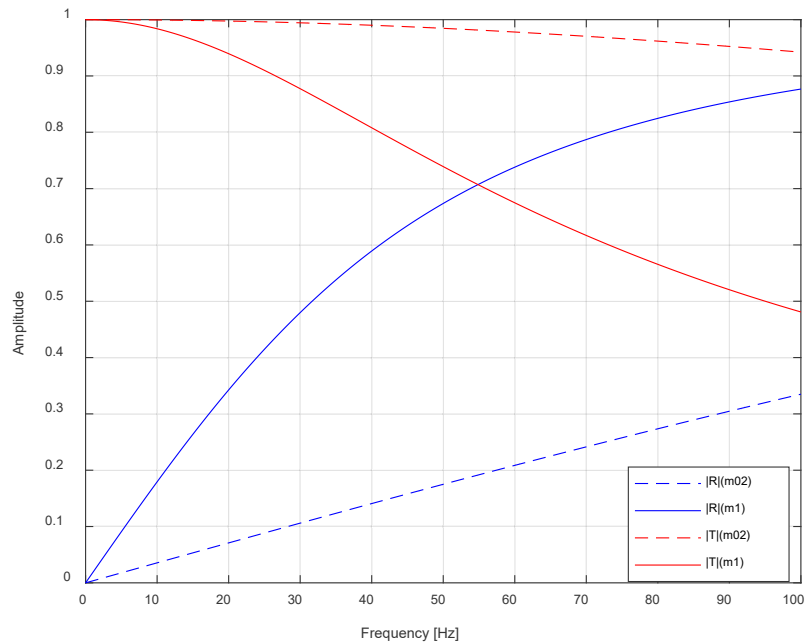


Figure 4. 2 Coefficients of reflection (blue) and transmission (red) for lumped masses of 195gr (dashed) and 1kg (solid)

In the figure it is possible to observe two main behaviours. As mass increases, the dependance of the transmission and reflection coefficients on frequency tends to be higher while for lower masses variations in frequency are considerably smaller. At lower frequencies, less than 30 Hz, the predominance of the transmission coefficient over the reflection one is evident; as frequencies start to increase this predominance is reduced until reflection coefficient takes the lead after 50 Hz.

4.2 Wave Reflection and Transmission on a Dropper

A more realistic model consists of a dropper connecting the messenger and contact wires at its ends. The dropper is represented with two lumped masses at its ends, one spring and one damper.

The input of the system is a step velocity wave of 0.6 m/s. Simulations were carried out in two different configurations by placing the input wave at the same distance from the measuring point but with two different configurations of the catenary, as shown in the *Figure 4. 3*.

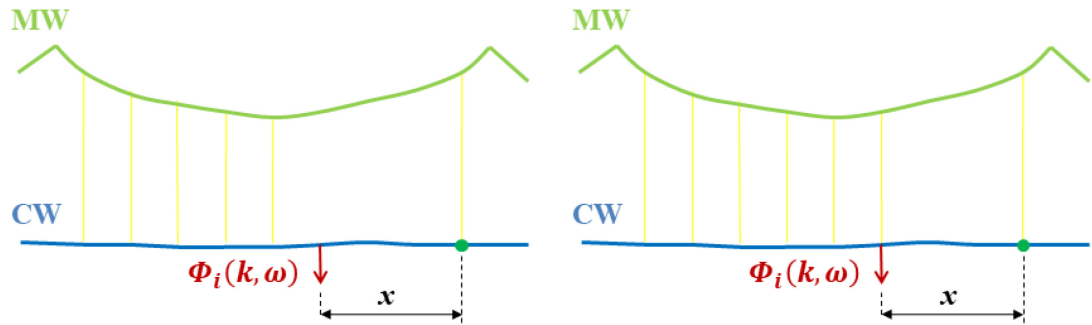


Figure 4. 3 System configurations with an input at the same distance ($x=10m$) from the measuring point (green point): Singular incident wave on the CW (left side). Two incident waves, one on the MW and one on the CW generated by positioning the input on a dropper (right side).

4.2.1 Input Wave on One of the Two Cables

The input wave, $\Phi_i(k, \omega)$, arrives to the dropper position from the contact wire generating four different waves, one transmitted and one reflected on the contact wire, $\Phi_{t+,CW}(k, \omega)$ and $\Phi_r(k, \omega)$, and two transmitted in the messenger wire, $\Phi_{t-,MW}(k, \omega)$ and $\Phi_{t+,MW}(k, \omega)$

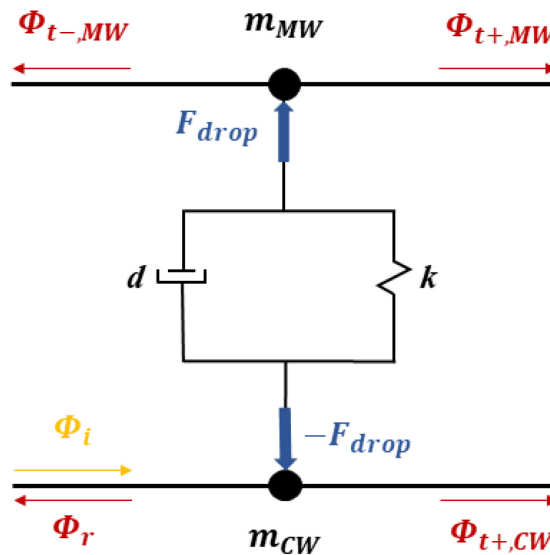


Figure 4. 4 Dropper connecting the two wires model, input wave on a single wire. Adaptation from (Vo Van, 2016)

To get the constitutive equations of the system a similar procedure to the one used in *Section 4.1* is applied on the frequency domain.

Following the procedures done with *equation (4.74)*, the first two equations are obtained using Newton's second law for the two masses

$$\frac{T_{CW}}{C_{CW}} [\Phi_i(k, \omega) - \Phi_r(k, \omega) - \Phi_{t+,CW}(k, \omega)] - F_{drop} = i\omega m_{CW} \Phi_{t+,CW}(k, \omega) \quad (4.79)$$

$$\frac{T_{MW}}{C_{MW}} [-\Phi_{t-,MW}(k, \omega) - \Phi_{t+,MW}(k, \omega)] + F_{drop} = i\omega m_{MW} \Phi_{t+,MW}(k, \omega) \quad (4.80)$$

With the continuity of displacement on both masses, two more equations are obtained

$$\Phi_i(k, \omega) - \Phi_r(k, \omega) = \Phi_{t+,CW}(k, \omega) \quad (4.81)$$

$$\Phi_{t-,MW}(k, \omega) = \Phi_{t+,MW}(k, \omega) \quad (4.82)$$

Finally, the impedance definition of the dropper gives the fifth equation

$$F_{drop} = [\Phi_{t+,CW} - \Phi_{t-,MW}] \left(D + \frac{K}{i\omega} \right) \quad (4.83)$$

Writing the system in a matrix form

$$\begin{bmatrix} \frac{T_{CW}}{c_{CW}} & \frac{T_{CW}}{c_{CW}} + i\omega m_{CW} & 0 & 0 & 1 \\ 0 & 0 & \frac{T_{MW}}{c_{MW}} & \frac{T_{MW}}{c_{MW}} + i\omega m_{MW} & -1 \\ -1 & 1 & 0 & 0 & 0 \\ 0 & 0 & -1 & 1 & 0 \\ 0 & D + \frac{K}{i\omega} & 0 & -D - \frac{K}{i\omega} & 1 \end{bmatrix} \begin{Bmatrix} \Phi_r \\ \Phi_{t+,CW} \\ \Phi_{t-,MW} \\ \Phi_{t+,MW} \\ F_{drop} \end{Bmatrix} = \begin{bmatrix} \frac{T_{CW}}{c_{CW}} \\ 0 \\ 1 \\ 0 \\ 0 \end{bmatrix} \{\Phi_i\}. \quad (4.84)$$

Finally, with *equation (4.84)* it is possible to write the analytical expression of reflection and transmission coefficients and of the dynamic impedance of the dropper

$$\begin{Bmatrix} \Phi_r \\ \Phi_{t+,CW} \\ \Phi_{t-,MW} \\ \Phi_{t+,MW} \\ F_{drop} \end{Bmatrix} = \begin{bmatrix} R_{drop,CW} \\ T_{drop,CWtoCW} \\ T_{drop,CWtoMW} \\ T_{drop,CWtoMW} \\ Z_{drop} \end{bmatrix} \{\Phi_i\} \quad (4.85)$$

where the transfer functions $R_{drop,CW}$, $T_{drop,CWtoCW}$ and $T_{drop,MWtoCW}$ are the coefficient of reflection of the wave in the CW, the coefficient of transmission of the wave in the CW and the coefficient of transmission from CW to the MW through the dropper.

The coefficients at 0 Hz are calculated for a single wave on the CW and for a single wave on the MW as

$$T_{drop,CWtoCW}(\omega = 0) = T_{drop,CWtoMW}(0) = -R_{drop,MW}(0) = \frac{\frac{T_{CW}}{c_{CW}}}{\frac{T_{CW}}{c_{CW}} + \frac{T_{MW}}{c_{MW}}} \quad (4.86)$$

$$T_{drop,MWtoMW}(\omega = 0) = T_{drop,MWtoCW}(0) = -R_{drop,CW}(0) = \frac{\frac{T_{MW}}{c_{MW}}}{\frac{T_{CW}}{c_{CW}} + \frac{T_{MW}}{c_{MW}}} \quad (4.87)$$

The resulting coefficients for the tensions $T_{CW} = 22kN$ and $T_{MW} = 16kN$ leading to the velocities $c_{CW} = 127.66 \text{ m/s}$ and $c_{MW} = 121.71 \text{ m/s}$ are

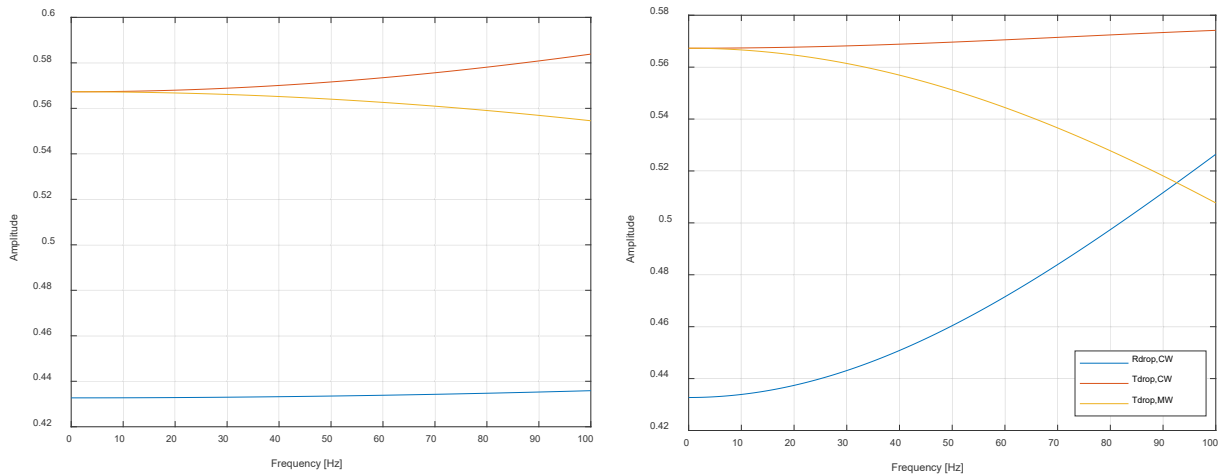


Figure 4. 5 Coefficients of reflection (blue), transmission on the CW (red) and transmission on the MW (yellow). Incident wave on the CW for a standard dropper mass of 195gr (left side) and for a reinforced dropper 1kg (right side).

As in the previous case it is possible to observe a predominance of transmission coefficients over the reflective coefficients for low frequencies and an increasing influence of the latter for higher frequencies. This behaviour is clearer as the mass increases, or for cases of reinforcements in broken or fragile droppers while the usual mass of the droppers generates a more attenuated increase of reflective effects. For the next experiments the case of reinforced droppers will be analysed, this is lumped masses of 1kg.

Therefore, by seeing *equation (4.86)* and *equation (4.87)*, mechanical tension exerted in the wires can be spotted as the only parameter capable of modifying the coefficients at low frequencies. Its importance will be analysed together with other parameters variations such as the dropper mass in the CW and MW (m_{CW} and m_{MW}), the dropper stiffness (K_{drop}) and the dropper damping coefficient (D_{drop}).

The obtained results are depicted in *Figure 4. 6*.

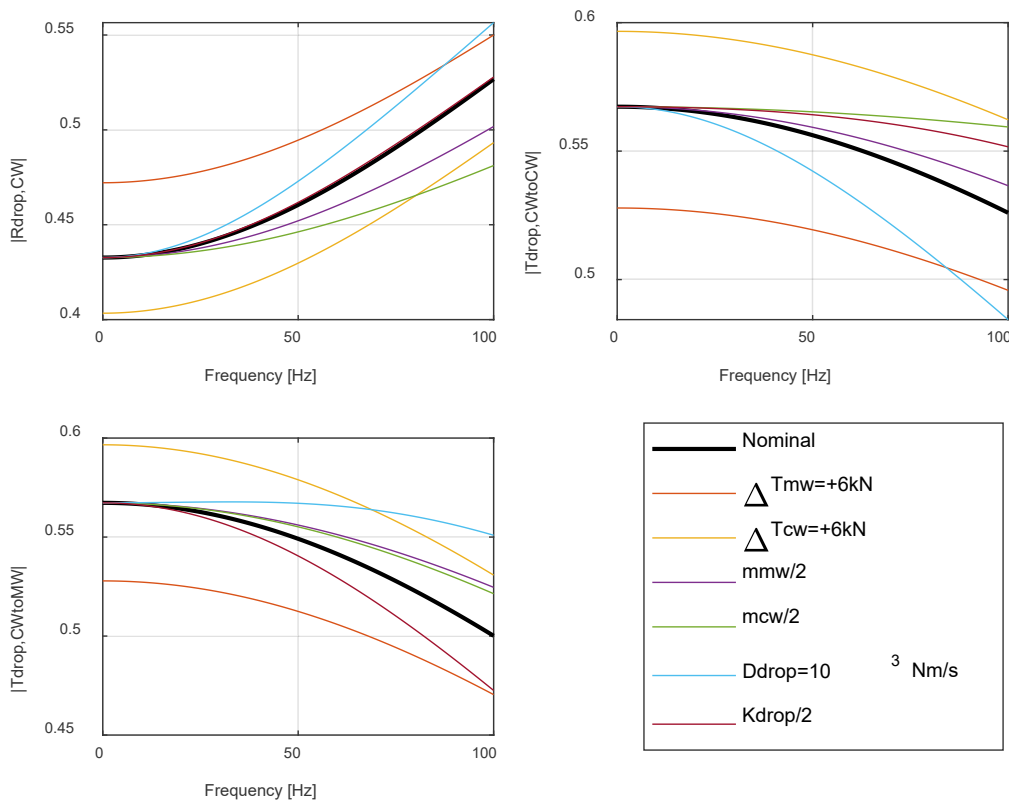


Figure 4. 6 Variation of the CW transfer functions with the modification of different parameters for a reinforced dropper (nominal) mass (1kg).

Variations in the stiffness, damping and inertia of the droppers produce variations in the rigidity of the coefficient’s behaviour in frequency, while higher variations are generated by the mechanical tensions as previously explained. Particularly the decrease in the inertia generates an attenuation of the reflection coefficients while it favours the transmission, being

the mass in the CW the most predominant in this case. Increasing the damping of the dropper have an inverse effect with reflection (increasing it). Nevertheless, with the transmission, its effect is different for transmissions on the same wire (it decreases them) and transmissions from one wire to the other (it increases them). Finally, stiffness of the dropper does not induce important changes in reflection however, it increases both transmission coefficients.

Solving *equation (4.85)* with the nominal parameters of *Figure 4. 5*, the resulting velocity waves are obtained for the case of *Figure 4. 3* (left side).

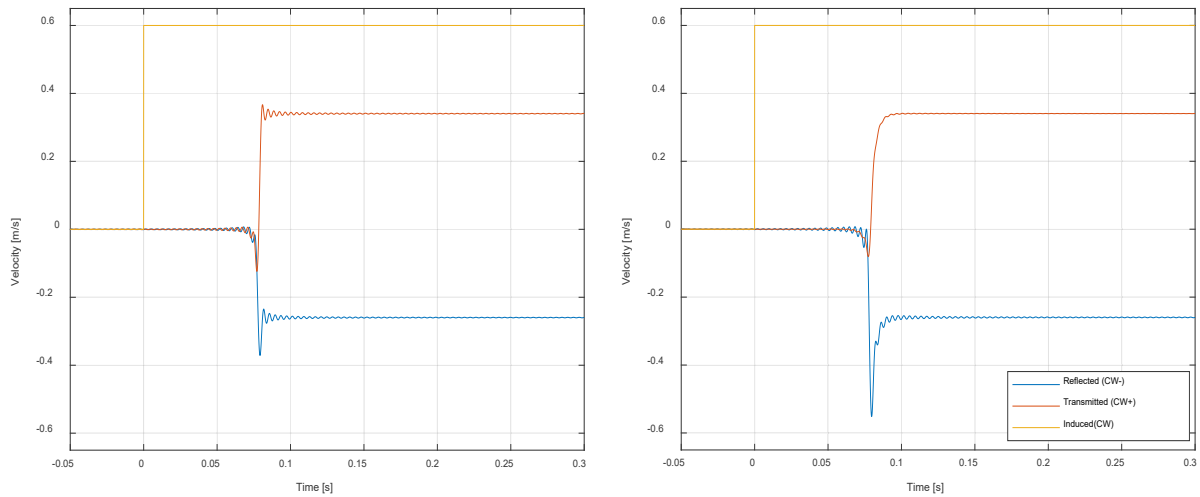


Figure 4. 7 Wave velocities in the CW for a standard dropper mass of 195gr (left side) and for a reinforced dropper 1kg (right side)

The delay in the response is due to the time that the velocity wave takes to travel the distance x from the application point to the measuring point (*Figure 4. 3*). In the contact wire (CW), the wave is more likely to be transmitted than reflected, this is observable from *Figure 4. 6* and *Figure 4. 7*. Although reflection is increased for the reinforced dropper, a clear predominance of the transmission is observed for both cases.

To analyse the situation with the transmitted waves in the messenger wire (MW), an analogous experiment can be done considering that the input wave is in the MW. By following the same procedure done for the input wave in the CW the resulting equation of the transfer functions is

$$\begin{Bmatrix} \Phi_r \\ \Phi_{t+,MW} \\ \Phi_{t-,CW} \\ \Phi_{t+,CW} \\ F_{drop} \end{Bmatrix} = \begin{bmatrix} R_{drop,MW} \\ T_{drop,MWtoMW} \\ T_{drop,MWtoCW} \\ T_{drop,MWtoCW} \\ Z_{drop} \end{bmatrix} \{\Phi_i\} \quad (4.88)$$

From *equation (4.86)* and *equation (4.87)*, the predominant importance of mechanical tensions is again evident. Again, the coefficients are calculated for parameters variations such as the dropper mass in the CW and MW (m_{CW} and m_{MW}), the dropper stiffness (K_{drop}) and the dropper damping coefficient (D_{drop}).

The obtained results are depicted in *Figure 4. 8*.

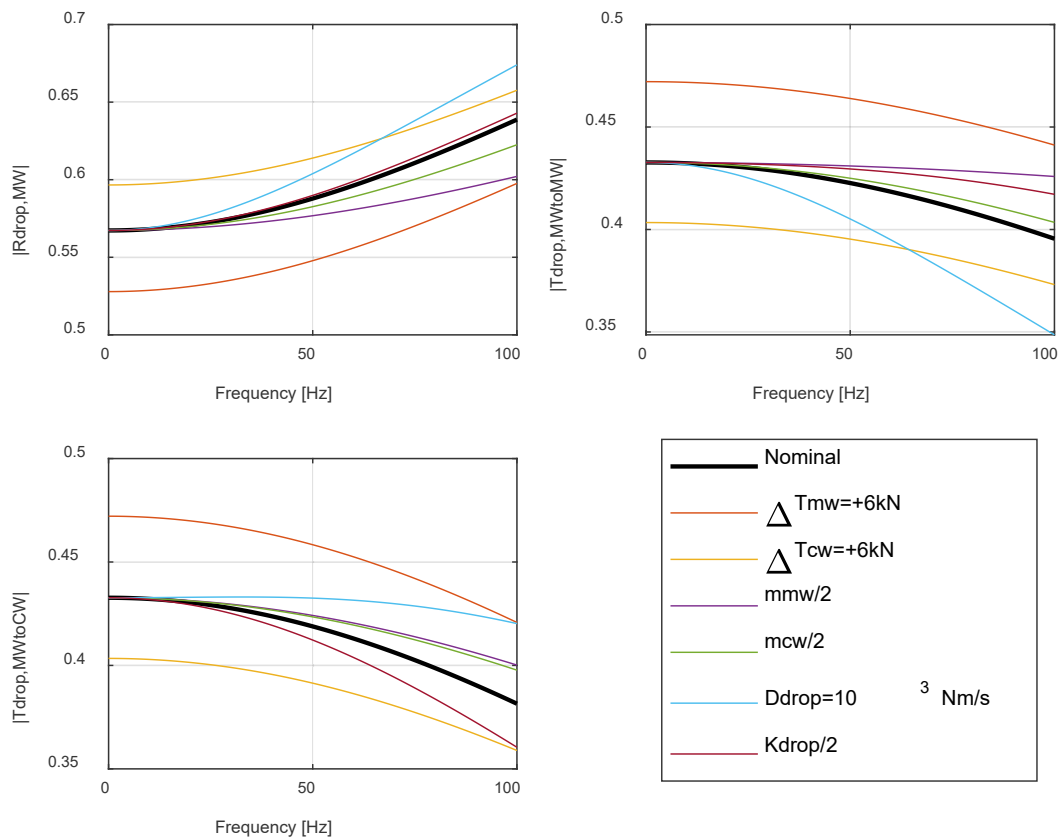


Figure 4. 8 Variation of the MW transfer functions with the modification of different parameters for a reinforced dropper (nominal) mass (1kg).

The results are analogous to the ones in *Figure 4. 6*, nevertheless a clear predominance of reflection coefficients is observed over the transmission coefficients. Tensions exerted to the cables are the only parameters capable of modifying the transmission coefficients for low frequency values. Masses have the same effect as in the CW, reducing the reflection coefficient while increasing the transmission ones when it decreases its value, being the mass in the MW the most predominant in this case. Bigger damping coefficients generate an increase in the reflection coefficient and in the transmission effects from one wire to the other while producing a decrease in the transmission coefficient on the same wire. Finally, decreasing the rigidity increases the transmission effects on the same cable while it reduces the transmission from one wire to the other.

Solving *equation (4.88)* the resulting velocity waves are obtained for the case of *Figure 4. 3* (left side) where the input wave is located on the MW

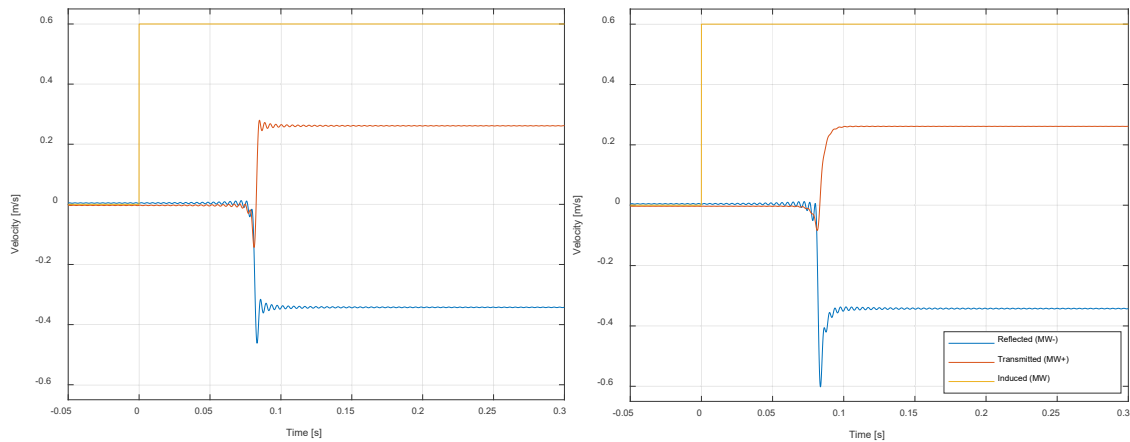


Figure 4. 9 Wave velocities in the MW for a standard dropper mass of 195gr (left side) and for a reinforced dropper 1kg (right side)

The delay in the response is observed to be slightly higher than the one in *Figure 4. 7*, this is because of $c_{CW} > c_{MW}$. From *Figure 4. 8* and *Figure 4. 9* it is possible to spot higher reflection coefficients over the transmission coefficient. Hence, the transmitted waves in the MW coming from the input in the CW (case of *Figure 4. 3* (left side)) are going to be more reflected than transmitted, finishing trapped between two droppers. Reflection is more evident for the reinforced droppers, nevertheless, its predominance over the transmission coefficients is also evident on the case of “normal” droppers.

4.2.2 Input wave on a Dropper – Waves Generated in the Two Cables

The input waves, $\Phi_{i,CW}(k, \omega)$ and $\Phi_{i,MW}(k, \omega)$, arrive to the dropper position from the contact wire and the messenger wire, generating four different waves each as seen in *Figure 4. 10*. The case is the one schematized in *Figure 4. 3* (right side).

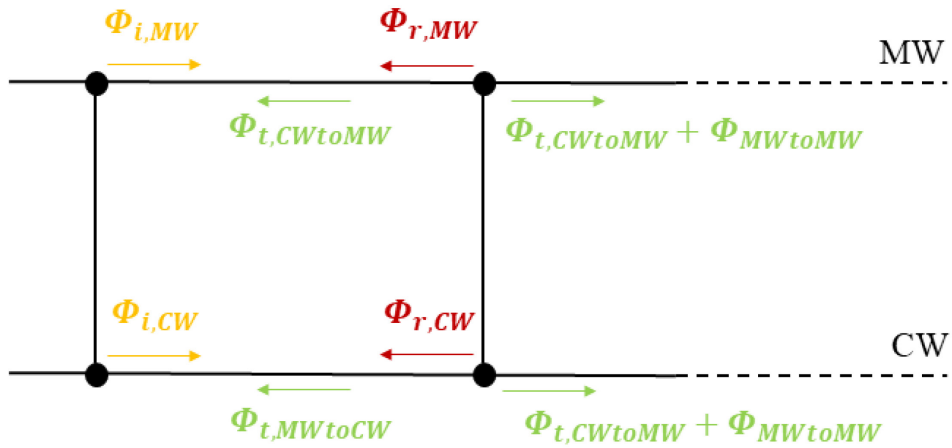


Figure 4. 10 Droppers connecting the two wires model, input wave on both wires. Adaptation from (Vo Van, 2016)

To solve this model, a linear combination of the two cases of a single wave discussed in Section 4.2.2 (input wave in the CW and input wave in the MW) is realized. Considering only the returning waves of Figure 4. 10, ($\Phi_{r,CW}(k, \omega)$, $\Phi_{t-,CWtoMW}(k, \omega)$, $\Phi_{r,MW}(k, \omega)$ and $\Phi_{t-,MWtoCW}(k, \omega)$), the obtained results are

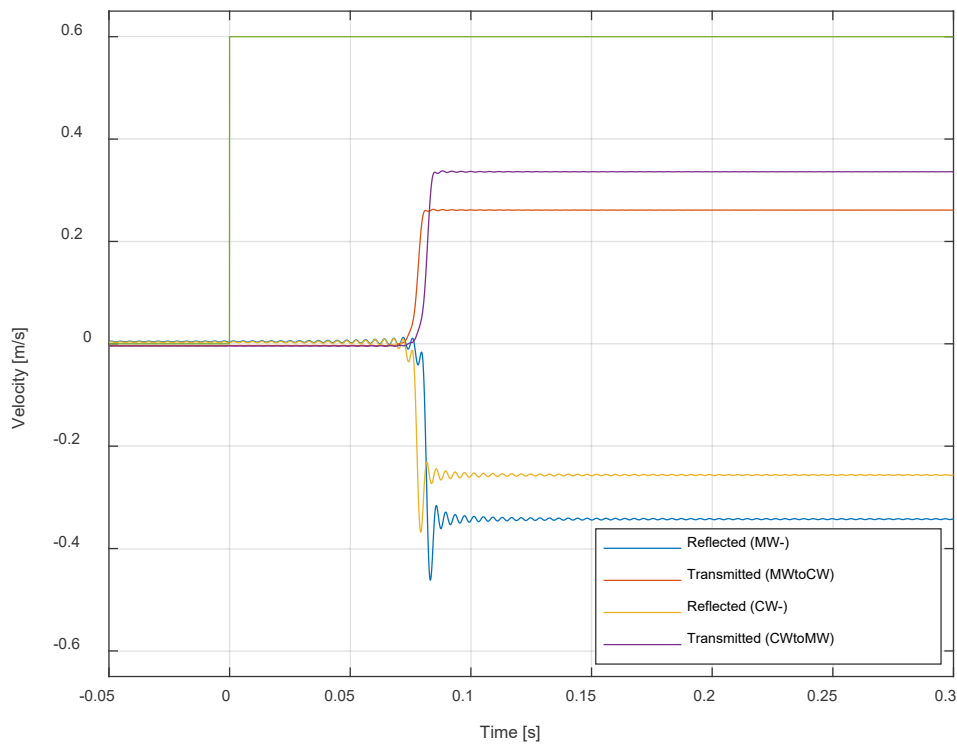


Figure 4. 11 Wave velocities in the MW and CW for a normal dropper mass of 195gr.

The wave delay in the messenger wire and the difference between the two behaviours (CW and MW) is clearer in *Figure 4. 11*.

4.2.3 Mast Behaviour

The final analysis is done for the region near the mast. It is well known that the passage of the pantograph around the mast region is critical, being the source of current collection problems and frequent arcing. (*Vo Van, 2016*).

In this position the MW is connected to the mas through the brackets (*Figure 1. 5* and *Figure 1. 6*). This joint allows rotations in the transversal and vertical axis and displacement on the longitudinal axis; however, incident waves are reflected almost entirely since no vertical displacement is allowed.

For the CW connections and degrees of freedom are different. It is linked to the steady arm which is linked to the registration arm connected to the brackets. The SA is articulated and introduces very low stiffness to the CW; thus, the contact wire is almost free to oscillate on the vertical and horizontal directions being the incident wave almost completely transmitted to the next span.

The wave transmitted on the contact wire that was not reflected by the steady arm, is then reflected and transmitted on the first dropper from the next span. The part of the wave transmitted by the dropper to the messenger wire is not compensated by the wave that should be transmitted from the MW of the previous span (fully reflected wave), and a change in the level of velocity is expected respect to the segments away from the boundary.

The scheme of the configuration used for the simulations is presented on *Figure 4. 12*.

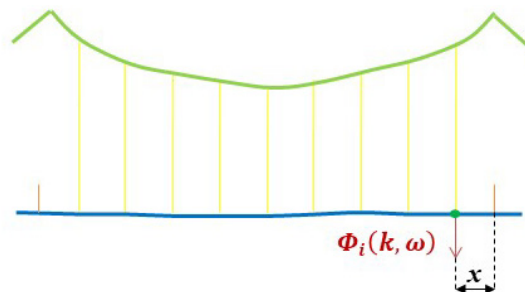


Figure 4. 12 System configurations with an input wave on the last dropper of a span at a distance $2x$ ($x=5m$) from the measuring point (green point). In orange, the steady arm (SA) located at both endings.

In the analytic model, reflections on the steady arm of the contact wire are neglected and only the ones in messenger wire are calculated. On the messenger wire, the incident wave is fully reflected by the mast junction; the reflected wave arrives to the excitation dropper and it is partially reflected, producing the first change on the level of velocity. This wave is fully reflected again on the mast and when it arrives and is partially reflected by the boundary dropper another change in the velocity level is produced. This continues until the trapped wave on the boundary segment attenuates. A scheme for the first four level changes is presented on *Figure 4. 13*.

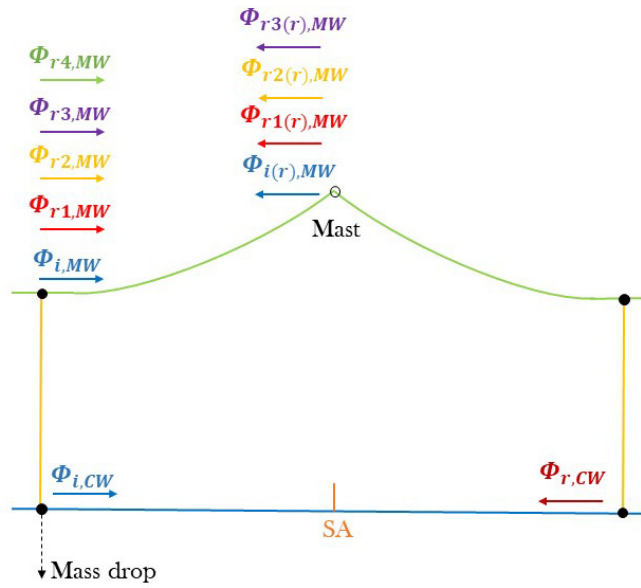


Figure 4. 13 Waves propagating on the boundary segment of the messenger wire after a mass drop below the last dropper

The first four changes of velocity level are plotted on Figure 4. 14 for a time step of 0.6 m/s and a lumped dropper’s mass of 195 gr (“standard” dropper)

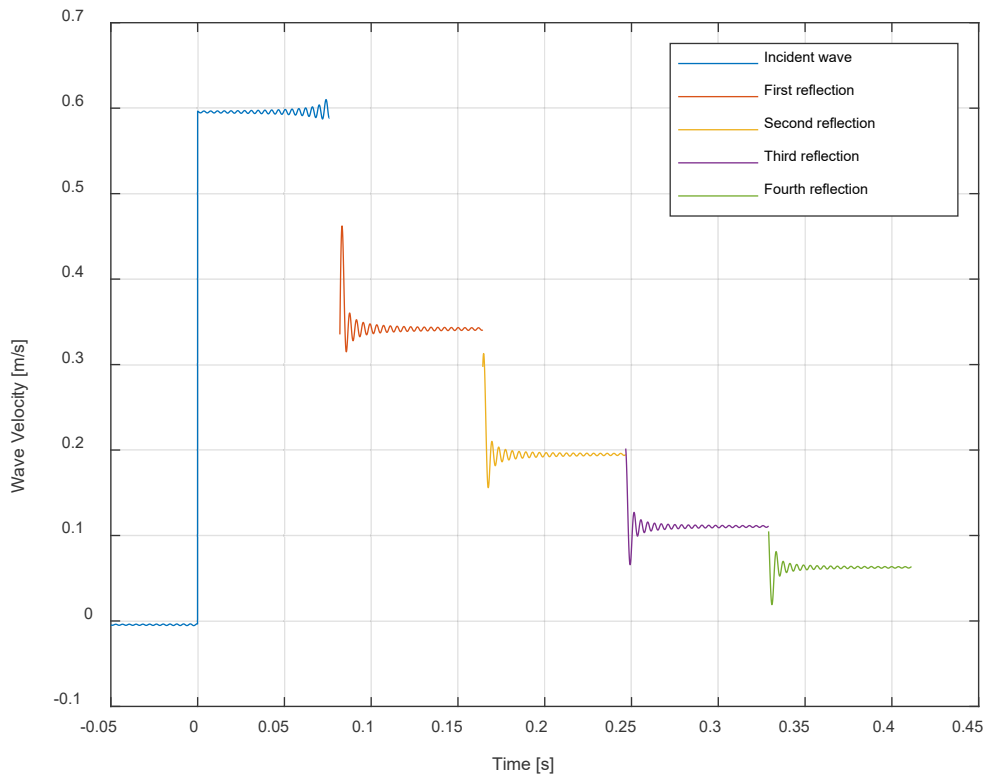


Figure 4. 14 Analytical vertical velocity of the messenger wire after the mass drop: velocity levels obtained after the successive reflections.

The wave remains trapped on the last segment and it is periodically attenuated. It is possible to see that the amplitude of the steps decreases as the velocity wave's amplitude is reduced. This effect extends the wave attenuation in time.

4.3 FEM Result

The experiences realized in *Sections 4.1* and *4.2* were simulated with the help of a catenary system discretized with a FEM designed by the DIRG Research Group of Politecnico di Torino. The obtained velocity diagrams were compared with the analytic ones to determine the validity of the models.

4.3.1 Lumped Mass Simulations

The analytic model used for the comparison with the simulation results was slightly different than the used in section 4.1. Particularly, the lumped mass was considered to be higher (9.6 kg) as well as the dopped mass (20.2 kg). The position of the mass drop is on the contact wire segment, at around 15 meters of the mast. The lumped mass, on the other hand, is located on the steady arm junction. The total length travelled by the wave is 20m, with the input position at 15m from the lumped mass and the output registration being done at 5m from it. Parameters used for the FEM simulation are summarized in *Table 4. 2*.

Parameter	Value	Description
T_{CW}	22	Axial tension force exerted on the contact wire [kN]
T_{MW}	16	Axial tension force exerted on the messenger wire [kN]
μ_{CW}	1.35	Linear mass of the contact wire (string hypothesis) [kg/m]
μ_{MW}	1.08	Linear mass of the messenger wire (string hypothesis) [kg/m]
m_{cw}	0.195	Mass of the steady arm junction in the contact wire [kg]
m_{mw}	0.195	Mass of the steady arm junction in the mounted wire [kg]
m^*	9.6	Lumped mass on the steady arm [kg]
m^{**}	21.1	Mass dropped to generate the step velocity
d_{SA}	0	Damping of the steady arm [Nm/s]
k_{SA}	$1 \cdot 10^1$	Stiffness of the steady arm [N/m]
x	20	Total distance travelled by the wave [m] (Analytic)
x_p	15	Relative distance from the lumped mass to the excitation point [m] (FEM)
x_r	5	Relative distance from the lumped mass to the measuring point [m] (FEM)

Table 4. 2 Parameters used in the lumped mass analytic calculation and FEM simulation

As already explained in *Section 4.2.3*, when the contact wire arrives to the mast it is linked to the steady arm with an articulated joint, giving low stiffness on the radial direction. If no mass is attached to the arm, reflections can be considered to be negligible and the whole wave tends to be transmitted to the other span.

For the simulations, the steady arm is modelled as a dropper with negligible stiffness, with and without an additional mass, to simulate the case where waves are reflected and the case where reflection does not occur. The no mass case considers only the estimated mass of the steady arm joint (0.2 kg). Following the procedures of *Section 4.1*, different time-steps are chosen ($dt=0.003s$, $dt=0.001s$ and $dt=0.0001s$) for the two used numerical methods (α -method and Newmark method).

The obtained results are plotted in *Figure 4. 15*.

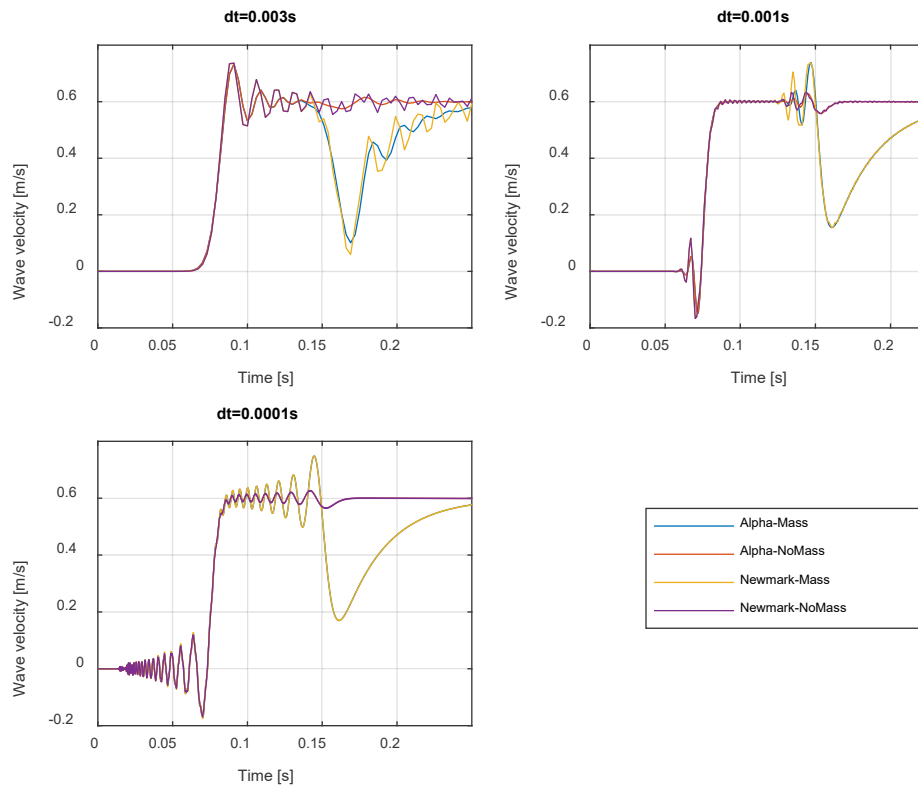


Figure 4. 15 Wave reflections on a lumped mass of 9.6 kg located on the steady arm for an input generated with a mass drop of 21.1 kg

The first characteristic that can be spotted is the wave dispersion with the two smaller time steps. The dispersive phenomena are not clear for the time step $dt=0.003s$ that, as in the previous studies, shows an inverse behaviour.

As the time step decreases, convergence between both methods is achieved, being almost equal for a time step $dt=0.0001s$. Nevertheless, spurious oscillations are observed with Newmark’s method for a time time-steps of $dt=0.001s$ and $dt=0.003s$.

In the case where the lumped mass is attached to the steady arm, the reflection is clearly seen at around $t=0.16s$ and has a considerable magnitude. On the other hand, for cases where only the mass of the steady arm joint is taken into account, reflection takes place at a close time instant, but it has a considerably lower magnitude. This means that nearly all the wave in the contact wire is transmitted to the next span.

For the comparison with the analytic result, a time step equal to $dt=0.0001s$ is chosen for an analysis with a present lumped mass. The total distance travelled by the wave is again 20m. Parameters used for the analytic simulation are summarized in *Table 4. 2*.

The obtained results for are plotted in *Figure 4. 16*

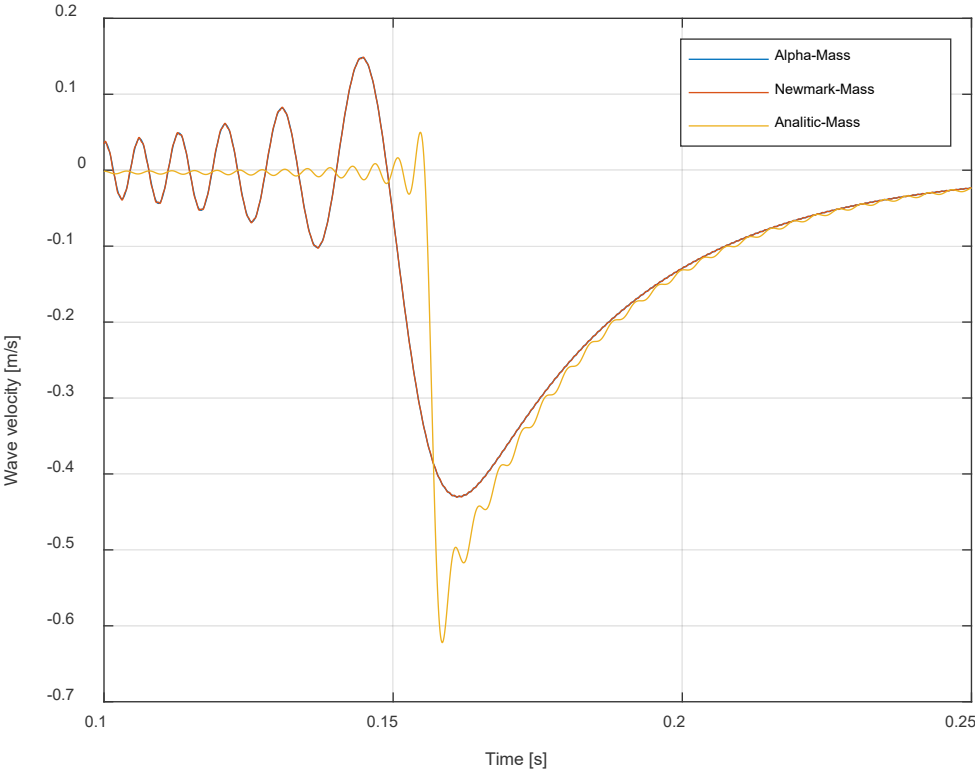


Figure 4. 16 Comparison between analytic and simulated results

Reflection observed in the analytic result is slightly higher than the one shown by the simulation results. Nevertheless, the analytic model is able to show a suitable convergence with the simulated experiment.

4.3.2 Dropper Simulations – One Wire at the Time

To compare the FEM simulations with the analytic results, the continuity of displacement from the *equation (4.81)* was plotted for the contact wire and the messenger wire by creating a step velocity input of 0.6 m/s.

The configuration of *Figure 4. 3* (left hand) is discretized with the Finite Element method and is defined as “FEM A”, and the input force is placed one time on the contact wire and the other on the messenger wire. To generate the step velocity of 0.6 m/s in the contact wire, a mass drop of 20.2 kg is placed at 5m from the dropper and the measuring points are located at +/- 5m from the dropper in analysis. The total length travelled by the wave is in any case equal to 10 m.

Due to the diverse characteristics of the messenger wire, the mass to be dropped needs to be adjusted in order to generate the same velocity step. For this, the dynamic impedance of the wire is considered as

$$m_{MW}^{**} = m_{CW}^{**} \frac{\frac{T_{MW}}{c_{MW}}}{\frac{T_{CW}}{c_{CW}}} \cong 16.1 \text{ kg} \quad (4.89)$$

In the FEM model, the properties of the contact wire are changed for the properties of the messenger wire to carry out the simulations.

The parameters used for the simulations are summarized in *Table 4. 3*

Parameter	Value	Description
T_{CW}	22	Axial tension force exerted on the contact wire [kN]
T_{MW}	16	Axial tension force exerted on the messenger wire [kN]
μ_{CW}	1.35	Linear mass of the contact wire (string hypothesis) [kg/m]
μ_{MW}	1.08	Linear mass of the messenger wire (string hypothesis) [kg/m]
m_{cw}	0.195	Mass of the dropper junction in the contact wire [kg]
m_{mw}	0.195	Mass of the dropper junction in the mounted wire [kg]
m_{cw}^{**}	21.1	Mass dropped in the contact wire to generate a velocity step of 0.6m/s [kg]
m_{mw}^{**}	16.1	Mass dropped in the messenger wire to generate a velocity step of 0.6 m/s [kg]
m^{**}	37.2	Mass dropper below a dropper to generate two step velocities of 0.6 m/s [kg]
d_{drop}	0	Damping of the dropper [Nm/s]
k_{drop}	$1 \cdot 10^5$	Stiffness of the dropper [N/m]
x	10	Total distance travelled by the wave [m] (Analytic)
x_p	5	Relative distance from the lumped mass to the excitation point [m] (FEM)
x_r	5	Relative distance from the lumped mass to the measuring points [m] (FEM)

Table 4. 3 Parameters used for the mass drop near a dropper experiment, for the analytic calculation and FEM simulation

As explained before, the continuity of displacement is plotted with the incident and the reflected waves together (the measurement is realized for the two at the same time), and the transferred wave apart. The results for three different time steps ($dt=0.003s$, $dt=0.001s$ and $dt=0.0001s$) and two numerical methods (α -method and Newmark method) are plotted in *Figure 4. 17* for the CW and *Figure 4. 18* for the MW.

For the contact wire, the results are

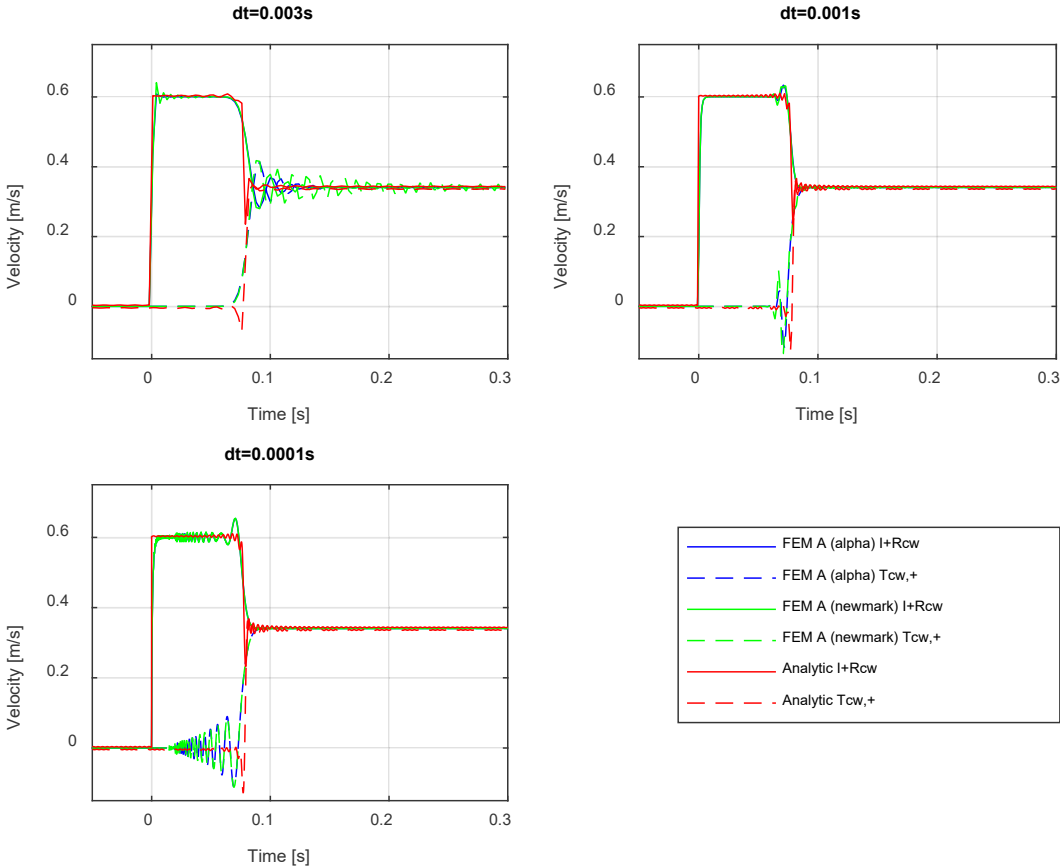


Figure 4. 17 Analytic and simulated wave transmissions and reflections for the CW

Again, the first characteristic that can be spotted is the wave dispersion with the two smaller time steps. The dispersive phenomena are not clear for the time step $dt=0.003s$ that, as in the previous studies, shows an inverse behaviour.

From previous experiments it is known that as the time step decreases, convergence between both methods is achieved, being almost equal for a time step $dt=0.0001s$. Then, only the α -method is used for the smallest stime step. Spurious oscillations are observed with Newmark’s method for a time time-steps of $dt=0.001s$ and $dt=0.003s$ and higher oscillations are observed for the smallest time step.

As the transmitted wave and the sum between the reflected and input wave converge after the reflection, it is possible to say that *equation (4.81)* is respected and both the analytical and simulated results are coherent.

For the messenger wire, the results are

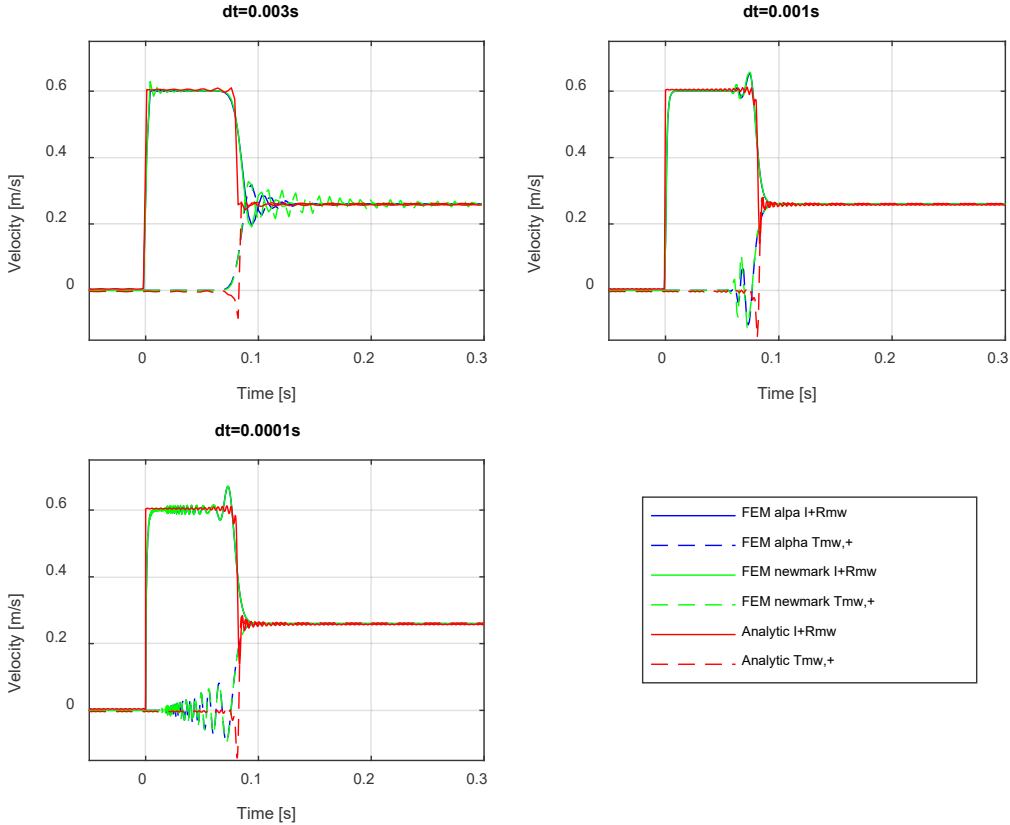


Figure 4. 18 Analytic and simulated wave transmissions and reflections for the MW

Analogous properties to the ones observed in Figure 4. 17 can be seen for the messenger wire, equation (4.81) is respected and both the analytical and simulated results continue to be coherent.

Further observations can be done from both figures. For the contact wire the reflected component seems to be considerable smaller than the transmissive component, this means that the wave is more likely to be transmitted than reflected. In the case of the messenger wire the effects are quite the opposite, been the reflective component the dominant one. This means that the wave will likely remain trapped between two droppers and transmission will remain as a secondary effect.

4.3.3 Dropper Simulations – Two Wires at the Time

Another possible analysis is made using the configuration shown in *Figure 4. 3* (right side), it is discretized by the Finite Element method and defined as “FEM B”. With this configuration, two waves are simultaneously generated by a mass drop right below the dropper linking the contact and messenger wires positioned at 5m from another dropper. The chosen mass is a summatory of the masses used for the mass drop experiments in the contact and messenger wires

$$m^{**} = m_{CW}^{**} + m_{MW}^{**} = 37.2 \text{ kg} \quad (4.90)$$

where m_{CW}^{**} is the mass drop needed to generate a velocity step of 0.6 m/s in the CW and m_{MW}^{**} is the mass drop needed to generate a velocity step of 0.6 m/s in the MW.

To standardize the comparison, the analytic and simulated results are weighted by the coefficients determined in *equations (4.86)* and *(4.87)*. For simplicity the transmission coefficient at 0 Hz is considered to be

$$a = \frac{\frac{T_{CW}}{c_{CW}}}{\frac{T_{CW}}{c_{CW}} + \frac{T_{MW}}{c_{MW}}} \cong 0.5673 \quad (4.91)$$

The weighted sum of the observed waves in the contact and messenger wires becomes

$$sum = (r_{CW} + t_{drop,MWtoCW})a + (r_{MW} + t_{drop,CWtoMW})(1 - a) + i \quad (4.92)$$

It is also possible to arrive to the similar simulated results by summing the waves measured with the configuration of FEM A for each of the wires and weighting them. The analytic results are calculated in an analogous way for a total distance travelled by the wave of 10 m. The measuring point and the excitation point are located at a distance of 5 m from the second dropper.

The parameters used for the simulations are summarized on *Table 4. 3*.

In summary, simulations are done for three different time steps (dt=0.003s, dt=0.001s and dt=0.0001s) and two numerical methods (α -method and Newmark method), considering two different FEM configurations (a combination of two “FEM A”, one with an input in CW and the other with an input in the MW, and “FEM B”).

The obtained results are shown in *Figure 4. 19*

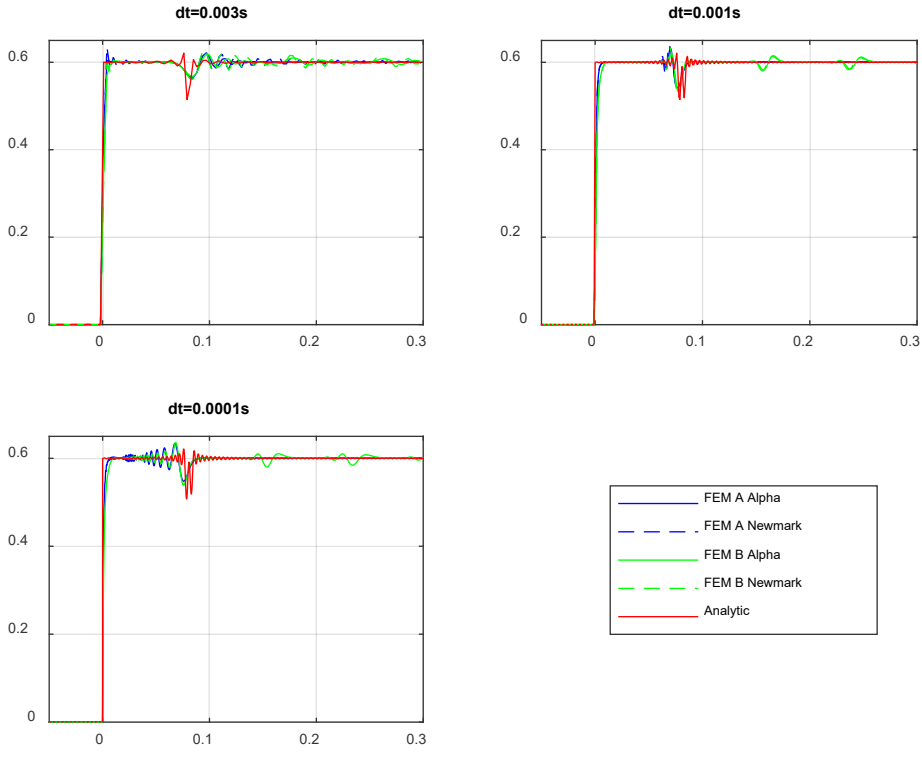


Figure 4. 19 Comparison between the sum of the transmitted, reflected and incident waves computed using FEM A, FEM B and analytically computed

Analogous properties can be spotted for the time-step reduction, for the biggest time step dispersion cannot be spotted and an inverse behaviour is indeed represented while for smaller time steps dispersion is clear.

Two main oscillations can be seen just before 0.1 s on the analytic results, this represents two different reflections for each wire, and it is due to the different phase velocities. The first is the reflection on the CW, being the one with higher velocity, and the second is the one occurring in the MW.

On the FEM results, the oscillation is distorted by the presence of higher frequency oscillations from the dispersive effects.

It is possible to say that a velocity wave compensation occurs at the droppers, with the slight delay between velocities only inducing short time variations

4.3.4 Mast Simulations

As previously said, waves on the MW are fully reflected while waves on the CW are considered to be almost fully transmitted.

In this section, simulations are done with a time step $dt=0.001s$ for two numerical methods (α -method and Newmark method). The simulated results are compared with the analytic levels calculated on *Section 4.2.3* on *Figure 4. 20*.

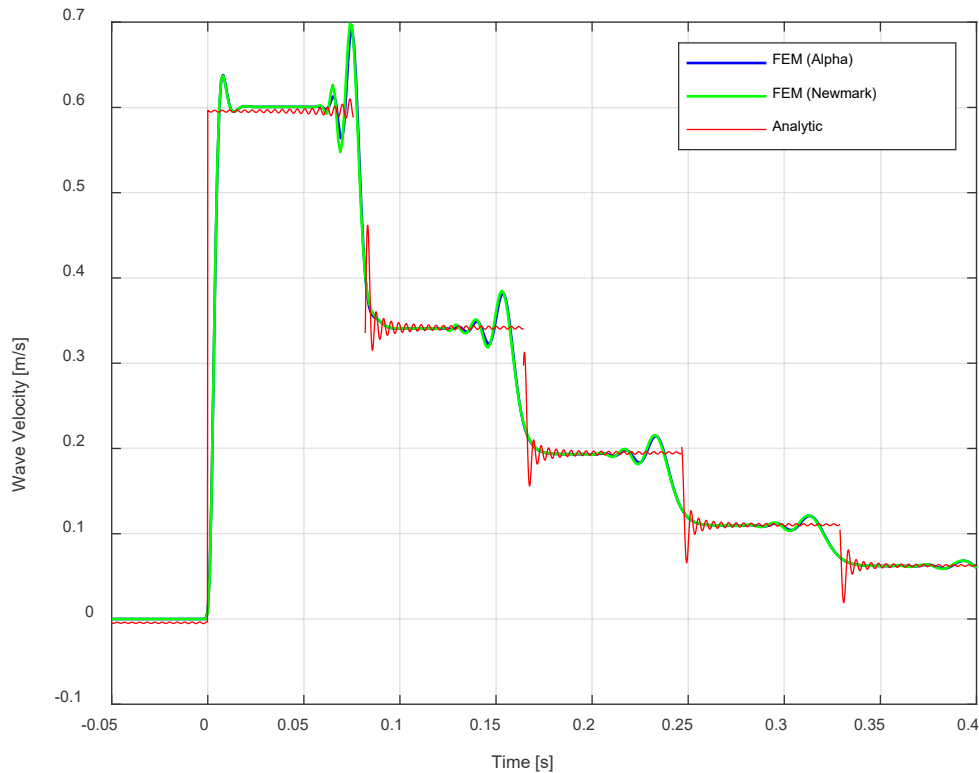


Figure 4. 20 Simulated wave's reflection compared to the analytic results.

The results of the simulations correspond to the results obtained on the analytic analysis. Each velocity level converges for both of the methods that have an analogue behaviour with a time step of $dt=0.001s$. The progressive attenuation of the wave can be observed after each of the reflections detailed on *Figure 4. 20*.

As a final comment, the reflected waves after a mass drop producing an input velocity wave of 0.6 m/s are plotted on *Figure 4. 21*. The simulation is generating by taking out the dropper from the last position in order to get the total reflections.

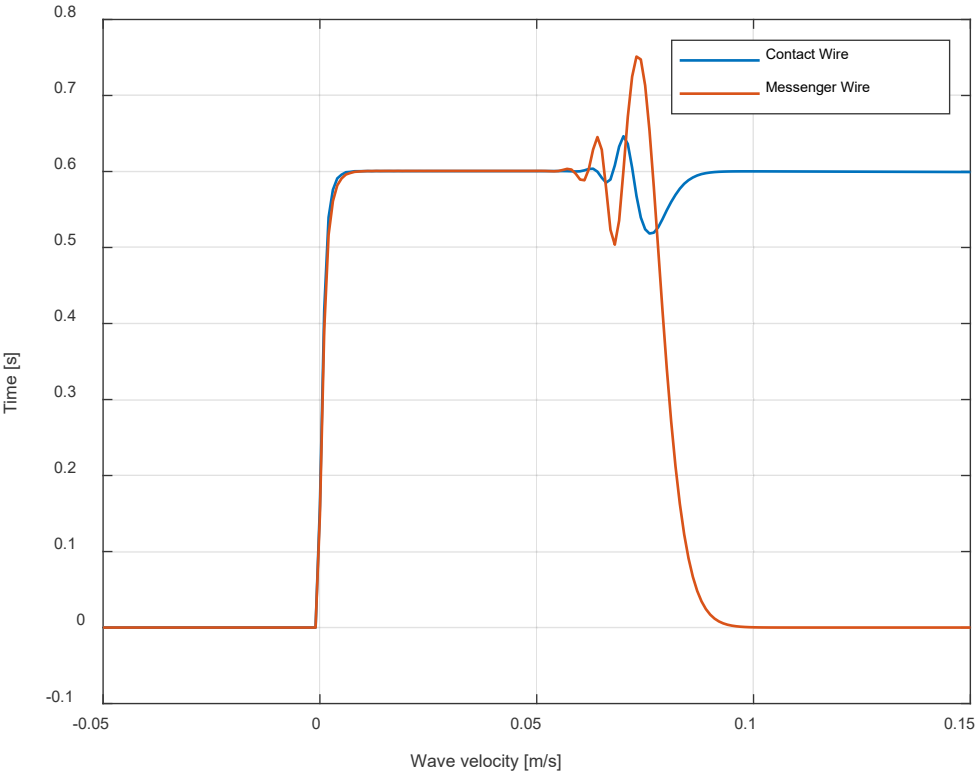


Figure 4. 21 Reflected waves on the mast (Messenger wire) and the steady arm (Contact wire) after mass drop generating an input velocity of 0.6 m/s

It is possible to observe that for the steady arm with an estimated mass of 330 gr (CW) the reflection is almost negligible, almost the whole wave is transmitted to the next span. On the other hand, the reflection produced by the mast junction (MW) is complete, generating a completely reflected wave towards the last dropper of the span in analysis.

Since no wave passes to the next span from the messenger wire, velocity compensation does not occur on the first dropper equilibrium as previously discussed. This lack of velocity compensation will generate a change on velocity level. Hence, the study of transmissive and reflective phenomena takes a special importance on the region around each mast.

Chapter 5

Conclusion

In this final chapter, a summary of the results is displayed adding final comments on the outcomes. Some additional future works are proposed for the continuation and complementation of the study.

5.1 Summary

The contact stiffness has demonstrated to be a useful parameter to model contact systems based on Hertz theory. For usual frequency bandwidths of interest [0 – 20 Hz] or [0 – 70 Hz], values of contact stiffness of the order of 1.8 or 2 MN/m produce convergence on the system, putting away resonances from the studied frequency range and maintaining a secure distance from numerical divergences. Nevertheless, numerical instability is found on central regions for the bandwidth of [0 – 70Hz] as seen in *Figure 2. 12*, these results must be studied and analysed in further simulations.

In *Chapter 2* the periodicity of the contact force variation respect to geometry was revealed. Nevertheless, this result is incompatible with reality since it is calculated based on the hypothesis of a rigid contact wire. In real contact wires, the displacement is allowed hence, the dynamic of the catenary system must be considered. Contact force fluctuations on flexible wires produce mechanical waves all along the powered line contributing to the fluctuations on the sliding contact system.

In order to study the importance of these generated waves on the system, the contact and messenger wires are model with two different hypotheses: the string hypothesis and the tensioned Euler-Bernoulli beam hypothesis. The first has demonstrated to be useful to predict waves velocities on low frequency spans, as the standard bandwidth of [0 - 20Hz], but this model cannot explain the dispersion phenomena, introduced on *Chapter 3*. A tensioned Euler - Bernoulli model is chosen in order to be able to observe the effects of mechanical waves dispersion and a clear difference between wave velocities calculated with each of the models is spotted on *Figure 3. 2*.

The wires are defined as dispersive mediums and it is possible to study the dispersion in a simply supported and tensioned Euler-Bernoulli beam model after it is discretized using FEM. The response in time of the system to two different excitations (sinusoidal and impulse) is calculated with two different numerical methods and time steps: HHT- α and Newmark method with time steps of $dt=0.003s$ and $dt=0.001s$. The first interpretation of the obtained results is that in order to observe dispersion the time step needs to be equal or lower than $dt=0.001s$, since bigger time steps exhibit a non-realistic inverse behaviour. The second conclusion is that HHT- α method with a calibrated negative α -dissipation ($\alpha=-0.1$) is more appropriate to evidence the dispersion phenomena, avoiding spurious oscillations produced by the excessive dissipation in lower frequency modes generated by the Newmark method and eluding an excessive dissipation of the higher modes produced by the negative α -dissipation. (see *Figure 3. 13* and *Figure 3. 14*).

Subsequently, wave reflection and transmission are explained in *Chapter 4*. The string theory-based models proposed by (Vo Van, 2016) are shown to be effective to indicate and evidence this two phenomena. As the mass of the junctions present on the wires grows, predominance of reflection increases to the detriment of transmissive effects. The contact wire is characterized as a mainly transmissive medium while the messenger wire is defined as a mainly reflective one, this means waves on contact wires are more likely to be transmitted while waves on the messenger wire are more likely to be reflected. Thus, reflection and transmission are demonstrated to be strongly related to the material of the wires, particularly to the mass per unit of length. Finally, with a chosen material, the tension of the wires is shown to be the only parameter that modifies transmission and reflection coefficients at null frequencies.

A correct amount of damping on the droppers helps to isolate the dynamics of the contact wire from the one of the messenger wires, nevertheless, an excessive damping produces a coupling between the two behaviours favouring wave transmission from one wire to the other. Wave transmission from one cable to the other may not be totally unwanted if the amplitude of the motion is controlled, since the messenger wire by receiving transmitted ways may be acting as a sort of energy dissipator. Waves showed to have different velocities on each of the wires so, small delays are expected to take place from one dropper to the other.

The transmitted and reflected waves are compensated in each of the segments of the span, except the ones limiting with the masts. In this region, waves on the contact wire are almost fully transmitted thanks to the steady arm flexibility (see *Figure 1. 4*, left side) while waves on the messenger wire are fully reflected due to the junction of the wire and the brackets shown on *Figure 1. 5*. The reflected wave remains trapped on the last segment and the transmitted wave is reflected by the first dropper of the next span. This reflection is thus non-compensated and a change on velocity level is expected on the limiting segment of the following span.

Therefore, special attention needs to be given to the dynamic of the border segments of each span.

Finally, the validity of the analytic models proposed is verified with the response of a FEM discretized system to similar excitation functions (step velocity functions simulating mass drops). The response is calculated with both a Newmark and HHT- α methods for different time steps. Analogous behaviours to the ones described in *Chapter 3* are exhibited with both methods. On *Figure 4. 19* wave compensation effects on droppers are shown. However, analytic results calculated for a non-dispersive medium (string hypothesis) cannot show the higher frequency effects and differ with the results with the FEM, considering a dispersive medium (Euler-Bernoulli beam model). These higher frequency effects produce distortions on the summatory generating a slightly different response.

5.2 Proposed Future Works

To deepen and verify the analysis of the realized work future studies are proposed.

For studies related with the contact force, it is possible to control the results obtained with the analytic model by simulating the contact force on a discretized model. The FEM model must take into account the flexibility of the messenger and contact wires, this will allow to see the direct impact of wave dispersion on the contact system and will make more evident the divergence between the force calculated with the analytic model that takes into account only the geometry of the system and the force calculated in the simulation that considers the geometry and flexibility of the wires.

This analysis will have to make emphasis on the droppers' dissipative effects and its relationship with the messenger wire dynamics. It would be interesting to see if it is possible to use the messenger wire as a dissipative body or if transmitted waves only contribute to the instability of the system.

Following the contact force analysis, contact stiffness effects must be studied in detail, together with the numerical limitations of the contact theory. Further contact theories or approaches may be applied, and their results compared to the ones obtained in this analysis. For the analytic model, the possibility of applying semi-elastic contact approaches could be studied like the one proposed by (Schupp, Weidemann, & Mauer, 2006) for the study of the wheel-rail contact. This kind of approaches would avoid numerical problems induced by the high contact stiffnesses of the elastic approach.

It would be interesting to study the possibility of applying other contact theories, similar to the ones used in the study of the wheel-rail contact, in order to introduce the effects of friction forces on the sliding contact system. The study of already proposed wear models, as the ones realized in the Politecnico di Milano (Bucca & Collina, 2007), can also be used to this aim.

The main experiments may be realized by doing field tests, realizing acceleration measurements under controlled excitation functions such as mass drops or sinusoidal excitations on wire systems following the norm detailed in ((CENELEC), 2018). It is important to check the validity of the used models and to improve the FEM discretization's with new parameters that may not have been taken into account.

Further design strategies should be realized taking into account the material of the wires, to observe more deeply the dissipation properties and main effects of the mass per unit of length and the tension. Nevertheless, these variations do not have to modify excessively the phase velocity of one of the wires respect to the other since high velocity differences between the two wires would produce imbalances on the droppers.

Finally, the effects of the third lumped mass of the pantograph model needs to be examine in detail. The third mass, together with the contact stiffness parameter, are the responsible of the contact resonance, that affects directly the modelling of the system. Bigger masses generate contact resonances closer to the frequency bandwidths under study.

Appendices

A. Procedures for the Analysis on the Time and Frequency Domains

For the study of the passages from the time domain to the frequency domain and vice versa, a simple exercise is proposed to facilitate the understanding of the constants needed to follow the correct procedure.

A sinusoidal signal is generated in the time domain [0 – 2 s], containing two different harmonics

$$y = \sin(\omega t) + \sin(3\omega t) \quad (A.1)$$

where $\omega = 2\pi f$, with $f = 10\text{Hz}$.

The signal is later filtrated to leave only the first harmonic component with a Butterworth, low pass filter designed in MATLAB (*butter* function) and applied with the command *filtfilt*.

```
fCut=20/(fs/2);
try
    [B,A]=butter(10,fCut);
    yc1=filtfilt(B,A,y);
catch
    yc1=y;
end
```

This filtered signal is left for comparison and the procedure continues with the Fast Fourier Transform of the non-filtered signal and the obtention of the frequency response function of the Butterworth filter. The FRF of the filter is done by using the command *freqz*.

FFT of the non-filtered signal

```
Nx=length(y);
Nx2=floor(Nx/2+1);
YDS=fft(y,Nx)/Nx;
xDS=fs*(0:Nx-1)/Nx;
YSS=2*YDS(1:Nx2);
xSS=fs/2*(0:Nx2-1)/Nx2;
```

FRF of the filter

```
[H,W]=freqz(B,A,Nx2);

H=reshape(H,[1,length(H)]);
```

The FRF of the filter is then multiplied by the single sided spectrum of the signal in the Fourier domain.

Multiplication of both FRF

```
YH=H.*YSS;
```

Finally, the Inverse Fourier Transform of the result is realized and compared with the filtered signal.

IFFT

```
yc2=ifft(YH,'symmetric')*(-Nx2/2);
```

```
dt2=linspace(0,2,length(yc2));
```

The obtained signal is compared with the original filtered signal in *Figure A. 1*.

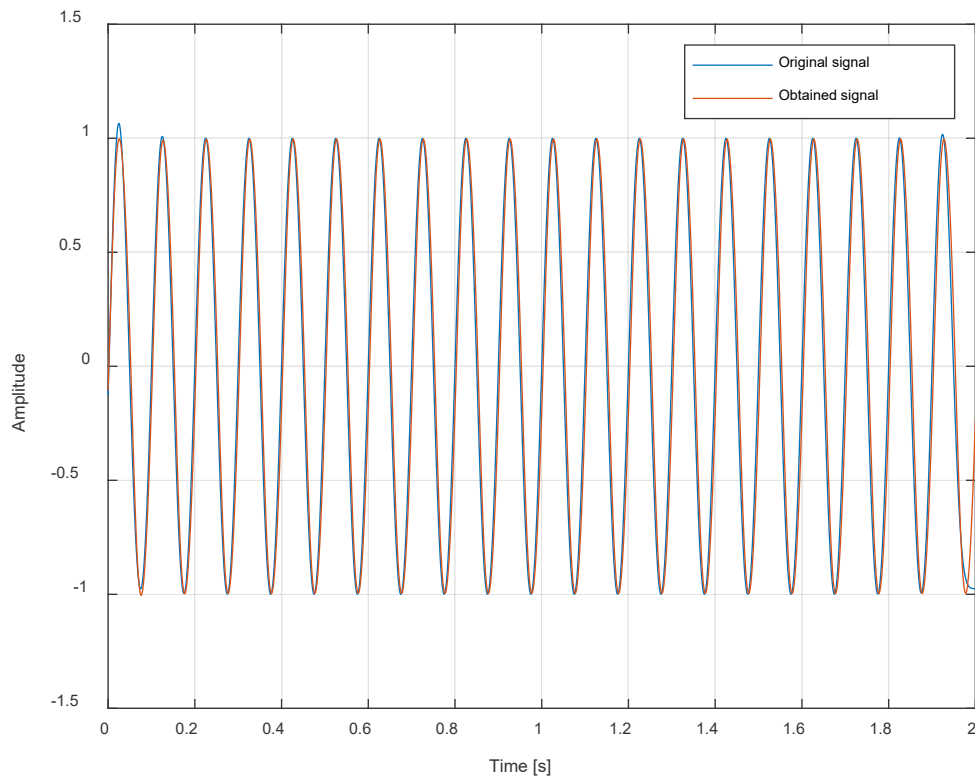


Figure A. 1 Filtered (original) signal vs the obtained signal

B. Flow Charts of the Used Numerical Methods

The flowcharts of Newmark and α -method are design in this appendix.

For the Newmark method

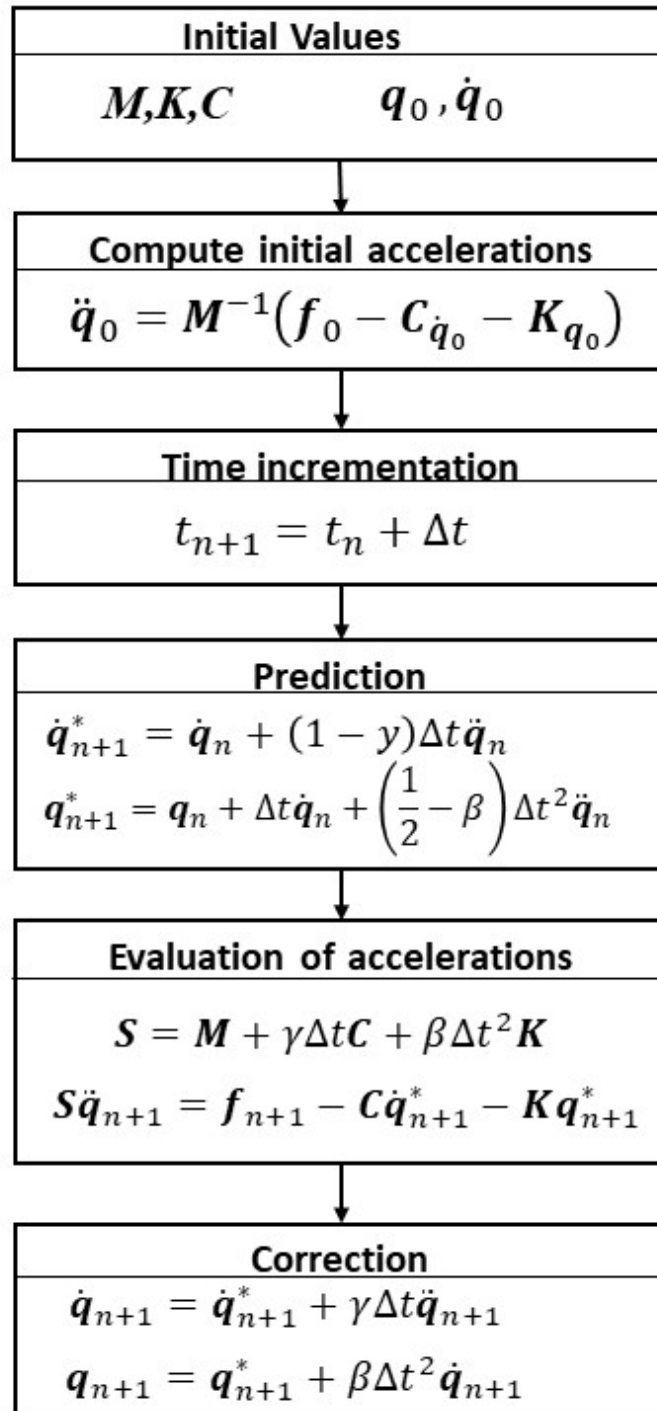


Figure B. 1 Flow chart of the Newmark scheme. Adaptation from (Géradin & Rixen, 2015)

For the HHT- α method

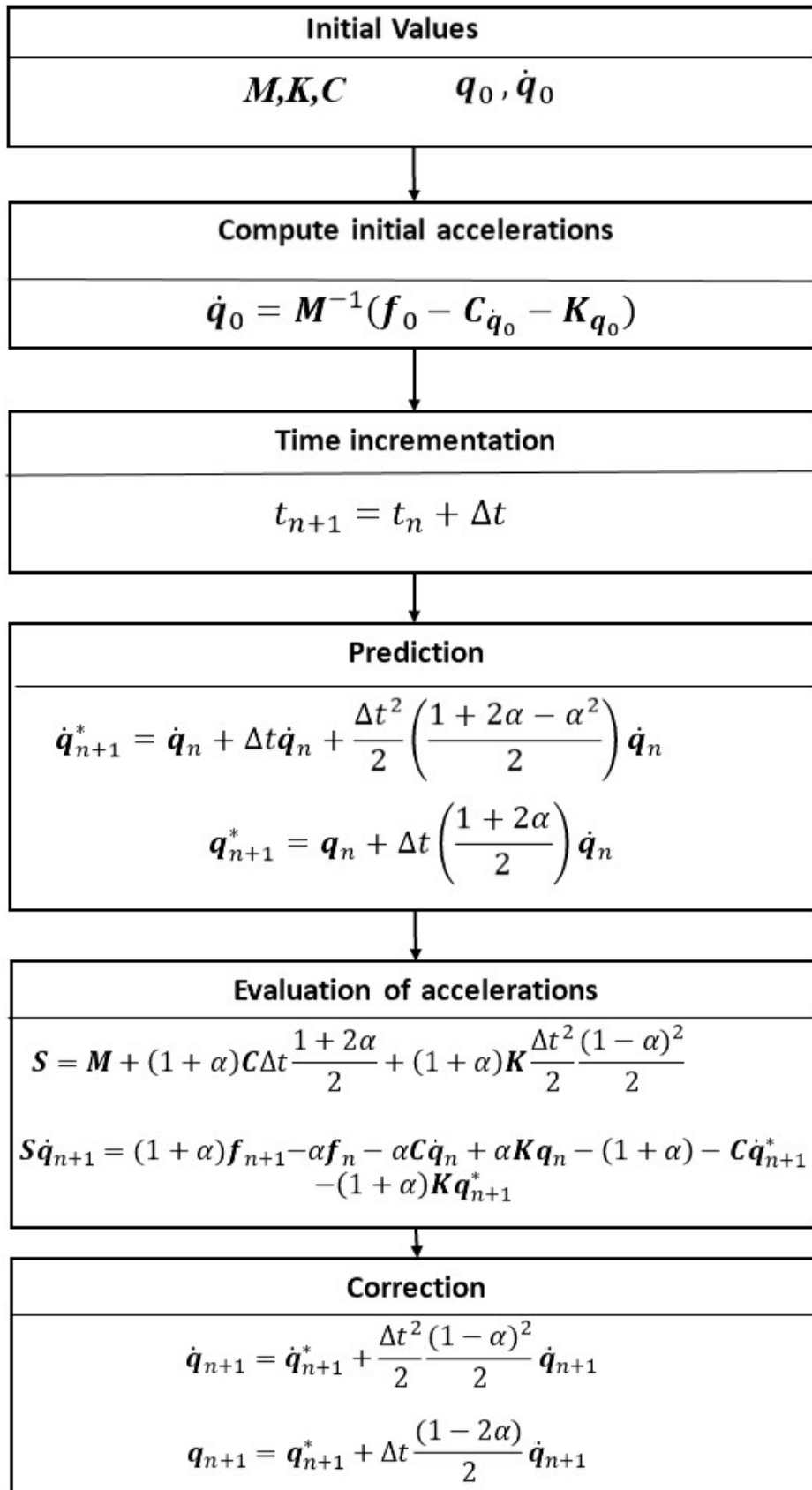


Figure B. 2 Flow chart of the Alpha scheme. Adaptation from (Gérardin & Rixen, 2015).

C. Procedure of the Wave Velocity Calculation in Dispersive Mediums

Wave accelerations are calculated following a digital analysis procedure proposed in (Hyeon Cho, 2008).

To begin, the input and output signals from the discretized system are obtained with the use of both numerical methods (Newmark and HHT- α) with two different time steps ($dt=0.001s$ and $dt=0.003s$) for three different excitation frequencies ($f_1=20Hz$, $f_2=50Hz$ and $f_3=100Hz$). The calculated signals for each of these cases constitutes the data base of the analysis. The excitation function is of the type of

$$f(t) = 10 \sin(2\pi f \cdot t) \quad (C.1)$$

Once on the analysis code, the data base is loaded to begin the operations with the signals.

```
load Fsinusoide.mat
```

The group of signals to be processed are chosen and their main parameters defined. In the example case the chosen group is the one solved with Newmark method, for a frequency $f=100Hz$ and with a time step $dt=0.001s$ (`ydotdotN6` from the data base). The sampling frequency is defined with the time step.

Signal parameters definition

```
ydotdotin=ydotdotN6(1,:);  
ydotdotout=ydotdotN6(2,:);  
  
dt=0.001;  
fs=1/dt;
```

The selected signals are plotted in the time domain on *Figure C. 1*.

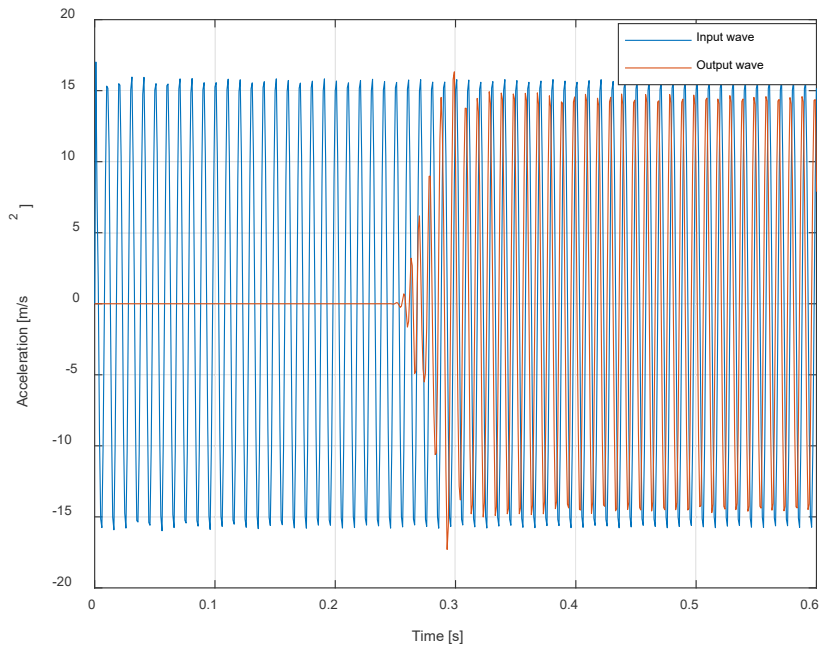


Figure C. 1 Input and Output signals for a frequency of 100 Hz and $dt=0.001s$.

Following the analysis, the correct FIR filter is chosen for the filtering of the signals. In this case a band-pass filter isolating the frequency of 100 Hz or Hd3, introduced using the *filter* function from MATLAB.

Filtering of the signal

```
% 20Hz
% ydotdotinf=filter(Hd1,ydotdotin);
% ydotdotoutf=filter(Hd1,ydotdotout);

% 50Hz
% ydotdotinf=filter(Hd2,ydotdotin);
% ydotdotoutf=filter(Hd2,ydotdotout);

% %100Hz
ydotdotinf=filter(Hd3,ydotdotin);
ydotdotoutf=filter(Hd3,ydotdotout);
```

The filtered signal is plotted *Figure C. 2*.

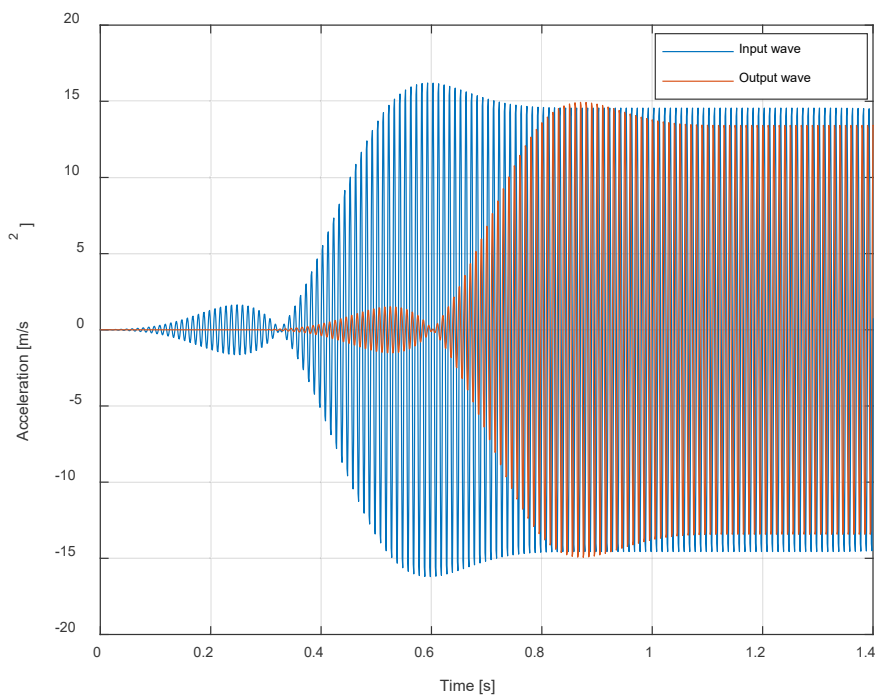


Figure C. 2 Input and Output filtered signals for a frequency of 100 Hz.

With the filtered signals, the Short Fourier Transform is performed with the function *spectrogram* from MATLAB. The windowing is done using Hamming windows of 20 samples each with an overlap of 50%. The number of spectral lines is $nfft=2^9$ and the sampling frequency is the one defined before with the time step ($fs=1000Hz$).

Short Time Fourier Transform (STFT)

```
nfft=2^9;
window=20;
noverlap=round(window*0.5);

[Sin,Fin,Tin]=spectrogram(ydotdotinf,window,noverlap,nfft,fs);
[Sout,Fout,Tout]=spectrogram(ydotdotoutf,window,noverlap,nfft,fs);
```

From the function *spectrogram* two vectors (F and T) and one matrix (S) are obtained. The vector F is the vector of the frequency domain, T is the vector of the time domain and S is the spectrogram matrix.

The procedure is followed by searching the location of the frequency of interest on the frequency vector and plotting the corresponding column of the spectrogram matrix on the time domain. This is done for both signals.

The obtained plot is the spectrogram at 100 Hz on the frequency domain. It is plotted on *Figure C. 3*.

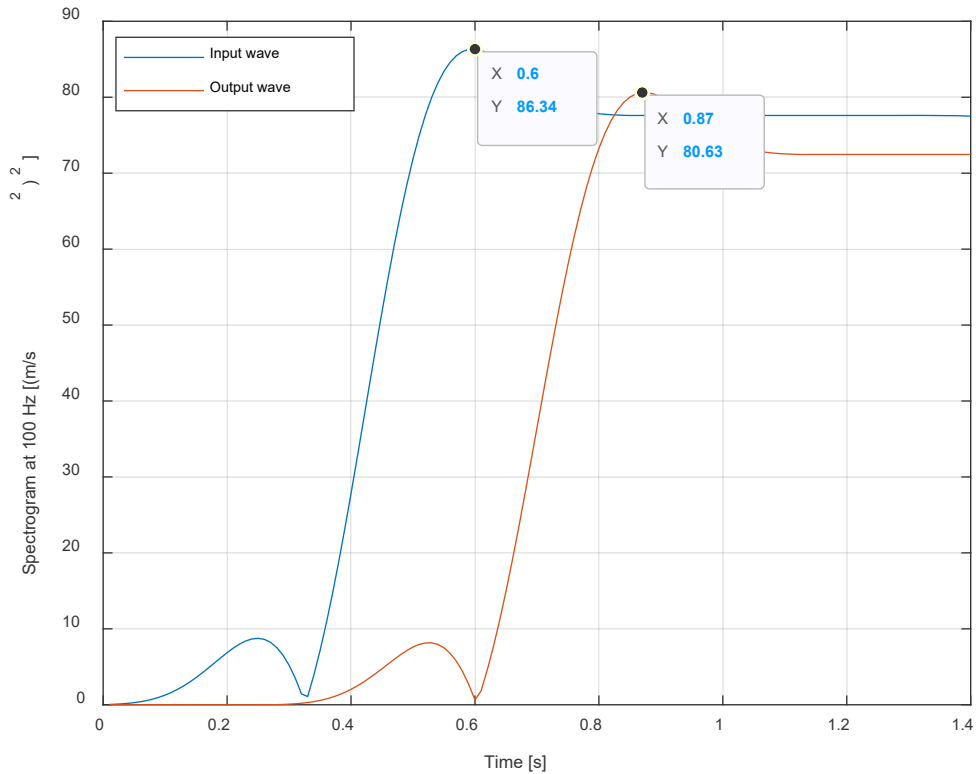


Figure C. 3 Spectrogram at 100 Hz on the time domain

The maximum points of each signal are evidenced in order to get the time delay between the two waves. Knowing the distance between the excitation point and the measuring point ($x=40$ m), it is possible to calculate the wave velocity by making a simple calculation of the type

$$v = \frac{x}{\Delta t} = \frac{40 \text{ m}}{0.87\text{s} - 0.6\text{s}} = 148.15 \frac{\text{m}}{\text{s}} \quad (C.2)$$

The procedure is repeated for the other signals with the aim of calculating the wave velocities for each of the cases.

D. Comments on Digital and Analogue Filters

A filter is, as defined in (Wanhammar & Saramäki, 2020), a device that is required to have a prescribed response for a given input signal. The response requirements may be given in terms of its behaviour in frequency domain, the time domain or both.

The most common are the low-pass filter, the high-pass filter, the band pass filter and the band stop filter. For each one of these filters an ideal transfer function is defined, as the ones shown on *Figure D. 2*

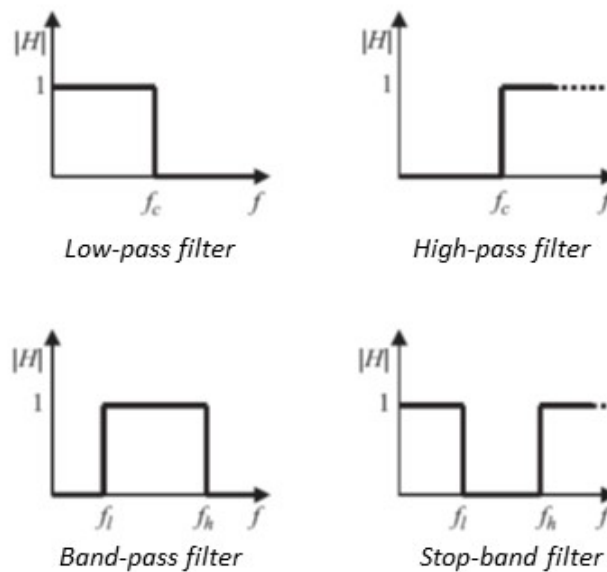


Figure D. 1 Transfer functions of the main kind of filters. Adaptation from (Mwakali & Taban-Wani, 2006)

In real filter applications, square waves are not practical because the filter needs some time to drop down to the stop band. Therefore, it is necessary to give the filter some space to reach the stop band.

D.1 FIR Filters

Digital filters can be defined also as a system with an input and output ports with a transfer function depending on frequency of the type shown in *Figure D. 1*. Thus, a filter is a Linear Time Invariant system (LTI), a system that generates an output from any input signal restricted to linearity and time-invariance.

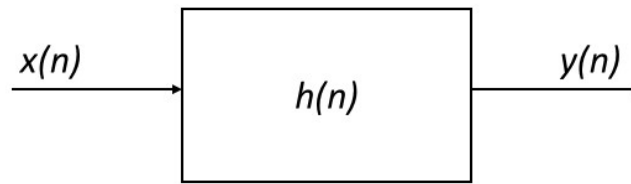


Figure D. 2 Digital filter scheme

where the $x(n)$ is an input sequence, $h(n)$ is an impulse response sequence and $y(n)$ is the output sequence of the system in the discrete - time domain. Since any input can be expressed as the sum of scaled delayed unitary impulses, the total response $y(n)$ to the input sequence $x(n)$ is

$$y(n) = \sum_{k=-\infty}^n h(n-k) x(k) \tag{D.1}$$

$$y(n) = \sum_{k=-\infty}^{\infty} h(n-k) x(k)$$

The first equation is for a causal system, this means that the output of the system depends only on past and present inputs ($h(n) = 0 \forall n < 0$). The second equation is for a non-causal system, this kind of systems have outputs that depend also on future inputs. Since the first equation is a special case from second, the non-causal system will be used from now and on for the rest of the analysis. The definitions from *equation (D.1)* can be named as convolution sums, and they describe the input-output relationship on the time domain.

$$y(n) = x(n) * h(n) = \sum_{k=-\infty}^{\infty} h(n-k) x(k) \tag{D.2}$$

To solve this equation in a simpler way, it is necessary to pass to the frequency domain. Knowing that the z-transform of a convolution on the time domain gives a multiplication on the frequency domain (analogously to the Fourier transform), as explained in (Fasana & Marchesiello), *equation (D.2)* becomes

$$H(z) = \frac{Y(z)}{X(z)} \tag{D.3}$$

A sequence of input-output relationships can be defined for a digital system on the discrete-time domain by using difference equations, see (Shin & Hammond, 2008), as

$$y(n) = - \sum_{k=1}^N a_k y(n-k) + \sum_{r=0}^M b_r x(n-r) \quad (D.4)$$

Making the z-transform of equation (D.4) and the time shifting property, this is $Z\{x(n-r)\} = z^{-r}X(z)$, it is obtained

$$Z\{y(n)\} = Y(z) = -Y(z) \sum_{k=1}^N a_k z^{-k} + X(z) \sum_{r=0}^M b_r z^{-r} \quad (D.5)$$

Reaccommodating *equation (D.5)*

$$H(z) = \frac{Y(z)}{X(z)} = \frac{\sum_{r=0}^M b_r z^{-r}}{1 + \sum_{k=1}^N a_k z^{-k}} \quad (D.6)$$

The characteristics of the transfer function $H(z)$ can be adjusted to the desired form by choosing the appropriate coefficients a_k and b_r and the orders N and M . The coefficients may not be exact and some arithmetic round-off error may be present, as explained in (Shin & Hammond, 2008).

If $a_k = 0$ for all k on *equation (D.6)*, the filter has a finite impulse response and is, therefore, a non-recursive filter. On the other hand, if $a_k \neq 0$ for at least one k on *equation (D.2)*, it represents a recursive algorithm where some of the previous calculated output results are used to compute the next value.

Digital filters can be characterized into two kinds: if the filter has a finite memory is called FIR filter (Finite Impulse Response Filter), this means that the impulse response sequence has a finite length, while an IIR filter (Infinite Impulse Response Filter) on the other hand, has an infinite memory. In general, FIR filters are non-recursive while IIR filters are recursive.

As exposed in (Wanhammar & Saramäki, 2020), FIR filters are often preferred. The advantages that these filters have over IIR filters are that they can be guaranteed to be stable and may have a linear phase response, without phase distortions. Furthermore, they require shorter data word length than the corresponding IIR filters. Nevertheless, FIR filters require much

higher orders than IIR filters for the same magnitude specifications and they introduce a large group delay that make them unsuitable for many applications.

The impulse response of a causal FIR filter of order N is zero outside the interval $0 \leq n \leq N$ as defined before. The transfer function of an N -th order FIR filter is written as

$$H(z) = \sum_{n=0}^N h(n) z^{-n} \quad (D.7)$$

The poles of the transfer function of a non-recursive FIR filter can only be placed at the origin of the Argand-Gauss plane. The zeros can be placed anywhere in the Argand-Gauss plane. Usually, they are placed on the unit circle (to provide higher attenuation in the stopband) or as pairs that are mirrored in the unit circle. The pole-zero configuration for a band-pass FIR filter with $N=50$ designed with the Remez algorithm from MATLAB is shown in *Figure D. 3*.

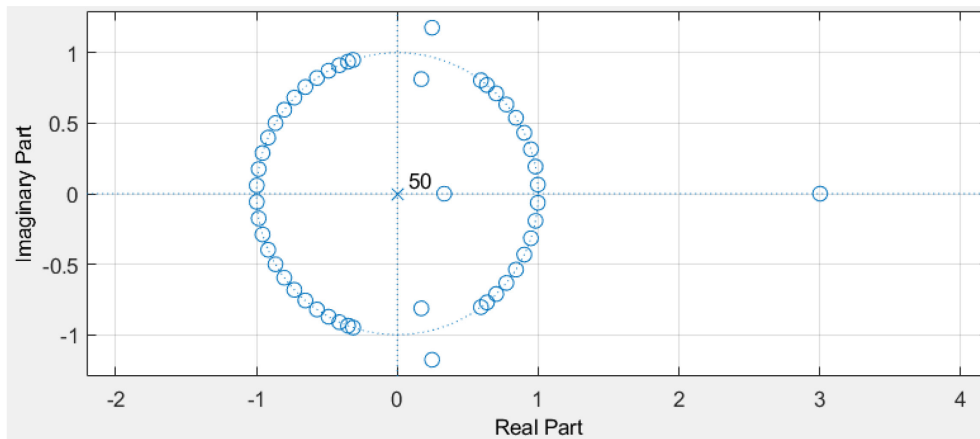


Figure D. 3 Pole-zero configuration for a band-pass FIR filter

By expanding the transfer function of a FIR filter of order N (equation (D.7))

$$H(z) = \sum_{n=0}^N h(n) z^{-n} = \frac{h(0)z^N + h(1)z^{N-1} + \dots + h(N-1)z + h(N)}{z^N} \quad (D.8)$$

where $h(n)$ is the impulse response. The number of poles and zeros will always be the same, except in the case of an overall delay which corresponds to extra poles at the origin.

It is possible to define the FIR filter using the length of the impulse response ($L = N + 1$) instead of the filter's order. Therefore, the number of coefficients on the transfer function is equal to L .

The frequency response is defined as

$$H(e^{i\omega t}) = |H(e^{i\omega t})| e^{i\varphi(e^{i\omega t})} \quad (D.9)$$

where $|H(e^{i\omega t})|$ is the amplitude of the function and $\varphi(e^{i\omega t})$ is the phase of the function. A special case of FIR filters are the ones with linear-phase-response, where

$$\varphi(e^{i\omega t}) = -k\omega t \quad (D.10)$$

where k is a positive constant. Linear-phase filters are not strictly linear since they are only piecewise linear, as defined in (Wanhammar & Saramäki, 2020).

The selected FIR filter was an equiripple FIR filter. Since the magnitude response of digital filters may exhibit ripples near the cut-off frequencies, an equiripple filter is a filter with ripples of equal height. An example of equiripple, band-pass FIR filter with $N = 50$ designed with the Remez algorithm from MATLAB is plotted on *Figure D. 4*.

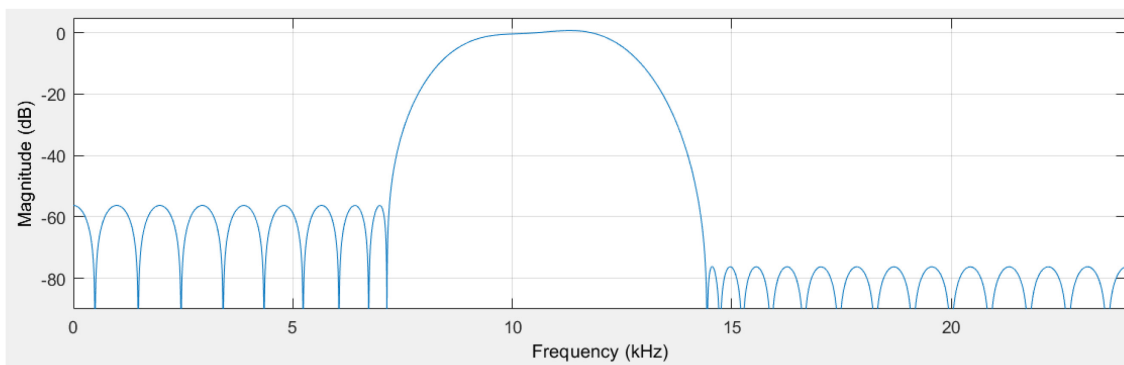


Figure D. 4 Frequency response in dB for a band-pass, equiripple FIR filter

Other methods for the design of FIR filters are summarized by (Shin & Hammond, 2008). The window method designs the filter in a Fourier series form that is then truncated. The truncation introduces distortions in the frequency domain which can be reduced by modifying the Fourier coefficients using windowing techniques. Other method is the frequency sampling method that specifies the filter in terms of $H(k)$, where $H(k)$ is the Direct Fourier Transform (DFT) of $h(n)$. This method is useful for narrow band-pass filters. The last method defined is the principle of optimal filter design. It consists in minimizing the mean square error between the desired filter characteristic and the transfer function of the filter.

D.2 Butterworth Filters

The Butterworth filter is designed as an analogue filter and then used for digital applications. Some basic filter concepts are extracted from (Wanhammar & Saramäki, 2020) for the understanding of these kind of devices.

The synthesis of an analogue filter is the first step in designing a corresponding digital filter. The design process is summarized on *Figure D. 5*.



Figure D. 5 Design of digital filters using analogue prototypes. Adaptation from (Wanhammar & Saramäki, 2020)

The frequency response of the filter is

$$H(i\omega) = |H(i\omega)| e^{i\varphi(\omega)} \quad (D.11)$$

With a linear-phase response equal to

$$\varphi(\omega) = -\omega\tau_1 + \tau_2 \quad (D.12)$$

where τ_1 and τ_2 are constants. Analogous for the velocity of mechanical waves, the phase and group delays are defined as

$$\begin{aligned} \tau_\varphi(\omega) &= -\frac{\varphi(\omega)}{\omega} \\ \tau_g(\omega) &= -\frac{\partial\varphi(\omega)}{\partial\omega} \end{aligned} \quad (D.13)$$

The impulse response is obtained by making the inverse Fourier transform of the frequency response function of *equation (D.11)*

$$h(t) = \frac{1}{2\pi} \int_{-\infty}^{\infty} H(i\omega) e^{i\omega t} d\omega = \frac{1}{2\pi} \int_{-\omega_c}^{\omega_c} e^{-i\omega t} e^{i\omega t} d\omega = \begin{cases} \frac{\omega_c}{\pi} \frac{\sin(\omega_c(t - \tau))}{\omega_c(t - \tau)} \\ \frac{\omega_c}{\pi} \end{cases} \quad (D.14)$$

The aim of the filters is to separate the desired signal from one or more undesirable signals, also called noise. It is not possible to achieve an exactly constant attenuation over a band of frequencies, so it is necessary to establish some limits as previously done for FIR filters. These limits are chosen to tune the variation of the attenuation and the effects of components tolerances and dissipation. It is possible to see the limits of an attenuation specification for a low pass filter on *Figure D. 6*.

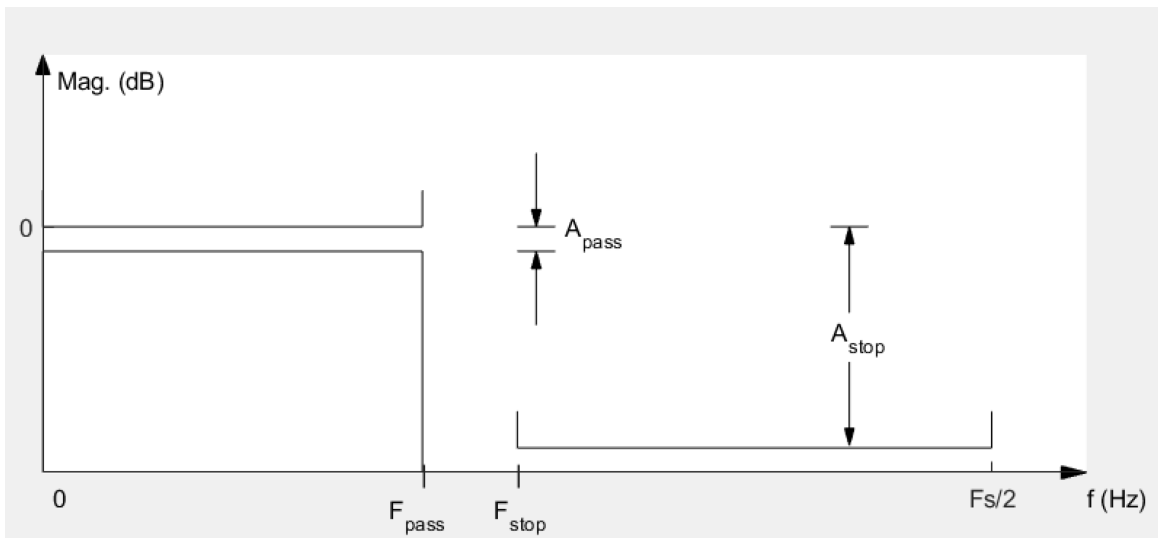


Figure D. 6 Specifications for the attenuation of a Low pass filter

The variation in the attenuation function in the pass band is delimited by A_{pass} while the attenuation in the stopband should not be smaller than A_{stop} .

The *passband* goes from 0 to F_{pass} (or ω_c), it contains the desired signal. The ideal requirements of the filter are to provide constant attenuation and constant group delay so that no distortions are introduced to the signal.

The *transition band* goes from F_{pass} (or ω_c) to F_{stop} (or ω_s). The attenuation function of a filter is continuous, and no discontinuities are allowed thus, an interval region from that unites the edge of the passband with the edge of the stop band needs to be present. As the transition band gets smaller, the order and complexity of the filter rises.

The *stopband* contains the undesired signals, it begins at F_{stop} (or ω_s) and extends theoretically to infinity.

A linear phase response is desirable for some filter applications, this is analogous to have a constant group delay in the passband. With this, the waveform of the input signal is preserved.

The Butterworth filter is an analogue filter approximation. It has a mainly flat magnitude function at the origin and the variation of the group delay is large, inclusively in the passband. This approximation requires larger filter orders to meet given specifications. Nevertheless, they are usually chosen because they are mathematically simple. On *Figure D. 7* Butterworth filter attenuation properties are compared with other kind of filters.

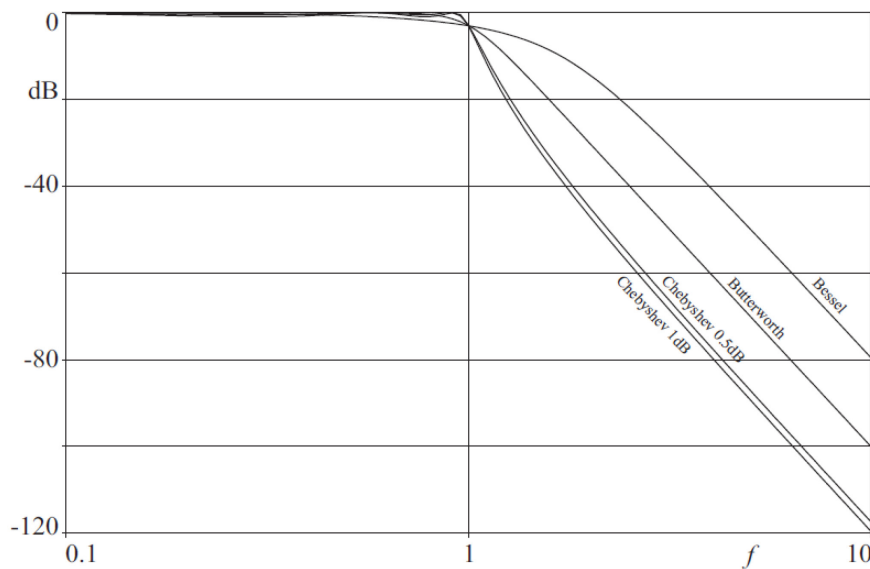


Figure D. 7 Comparison between the characteristics of four different filters of order 5. From (Mwakali & Taban-Wani, 2006).

As the order of the filter rises, the group velocity increases and the peaks become sharper as seen in *Figure D. 8*

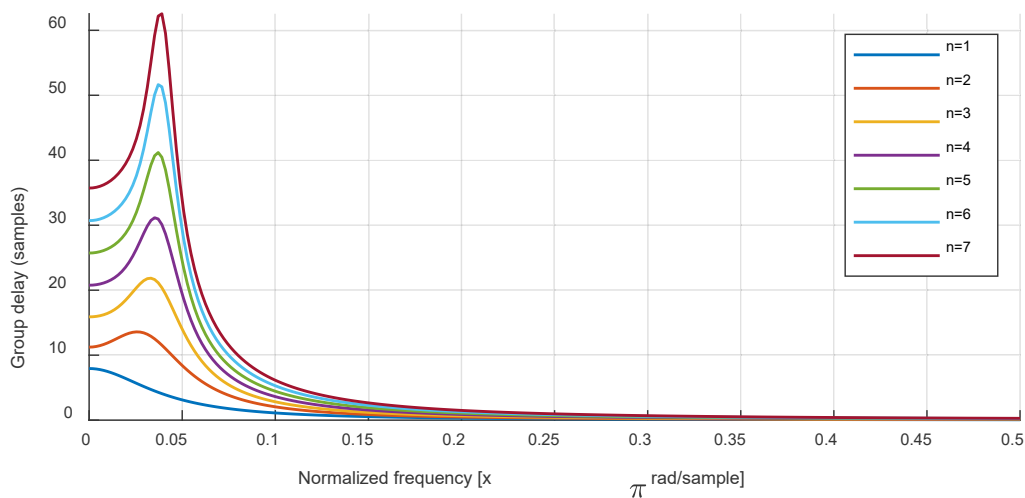


Figure D. 8 Group delay for Butterworth filters of different orders

Finally the frequency response function is calculated for a Butterworth low pass filter of different orders is shown on *Figure D. 9*

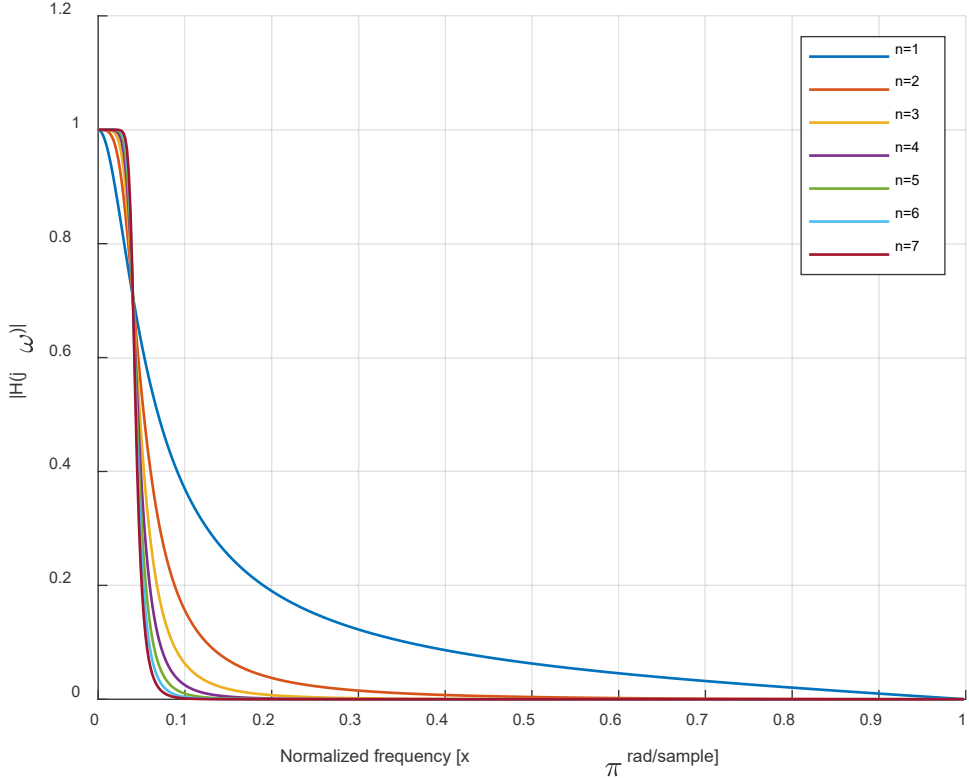


Figure D. 9 Frequency response function of a low-pass Butterworth filter for different orders

References

- (CENELEC), E. C. (2018). *Railway applications - Current collection systems - Validation of simulation of the dynamic interaction between pantograph and overhead contact line - EN 50318*. Brussels: CENELEC.
- Antonucci, E. (1993). *Infrastrutture Ferroviarie*. Pitagora.
- Bosso, N. (2021). *Progettazione di veicoli ferroviari, metropolitani e ad alta velocità*. Turin .
- Bucca, G., & Collina, A. (2007). *A procedure for the wear prediction of collector strip and contact wire in pantograph–catenary system*. Milan: Elsevier.
- Canuto, C. (2021). *Notes of the Lecture Course NUMERICAL MODELS AND METHODS*. Turin: Dipartimento di Scienze Matematiche.
- Chung, J., & Hulbert, G. (1993). *A Time Integration Algorithm for Structural Dynamics With Improved Numerical Dissipation: The Generalized- α Method*. Michigan: Department of Mechanical Engineering and Applied Mechanics - University of Michigan.
- Connolly, D., Kouroussis, G., Woodward, P., Alves Costa, P., Verlinden, O., & Forde, M. (2014). *Field testing and analysis of high speed rail vibrations*. Edinburgh: University of Edinburgh - University of Porto - University of Mons - Institute for Infrastructure & Environment, Edinburgh .
- Dahlberg, T. (2006). *Moving Force on an Axially Loaded Beam With Applications to a Railway Overhead Contact Wire*. Taylor and Francis.
- Fasana, A., & Marchesiello, S. (n.d.). *Meccanica delle Vibrazioni*. CLUT.
- Gear , C. (1971). *Numerical Initial Value Problems in Ordinary Differential Equations*. Englewood Cliffs - New Jersey: Prentice-Hall.
- Genta, G. (2009). *Vibration Dynamics and Control*. Turin: Springer.
- Géradin, M., & Rixen, D. (2015). *Mechanical Vibrations - Theory and Application to Structural Dynamics* (3rd ed.). Wiley.
- Goudreau , G., & Taylor, R. (1973). *Evaluation of numerical methods in elastodynamics*. Livermore: University of California.

- Hilber, H. (1976). *Analysis and design of numerical integration methods in structural dynamics*. Berkeley,: University of California.
- Hilber, H., Hughes, T., & Taylor, R. (1977). *Improved Numerical Dissipation For Time Integration Algorithms In Structural Dynamics*. Berkeley: University of California.
- Hyeon Cho, Y. (2008). *Numerical simulation of the dynamic responses of railway overhead contact lines to a moving pantograph, considering a nonlinear dropper*. Woram-dong: Korea Railroad Research Institute (KRRI).
- Iwnicki, S., Spiryagin, M., Cole, C., & McSweeney, T. (2019). *Handbook of Railway Vehicle Dynamics* (Second ed.). CRC Press.
- Lee, Y.-J. (2016). *Physics III: Vibrations and Waves*,. Massachusetts: Massachusetts Institute of Technology.
- MATLAB. (2021). Retrieved from Mathworks Web site:
https://it.mathworks.com/help/matlab/ref/fft.html?searchHighlight=FFT&s_tid=srchtitle_FFT_1
- MATLAB. (2021). *Mathworks Web site*. Retrieved from
<https://it.mathworks.com/discovery/filter-design.html>
- Meirovitch, L. (2001). *Elements of Vibration Analysis*. (M. G. Hill, Ed.)
- Morse , P. (1948). *Vibration and Sound* (Second ed.). McGraw-Hill Book Company, INC.
- Mwakali, J., & Taban-Wani, G. (2006). *Proceedings from the International Conference on Advances in Engineering and Technology*. Entebbe, Uganda: Elsevier.
- Newmark, N. (1959). *A method of computation for structural dynamics*. American Society of Civil Engineers (ASCE).
- Nickel, R. (1971). *On the stability of approximation operators in problems of structural dynamics*. Whippany - New Jersey: Bell Telephone Laboratories Inc.
- Park, S., Jeon, B., Lee, J., & Cho, Y. (2006). *Measurement of low-frequency wave propagation in a railway contact wire with dispersive characteristics using wavelet transform*. Key Engineering Materials.
- Popov, V. (2010). *Contact Mechanics and Friction - Physical Principles and Applications*. Berlin: Springer.

- Schupp, G., Weidemann, C., & Mauer, L. (2006). *Modelling the Contact between Wheel and Rail within Multibody System Simulation*. Taylor & Francis.
- Shin, K., & Hammond, J. (2008). *Fundamentals of Signal Processing for Sound and Vibration Engineers*. Andong, Republic of South Korea - Southampton United Kingdom: WILEY.
- Signorini, A. (1959). *Questioni di elasticità non linearizzata e semilinearizzata*. Roma: Department of Mathematics of the Sapienza University of Rome - Istituto Nazionale di Alta Matematica Francesco Severi.
- Strauss, A. (2014). *Development of numerical models for the dynamic analysis of pantograph-catenary interaction*. Turin: Politecnico di Torino.
- Turri, R. (2017). *Il sistema catenaria e la qualità della captazione della corrente nella trazione AV/AC*. Padova: Università degli studi di Padova.
- Vo Van, O. (2016). *Pantograph-Catenary, Introduction of variability into dynamic simulations*. Paris: Paris Tech - Paris Institute of Technology.
- Wanhammar, L., & Saramäki, T. (2020). *Digital Filters Using MATLAB*. Linköping, Sweden - Tampere, Finland: Springer.